Tomas Bata University in Zlín
Centre of Polymer Systems

Doctoral Thesis

Reinforcing mechanisms of polymer matrix composites: evaluation and modeling of matrix/dispersed phase interrelationship

Zpevňující mechanismy kompozitů s polymerní matricí: hodnocení a modelování vztahů mezi matricí a disperzní fází

Author: **Julian Niklas Rech**

Degree programme: P0719D130002 Nanotechnology and Advanced Materials

Supervisor: Prof. Ing. Berenika Hausnerová, Ph.D.

Consultant: Prof. Dr.-Ing. Bernhard Möginger

Zlín, August 2025

Keywords: *polymer matrix composite, modeling, elastic behavior, viscoelasticity, interfacial adhesion*

Klíčová slova: *kompozity s polymerní matricí, modelování, elastické vlastnosti, viskoelasticita, mezifázová adheze*

Full text of the doctoral thesis is available in the Library of TBU in Zlín.

Resume

This doctoral thesis presents a comprehensive study on the mechanical behavior of polymer matrix composites (PMC), focusing on process-structure-property relationships and the development of advanced modeling approaches. It introduces the impulse excitation technique as a reliable, non-destructive method for determining elastic properties of PMC and extends the modeling approaches according to Paul and Ishai-Cohen to incorporate interfacial adhesion effects. These modifications enable more accurate predictions of the mechanical performance of the PMC. Additionally, a viscoelastic model based on the concept of elementary volume was developed and validated for both particle- and fiber-filled composites, taking into account filler content, orientation, and time-dependent adhesion in order to improve long-term creep predictions.

Resumé in Czech

Tato dizertační práce představuje komplexní studii mechanického chování kompozitů s polymerní matricí (PMC), se zaměřením na vztahy mezi zpracováním, strukturou a vlastnostmi, a na vývoj pokročilých modelovacích přístupů. Práce zavádí metodu impulzní excitace jako spolehlivý a nedestruktivní nástroj pro stanovení elastických vlastností PMC, a rozšiřuje modely podle Paula a Ishai–Cohena o vliv adheze na rozhraní fází. Tato modifikace umožňuje přesnější predikci mechanického chování těchto kompozitních materiálů. Dále byl vyvinut a experimentálně ověřen viskoelastický model založený na konceptu elementárního objemu, a to jak pro kompozity plněné částicemi, tak vlákny. Model zohledňuje obsah a orientaci plniva i časově závislou adhezi, což zlepšuje predikci dlouhodobého creepu (tečení) materiálu.

Abstract

The use of polymer matrix composites has been tremendously increased during the last 100 years due to easy and low-cost processability, light weight and outstanding mechanical properties. Their ability for easy developing high-performance tailor-made parts necessitates a comprehensive analysis of their process-structure-property relationship. Many models were developed to predict the mechanical properties. However, some issues concerning adhesion effects of matrix and dispersed phase have been hardly investigated and are still unclear. This doctoral thesis summarizes the general knowledge how polymers and dispersed phases interact in such composites and how their mechanical properties are modelled and experimentally determined.

At first, the *cube in cube* approaches originally developed by Paul and Ishai-Cohen were modified by the elementary volume concept to account for interfacial adhesion effects in terms of an adhesion coefficient quantifying an imperfect filler matrix adhesion. This enables a fast calculation of composite moduli based on matrix and filler properties as well as filler content and fits well with experimental data for various polymer composites. The adhesion coefficients were found to be 0.5 to 0.6 for the polar matrices polyamide 66 (PA66) or poly(butylene terephthalate) (PBT) and 0.1 to 0.2 for the nonpolar polyethylene or polypropylene matrices. These values were qualitatively confirmed by scanning electron microscopy (SEM) and specific surface energies. Property predictions worked well for filler volume contents not exceeding 20 %. Furthermore, the elementary volume concept led to a model that predicts the composites creep on base of the matrix creep and filler volume content, and it allowed for to determine a time-dependent adhesion coefficient for glass bead filled PBT. The application of the model to the creep behavior of short glass fiber reinforced PBT composites with 20 and 30 weight-% fiber contents needed to account for fiber misalignment in terms of orientation factors. The creep compliances parallel and perpendicular to the flow direction were underestimated if compared to experimental creep data because fiber matrix adhesion was assumed to be perfect. SEM analysis of fracture surfaces led to the conclusion that fiber matrix adhesion and failure behavior is affected by the stress direction with respect to the fiber axis.

To ensure reliable predictions and simulations, the model requires input parameters derived from experiments. Various methods – tensile tests, dynamic mechanical analysis (bending and torsion), and tensile creep tests – were evaluated with respect to their sensitivity to matrix-filler interactions and filler orientation. Special focus of this thesis was laid on the impulse excitation technique as a fast method to determine the elastic behavior of glass bead filled PA66 and PBT composites under tensile, shear and bending excitations. IET results aligned well with conventional tests, confirming its reliability for characterizing elastic properties of thermoplastic composites as a fast and non-destructive alternative.

Acknowledgements

First of all, I would like to thank my Ph.D. supervisor Berenika Hausnerová for her competent, wonderful, and caring support. Both the academic work and personal exchanges had a strong impact on me and provided tremendous support, making the path to my Ph.D. extremely enriching and—thanks to you—also successful. Thank you very much!

Next, my deepest thanks also go to my supervisor Bernhard Möginger. You were already my supervisor during both my bachelor's and master's theses, and then you made it possible for me to pursue a Ph.D. You have played a significant role in shaping my academic journey. Thank you for being a great teacher, mentor, advisor, and so much more!

To you as well, Johannes Steinhaus, I want to express my deepest thanks and utmost respect. You made it possible for me to continue my future at the university. Both as a colleague and as a friend, you are truly a great asset for me. Thank you!!

Dear Esther, since the beginning of my time at the university, you have been one of my most important points of contact, both professionally and personally, always ready to offer help. On our first trip to Zlín, we quickly realized that working together would never be boring. Thank you for being such a wonderful person.

I would also like to thank Christian Dresbach for the strong support, the valuable exchange, and for always asking you questions I don´t have an answer to. Working with you is simply a pleasure – I´m already looking forward to more of it in the future. (P.S.: Maybe one day I'll finally manage to learn Python).

Thank you as well, Mandy Gieler-Großgarten, for being such a refreshing, witty, and highly competent person. With you as one of the two heads of our working group, the future of AG Polymere can only be bright.

The always-hungry Michi, favorite office companion, and there from the very beginning. As far as I remember, I've followed your career path step by step.....one might say you've been something of a role model for me – just kidding. Thank you for all the moments we've already shared—and the many more to come!

Dear Daniela, I also want to thank you—not counting the cleanup duties—for everything: your warm and caring nature, your dedication, your sense of humor, and the fact that we're just on the same wavelength. (P.S.: Don´t take everything so serious).

Lara aka. Larilarolaralala, thank you for being part of my journey from the very beginning. Even though you took a few short breaks from the university, you always found your way back—and I'm really glad you did. Without you, the working group wouldn't be the same.

Astrid and Klaus, the two of you taught and inspired me already during my bachelor's studies and sparked my interest in materials science. A few years later,

I can proudly call myself your colleague and friend—and for that, I'm more than just grateful!

Abdul and Christian, from master's thesis advisor and practical supervisor to best buddies — I had the honor of being part of your weddings and got to know your wonderful little families. For that, I'm endlessly grateful!

Many, many thanks to all other wonderful colleagues who supported me and were simply there along the way: Hannah Rohde, Cassandra Moers, Marc Williams, Philipp Gillemot, Thomas Haenel, and many more. Special thanks to Bernd Evers-Dietze and Patrick Michels for their active expertise, and of course Michal Studený from the TBU for his valuable support!

I would like to thank Ulrike, Wilma, Rainer, and Marcel for welcoming me so warmly into your family, for always making me feel welcome, and of course for your ongoing support!

A loving thank you to Alisa for your emotional support, for always being there for me, and for being a part of my life — in fact, the very center of it. The future is going to be amazing.

During my Ph.D., I mainly worked with elastic constants of materials — but the only constant that truly mattered was always my family –Ute, Rainer, Florian – I love you and thank you for everything!

Contents

1 State of the Art

1.1 Introduction to composites science

Composites systems were studied by important scientists such as Poisson, Faraday, Einstein and others. They contributed significantly to the understanding of composites performance and the current state of knowledge on a physical and mathematical point of view [1]. Composites are defined as a macroscopic homogeneous material consisting of two or more microscopic phases retaining their chemical and physical identities. Between these phases a distinct interface may contribute to synergetic effects of the material [2]. On this base, composites are classified with respect to the matrix as metal matrix composites (MMC), ceramic matrix composites (CMC), or polymer matrix composites (PMC), Fig. 1.

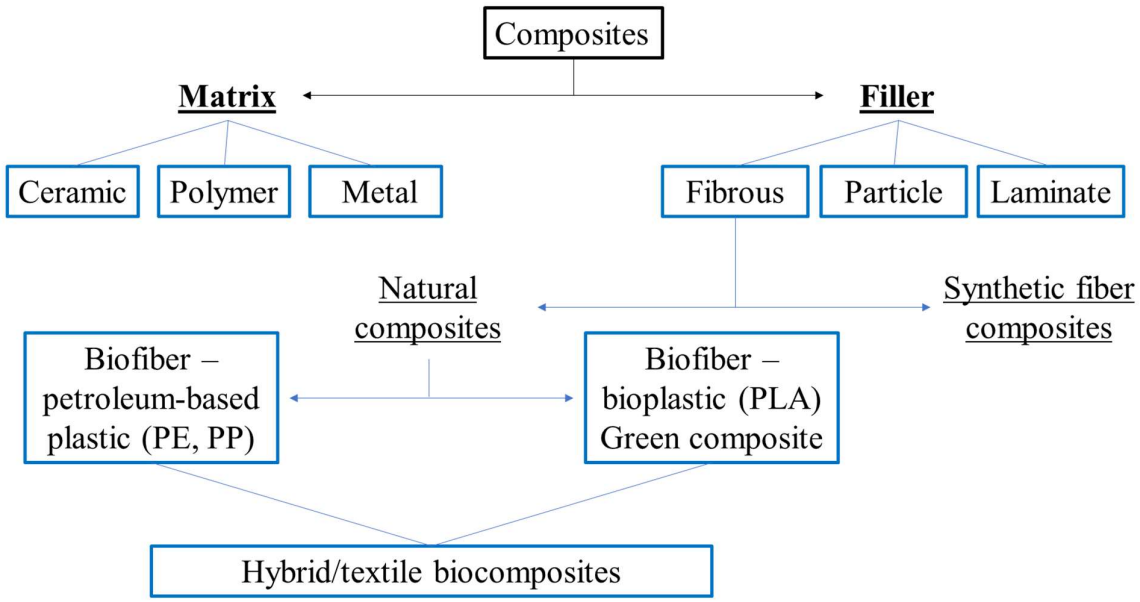

Fig. 1 Classification of composites with respect to matrix and dispersed phase, adapted from [3].

This classification shows that these materials are ubiquitous in both natural or industrial engineered materials. To describe the properties of a composite in detail both the matrix, or continuous phase, and the dispersed phase in terms of fibers, fillers or toughеners have to be taken into account. Furthermore, due to their interactions, synergetic effects may provide additional benefits on the macroscopic scale not shown by the constituents.

In the last decades PMC gained an important role due to their straightforward and economical processability and their high potential in light weight design, e.g. in building industry, automotive, aerospace, sports and household as well as electrical industry [4]. However, sustainability demands of polymer parts are steadily increasing as well. Currently, not only polymeric systems from renewable

sources are developed, but also established materials and commodities have to be brought in the recycling process to meet legislation towards a closed-loop economy. To meet application requirements, these "recycled" materials have often to be "improved" by introducing dispersed phases. Matrix and dispersed phase address different tasks in composites behavior, Table 1.

Table 1 Task address of matrix and dispersed phase in a composite [5].

matrix phase	dispersed phase
• affirms adhesion to composites • transfer of external stresses to dispersed phase • determines the final shape of the part • protects fibers and filler particles	• increase in toughness ($E_F < E_M$) • increase of stiffness and strength ($E_F > E_M$) • increase in special properties e.g. heat or electrical conductivity, abrasion resistance, flammability or color • reduction of costs

To meet application requirements, a controlled and uniform distribution of the dispersed phase has to be achieved by compounding regardless of its shape [5]. Furthermore, the composites properties, e.g. thermal, mechanical, and/or electrical properties have to be determined with respect to the given application. This can be either accomplished by an elaborate analysis of the mentioned properties, which is expensive and time-consuming, or reliable and accurate predictions using theoretical approaches and models.

History of composites

The development of composites can be dated back to around 3400 BC. Mesopotamians created a ship made of plywood by glueing layers of wooden pieces at different angles, thus, enhancing durability and performance of the ships. 2000 years later, straw and wood reinforced mud bricks were found in Egypt and Mesopotamia as construction materials in buildings, boats or pottery [6]. Fig. 2 shows the evolution of the dominant material classes: metals, polymers, composites, ceramics and glasses [7].

In the 12th century Mongolian warriors invented the first weapon using bamboo, silk, tendon from cattle, bones and horns embedded in pine resin creating superior arches and arrows. The synergetic effects of these materials yielded an early-age composite bow enhancing the shooting range compared to pure wooden bows [8].

Although all aforementioned inventions demonstrated the capability of composites, it lasted another 700 years to significantly increase the demand of composites. The breakthrough started with the upcoming chemical revolution and the invention of synthetic polymeric resins. In 1907, Belgian-born US chemist Leo Hendrik Baekeland invented the first synthetic resin called Bakelite, a thermosetting phenol formaldehyde resin formed by polycondensation resulting in a cross-linked molecular structure. Because of its brittleness Baekeland

combined the resin with cellulose to soften the material and manufactured the first commercial product, a gearshift knob, in 1917 for Rolls Royce® automobiles. Bakelite possessed a wide application range due to its electric impermeability and heat resistance and was designated as the first synthetic plastics in the world [9]. The invention of the polymerization process represented the beginning of PMC. In 1937 to 1941, Carleton Ellis [10] patented his invention of unsaturated polyester resins. The curing reaction of glycols with maleic anhydride led to an insoluble solid if a peroxide catalyst was added. Further investigations led to high performance resins, such as epoxy or other phenolic resins [11]. This development opened the "playground" of reinforcing, toughening, electric conducting, flame-retardening, and many other applications of composites being scientific topics up to now.

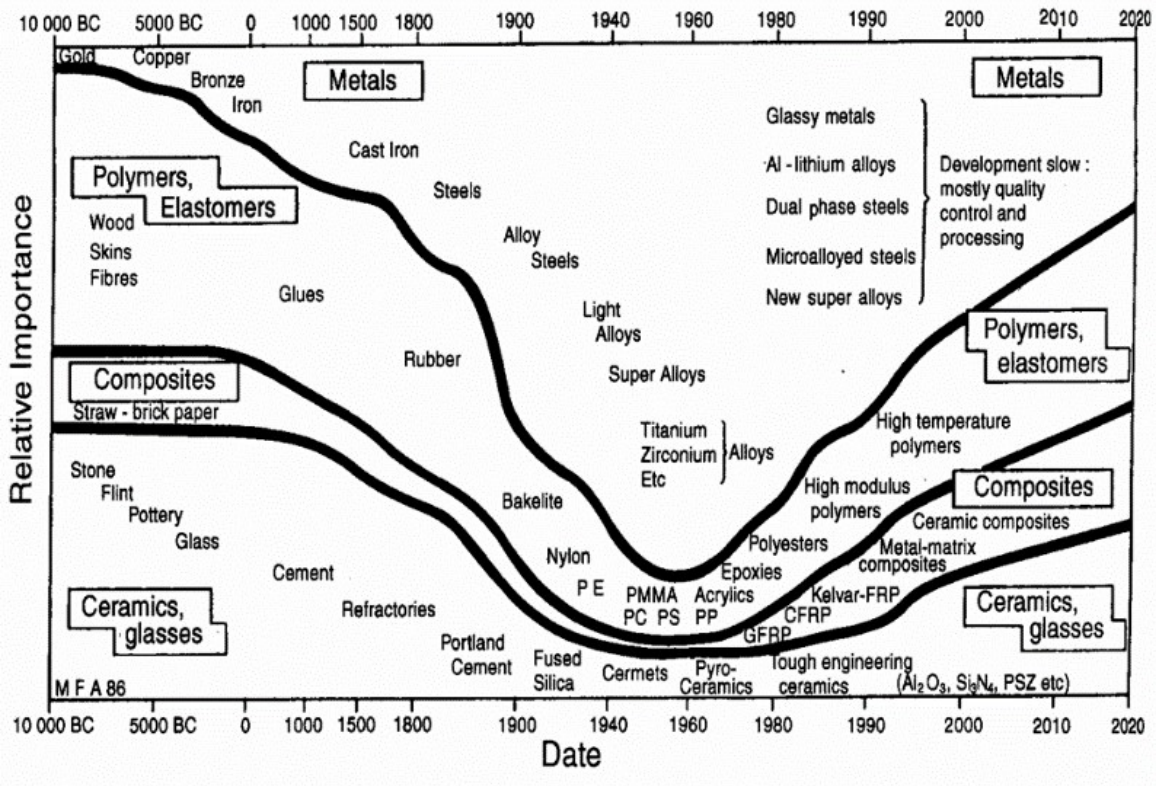

Fig. 2 Schematic overview of historical achievements of the material classes metals, polymers, composites and ceramics and glasses and their relative importance over time [7].

1.2 Polymer matrix composites

Polymers consist of highly polymerized monomer units forming huge macromolecules. These macromolecules can be either linear or branched in shape forming amorphous/semi-crystalline thermoplastics, or cross-linked network structures – elastomers and thermosets, Fig. 3.

matrix polymers			
linear and branched polymers		cross-linked polymer networks	
amorphous	semi-crystalline	widely meshed	closely meshed
	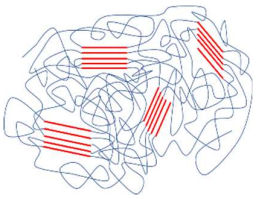	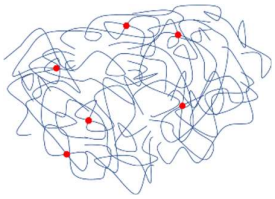	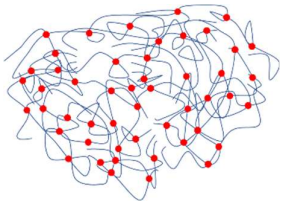
thermoplastics		elastomers	thermosets

Fig. 3 Polymer classes and their schematic morphology of macromolecular arrangement.

1.2.1 Polymer matrices and their properties

Thermosets

Thermosets are polymeric materials that are synthesized and highly cross-linked in one step to a "single" molecule due to multifunctional reactive groups of monomers or pre-polymers units with low molecular masses. This leads to an amorphous network structure being insoluble with excellent thermal and dimensional stability of rigid parts. Thermosets can be synthesized by radical and ionic polymerization, addition polymerization or condensation polymerization [12]. The most common resin systems and their property profile are shown in Table 2.

Table 2 Property overview of thermosets [13-19].

		resin systems						
		phenolic	amino	polyester	epoxy	silicone	polyimide	acrylate
		C*	C*	A/C*	A*	C*	C*	R*
properties	mechanical	↑	/	/	↑↑↑	↑↑↑	↑↑	/
	thermal	↑	↑	↑↑↑	↑↑↑	↑↑↑	↑↑↑	↑↑
	dielectrical	↑	↑	↑↑↑	↑↑↑	↑↑↑	↑↑↑	/
	chemical	/	/	/	↑↑↑	/	↑↑	↑↑
	colorability	↓	↑↑↑	↑↑↑	↑↑	/	↓↓	→[1]
	adhesion	/	/	/	↑↑	/	/	↑↑
	flame retardancy	↑	↑[2]	/	↑↑	/	↑↑↑	/
	price	↑↑↑	↑↑	↑↑	↓	↓↓	↓↓	↑↑

[1]transparent; [2]only for urea-based resins

* polycondensation (C), polyaddition (A), radical polymerization (R)

property profile ranging from very good (↑↑↑) – moderate (→) – suboptimal (↓↓)

Thermoset matrices are synthesized under heat/pressure/radical initiation forming a high cross-linked density network structure, depending on the functionality of the reactants in the polymerization process. Thermosets do not soften, only decompose on heating, and cannot be reshaped after the manufacturing process. Due to this thermal behavior, thermosets have to be manufactured in the so-called reaction injection molding (RIM or RRIM for reinforced RIM). Here, the monomers or oligomers are fed separately into the injection unit, are injected and reacting in the mold to the final product [11].

Elastomers

Elastomers are made by almost amorphous thermoplastics having low glass temperatures ($T_G < T_{ambient}$) that are subjected to a second processing step in which cross-linking agents create a loosely cross-linked morphology. This morphology is responsible for the rubber elasticity- with a non-hookeian deformation behavior and extraordinary reversible elongations. To create new properties the backbones were modified by copolymerization and blending to meet the application requirements [20]. All elastomers unite a random-coil structure yielding in an entropy elastic behavior with characteristic low modulus but high damping. Furthermore, elastomers cannot crystallize considering the hindered chain mobility and irregularity caused by the wide-meshed crosslinks. This in turn ensures that they exhibit a glass transition temperature far below room temperature and cannot be melted but only decompose at high temperatures. One exception is the class of thermoplastic elastomers (TPE) which can be formed through block-copolymerization of semi-crystalline hard segments and amorphous soft segments. The hard segments with a high melting temperature, e.g. polyamides or polyester, form crystalline domains serving as virtual crosslinks, whilst the amorphous soft segments, e.g. polyethers, polyesters, with a low glass transition temperature contribute with their elasticity.

Most elastomers have to be filled with particles to achieve relevant property spectra. Two specific examples are natural rubber/carbon black and polysiloxane rubber/silica. Both elastomers cannot undergo strain-induced crystallization and are therefore compounded with a reinforcing filler increasing the abrasion resistance, tear strength, and tensile strength but disadvantaging the hysteresis and compression set yielding in heat buildup and permanent deformation, respectively [20].

Thermoplastics

Thermoplastic matrices have amorphous or semi-crystalline morphologies and consist of linear or branched chain molecules connected by intermolecular forces (dipole-dipole-interaction, hydrogen-bonding and/or van der Waals-forces). They are fully polymerized, can be solved, and able to be altered thermo-physically by softening or melting due to their lack of intermolecular networking. However, this ability especially opens the field of recycling and reshaping and thus, the reuse of thermoplastic matrix materials [21]. Fig. 4 depicts the classification of

thermoplastics which is based mainly on their individual mechanical, thermal, and physical properties.

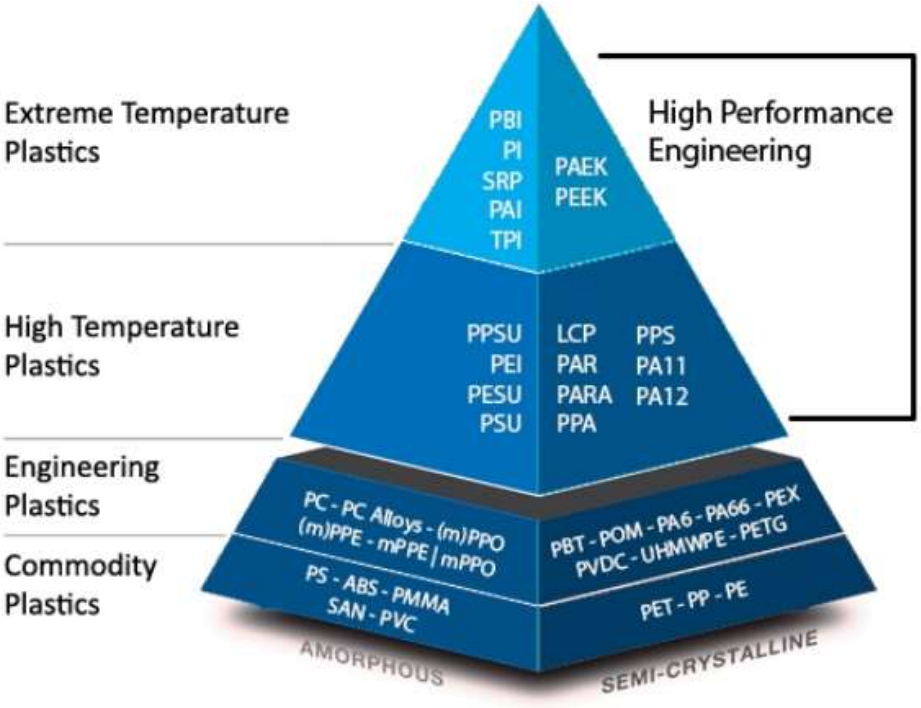

Fig. 4 Amorphous and semi-crystalline classification of thermoplastic polymer classes [22].

An important point in composite production is the compatibility in terms of polarity between filler and matrix. Amorphous and semi-crystalline thermoplastics exhibit either a polar or non-polar behavior depending on heteroatoms such as nitrogen, oxygen, fluorine, chloride, etc. in the monomer unit. Different electro-negativities of the atoms in the monomer unit result in a permanent dipole shift yielding in a more or less polar polymer. Matching polarities between matrix and filler material have to be taken into account when synergism effects for a e.g. better mechanical performance should be achieved. However, a mismatch of polarities can be overcome by filler surface treatments either chemically via plasma modifications, or coupling agents enhancing the filler-matrix adhesion [23].

In a polymer melt, the molecules are arranged as entangled random coils. During cooling the polymer solidifies either as an amorphous glassy solid consisting of entangled molecules without any long-distance order or in a structure of amorphous and highly ordered crystalline lamellae. Prior elongational and shear flows in the melt orient the macromolecules and may cause anisotropic material properties of the solid polymer and lead to a skin core structure.

The result for amorphous thermoplastics is a skin region of macromolecules oriented in flow direction, whereas in the core regions the macromolecules remain in their entropically favorable random coil state resulting in internal stresses

which can be made visible by polarized light microscopy. For semi-crystalline polymers, this yields cross-sectional varying crystal sizes.

As the crystallization process in polymers depends on time the cooling rate during solidification determines the cross-sectional crystallinity distribution. High cooling rates generate many nuclei forming a fine spherulitic structure in the skin region, low cooling rates in the core region generate less nuclei that can grow to large spherulites. Spherulites are formed of radially oriented crystal lamellae in 3D starting to crystallize from a nucleus consisting of lamellae of parallel arranged macromolecules, Fig. 5.

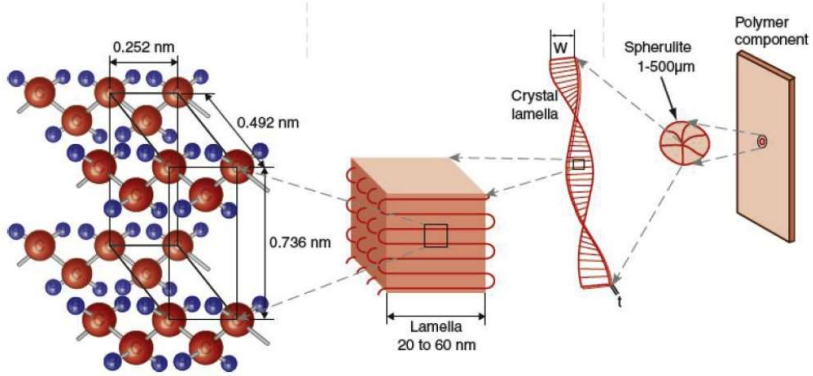

Fig. 5 Molecular structure and principle of spherulite formation using the example of high-density polyethylene (HDPE) [24].

During processing polymer melts experience both elongational and shear flows. They also affect the spatial orientation of platelet-like shaped filler particles or fibers and may cause cross-sectional skin core structures because of the shear flows close to the mold surface orients them in flow direction and elongational flows in the core orients them perpendicular to the flow direction. This leads to an anisotropic materials behavior in terms of mechanical and thermal properties, Fig. 6.

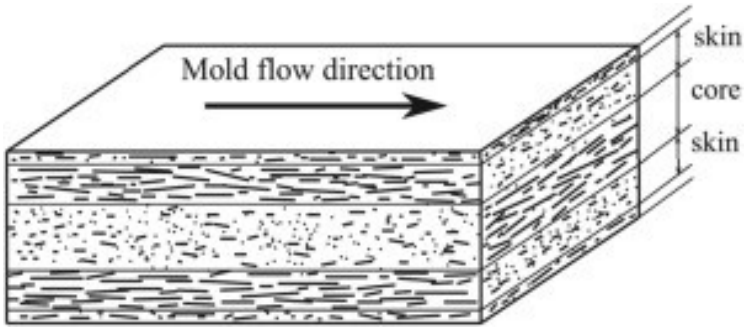

Fig. 6 Shear flow induced skin core arrangement of fiber reinforced composites during injection molding [25].

1.2.2 Dispersed phases and their properties

Dispersed phases can be divided in two classes considering its effects on the polymer matrix: stiffening and/or reinforcing fillers (with filler modulus

E_F > matrix modulus E_M) and toughening particles ($E_F < E_M$). The incorporation of fillers was historically purposed to reduce the cost due to relatively expensive polymers. Nowadays polymers and their composites are indispensable and found in high performance aerospace, maritime, or automotive applications optimizing thermal, mechanical, electrical or chemical properties. That is only possible for synergycally enhanced composites. The filler type can be classified with respect to their physical appearance such as aspect ratio r (length/width ratio) – fiber, spheres, or platelets, Table 3. Many properties can be derived from the aspect ratio but depend also strongly on particle size, filler volume content v_F, and filler matrix adhesion k_{adh}. Additionally, materials behavior is influenced by the resulting anisotropy caused by aforementioned flow conditions during processing.

Table 3 Property overview influenced by various filler types [26].

	fibrous filler					spherical filler							platelets		
property	glass fibers	asbestos	wollastonite	carbon fibers	whiskers	sand/quartz	silica	kaolin	glass beads	$CaCO_3$	metal oxides	carbon black	glimmer	talcum	graphite
Young´s modulus	↑	↑	↑	↑	↗	↗	↗		↗	↗	↗	↗	↑	↗	
tensile strength	↑	↗		↗	→				↗				↗	→	
strain	↓	↓	↓	↓		↓			↓	↓		↓	↓	↓	↓
compressive strength	↗					↗			↗	↗				↗	
impact resistance	*			*		↓	↓	↓	↓	→	↓	↗	→	↓	
red. shrinkage	↗	↗	↗	↗		↗	↗	↗	↗	↗	↗	↗	↗	↗	↗
red. warpage	↓	↓	↓	↓		↗	↗	↗	↑	↑	↗	↗			
red. therm. expansion	↗	↗			↗	↗	↗	↗			↗		↗	↗	
therm. conductivity		↗	↗	↗		↗	↗			↗		↗		↗	↗
heat deflection temperature	↑	↗	↗	↑				↗		↗	↗		↗	↗	
heat resistance			↗			↗	↗	↗			↗	↗	↗	↗	
electric conductivity				↗								↗			↗
electric resistance			↗					↑			↗		↑	↗	
abrasion resistance				↗				↗					↗	↗	↗
cost reduction	↗	↗	↗			↑	↗	↗	↗	↑			↗	↗	↗

*depends on fiber length
property profile affected by dispersed phase: high(↑)–moderate(→)–negative(↓)

1.3 General adhesion mechanisms on composites properties

The performance of PMC is mainly predetermined by the properties of the dispersed phase (filler or toughener) and the polymer matrix. Furthermore, the filler volume content v_F as well as the interfacial adhesion between dispersed phase and matrix (interface) describe how pronounced the individual characteristics are. Although the interface is a thin boundary layer between filler surface and matrix it is of great significance that this small region acts as a transfer for both strength and toughness to achieve good mechanical behavior [27]. The interface and its adhesion mechanisms can be characterized considering physical, chemical, mechanical, and morphological aspects, Fig. 7.

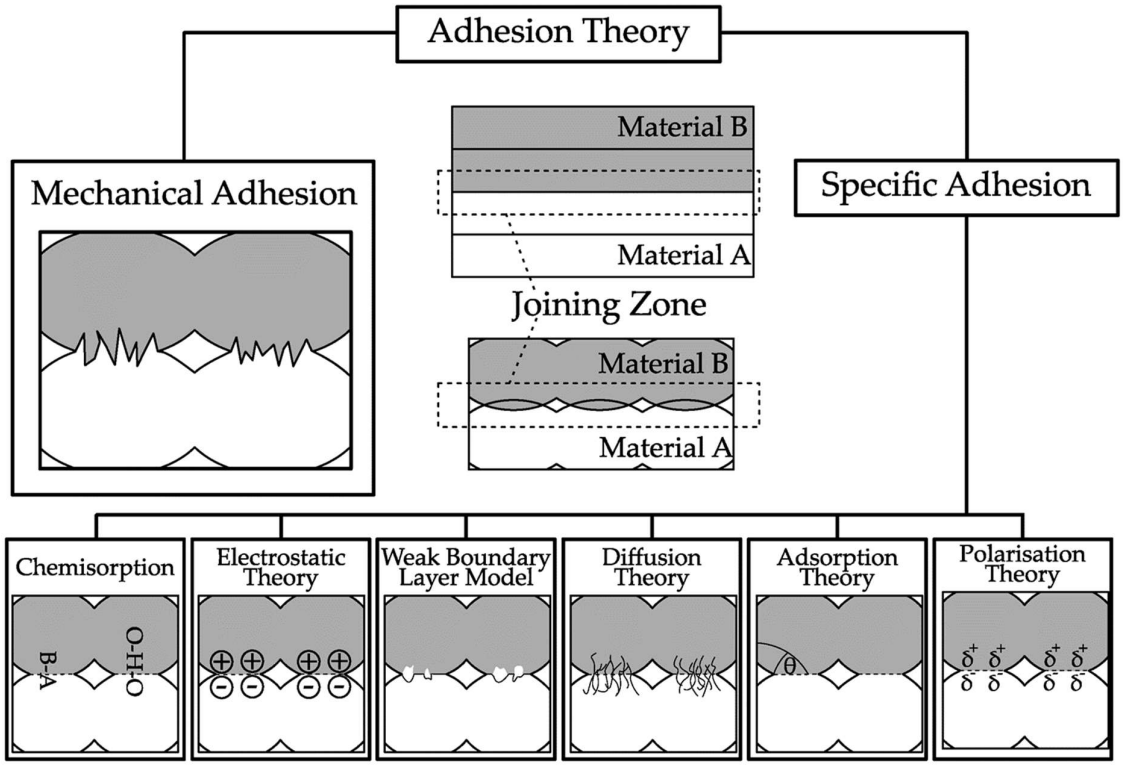

Fig. 7 Possible adhesion mechanisms [28].

The adhesion between two phases arises from several mechanisms:

Mechanical adhesion

requires a rough or porous surface of the filler particles which can be accessed by the molten matrix. Subsequent solidification provides interlocking due to the mechanical overlapping of both materials [29].

Polarization and chemisorption

Van der Waals forces and polar interactions may improve the adsorption due to the polarization of surfaces. In the case of chemisorption additional covalent bonds are formed between both phases [30].

Electrostatic

leads to the formation of electrically charged double layers at the interface evoking attractive forces, thus enhancing the adhesion due to the electrochemical potential difference between the two surfaces [31].

Weak boundary layer

addresses the fact that the interface is weakened due to imperfections or impurities. This reduces the contact areas and thus, the magnitudes of all adhesion mechanisms effects [32].

Diffusion

Brownian motion of molecules and polymer chains leads to an interdiffusion dependent on their affinity and mobility forming an interface which thickness is time and temperature dependent [33].

Adsorption

depends strongly on the wettability of the matrix on filler particles providing also adhesion. The better the wetting, the larger intermolecular forces. A measure of the adhesion behavior is the difference of the surface tensions of matrix and filler particles which can be modified within a certain range by functionalization of the filler particles [34].

1.3.1 Toughening mechanisms

Toughening can be achieved by mechanisms such as particle bridging, matrix cracking, crack front pinning or crack path deflection. To toughen brittle polymers, the dispersed phase often consists of soft rubber particles. Thus, only mechanisms of particulate toughened matrices are considered.

Particle bridging

This mechanism occurs if particles are perfectly bonded to the matrix and the force during loading is solely transferred to the crack tip of the particle so that crack bridges remain. They still connect the two fracture surfaces and are capable to transfer load until they fail. The energy dissipation is then attributed to the plastic deformation of the particle ending in the tearing of particles in the crack path [35], Fig. 8.

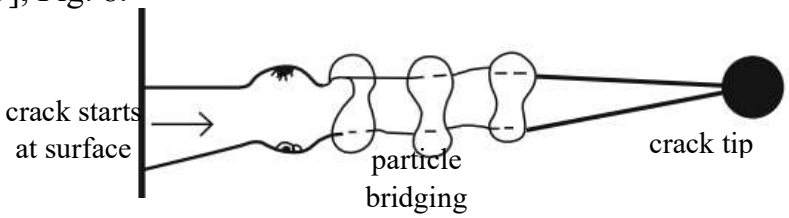

Fig. 8 Particle bridging behind the crack tip [36].

The fracture toughness ratio of the composite is given by [37]

$$\frac{K_c}{K_0} = \phi(1 - v_F) + \frac{f E^* \Gamma_t}{2\phi(1 - v_F)K_0^2} \quad (1)$$

with fracture toughness K_c and K_0 of composite and matrix, respectively, ϕ as a correction factor regarding crack bowing, filler volume content v_F, particle stiffness E^*, and tearing energy Γ_t of the particle.

Matrix cracking

The formation of micro-cracks is enforced by high stresses in the vicinity of the macroscopic crack tip what reduces the residual stress of the tip. Matrix cracking in terms of microcrack toughening can be described by a reduced elastic modulus of the material subjected to microcracking increasing the local dilatation of the matrix [38, 39], Fig. 9.

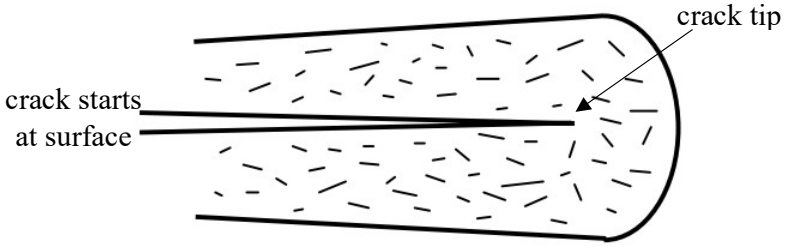

Fig. 9 Schematic of the micro-crack formation in the vicinity of the crack tip [40].

Hutchinson [41] described the elastic contribution as

$$\frac{K_c}{dK_c} = \frac{1-\mu}{\left(k_1 - \frac{5}{8}\right)\left(\frac{G}{G^*} - 1\right)\left(k_2 + \frac{3}{4}\right)\left(\frac{\mu^* G}{G^*} - \mu\right)} \tag{2}$$

with toughness K_c in the absence of microcracks, k_1 and k_2 as constants depending on the shape of microcracking zone, shear moduli G and G^* before and after microcracking, respectively, and Poison´s ratio μ and μ^* before and after microcracking, respectively. The dilatational contribution was derived by [39]:

$$dK_c = k_3 \, E \, \theta_T \, h^{1/2} \tag{3}$$

with k_3 as a constant, additionally depending on the size of the microcracking zone, Young´s modulus E of the neat, uncracked material, dilatational strain θ_T caused by microcracking, and width h of the process zone.

Crack front pinning

The crack-pinning mechanism is associated with rigid thermoplastic particles embedded in a matrix acting as impenetrable objects that cause the propagating crack front to slow and bend down, resulting in a higher energy consumption, Fig. 10. This phenomenon was firstly described and observed by Lange [42] who found “tails” near particles in the fracture surface on scanning electron microscope (SEM) pictures [43], Fig. 10.

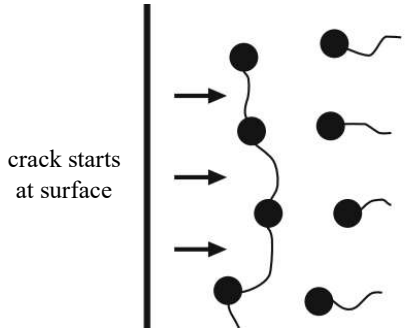

Fig. 10 Schematic of crack-pinning mechanism of rigid inclusion [36].

The toughening effect is given by [42]

$$\frac{K_c}{K_0} = 1 + \frac{Q}{\frac{2d_p(1-v_F)}{3v_F}K_0} \tag{4}$$

with fracture toughness K_c and K_0 of the composite and matrix, respectively, line energy per unit crack front Q, particle diameter d_p and filler volume content v_F.

Crack path deflection

The deflection of the crack out of plane increases the energy absorption and reduces the stress intensity factor at the crack tip. This can occur for two conditions: 1) residual strains in the composite due to weak interfacial adhesion, or 2) residual strains due to mismatching moduli and/or coefficients of thermal expansion of matrix and dispersed phase [39]. Both can lead to an insufficient load transfer to the dispersed phase, deflecting and prolonging the crack path, thus, resulting in a more pronounced toughening behavior, Fig. 11.

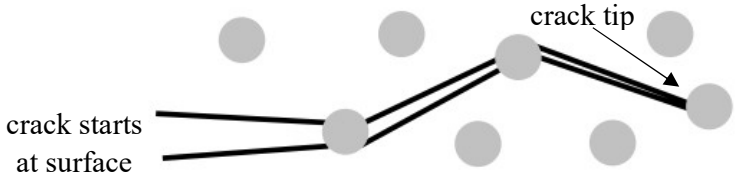

Fig. 11 Schematic illustration of crack path deflection as a toughening mechanism [40].

Faber and Evans [44] investigated this toughening effect for various inclusion and found

$$\frac{K_c}{K_0} = \left(\frac{E_c}{E_0}(1 + 0.87v_F)\right)^{1/2} \tag{5}$$

with fracture toughness K_c and K_0 of composite and matrix, respectively, Young´s modulus E_c and E_0 of composite and matrix, respectively, and filler volume content v_F.

1.3.2 Reinforcing mechanisms

Considering the aforementioned adhesion mechanisms, the reinforcing behavior of filler particles or fibers in composites can be modified by various surface modifications, e.g. covalent coupling of glass fibers (GF) using coupling agents, oxidative plasma etching of carbon fibers (CF), or plasma polymerization and polymer coatings on the filler or fiber surface [45]. All treatments enhance the load transfer between dispersed phase and matrix in the vicinity of either a fiber fracture or a matrix crack.

The shear lag model [46] is widely used to describe the micromechanics of a fiber of length l embedded in a cylindrical matrix which is subjected to a matrix strain ε_M. Assuming purely elastic behavior for both matrix and fiber having perfect adhesion allows the interpretation of the differential displacement in fiber direction. In turn, this displacement is directly proportional to the shear stress at the interface, where the fiber axial stress σ_F and shear stress τ_i along the fiber (z-) direction are given by:

$$\sigma_F(z) = E_F\,\varepsilon_M\left(1 - \frac{\cosh\left(\frac{\beta z}{R'}\right)}{\cosh\left(\frac{\beta l}{2R'}\right)}\right) \tag{6}$$

$$\tau_i(z) = \frac{\beta}{2}\,E_F\,\varepsilon_M\,\frac{\sinh\left(\frac{\beta z}{rR'}\right)}{\cosh\left(\frac{\beta l}{2R'}\right)} \tag{7}$$

$$\text{with } \beta = \left(\frac{2G_M}{E_F \ln\left(\frac{R'}{R''}\right)}\right)^{\frac{1}{2}} \tag{8}$$

with Young´s modulus of fiber E_F, matrix shear modulus G_M, R' and R'' as radii of fiber and matrix, respectively, fiber length l, and the location along the fiber z. The tensile stress is zero at the ends and exhibits a maximum plateau in the middle part of the fiber whereas the shear stress becomes maximum at the left fiber end, zero in the center and a minimum at the right end. Thus, the average stress carried by a fiber of finite length is always lower than for a continuous fiber subjected to the same external load.

For particulate filled composites the shear lag model cannot be applied due to the small aspect ratio of the fillers. These include spherical particles, platelets or needles. Here, the reinforcing mechanisms are synergy effects of different theories including interfacial adhesion theories, filler induced crystallization, and filler frame induced rigidity.

Based on previously described adhesion theories, Turcsanyi et al. [47] proposed an empirical equation to calculate composites yield strength $\sigma_{y,C}$ considering the filler and adhesion effects, Eq. (9),

$$\sigma_{y,C} = \sigma_{y,M} \frac{1 - v_F}{1 + 2.5 v_F} \exp(B v_F) \quad (9)$$

with yield strength of matrix $\sigma_{y,M}$, filler volume content v_F, and B as a measure of the interfacial adhesion strength. The interfacial adhesion strength is weak for $B < 1$, moderate for $1 < B < 3$, and strong for $B > 3$.

Other reinforcing concepts take into account the increased crystallinity due to higher nucleation rates induced by the filler particles or the decreased chain mobility of macromolecules due to stiffer filler frames contributing as a cytoskeleton. Both concepts yield in a reinforcing behavior and an increased rigidity of the composite [48].

1.4 Stiffness models of particle and fiber filled systems

The random distribution of the constituent phases demands a statistical approach, therefore a detailed knowledge of the phase distribution is required. This knowledge depends on a large number of different analyses. For modeling purposes, two-phase approaches were used differing in spatial orientation of the dispersed phase and geometrical segmentations of elementary cells which are subjected to external stresses or strains. This approach implies uniform stresses and strains in each of the phases allowing for the estimation of elastic constants [49, 50]. Numerous models have been developed to calculate the elastic modulus of particulate and fiber reinforced composites considering the elastic properties of its components (matrix and dispersed phase), aspect ratio r, filler volume content v_F, spatial fiber or particle orientation, and fiber/filler particle adhesion, Table 4.

Voigt [51] and Reuss [52] calculated moduli of continuously fiber reinforced composites and identified the mixture rule as the maximum modulus and the inverse mixture rule as the minimum modulus. This indicates that composites consisting of fibers of finite lengths or particles require a more complex consideration. Guth [53] expanded Einstein´s equation [54] of a suspension with spherical inclusions. He concluded that the change in the elastic constants of a suspension filled with rigid spherical inclusions is entirely analogous to the theory of viscosity.

To calculate the modulus of particle reinforced composites, a *cube in cube* approach is used assuming a cube shaped filler particle in a matrix cube. The modulus is determined by an appropriate segmentation in matrix and composites parts. Paul [55] considered an *in series* arrangement of matrix part and composites part, thus, providing the upper bound whereas Ishai and Cohen [56] considered a *parallel* arrangement providing the lower bound, Fig. 12.

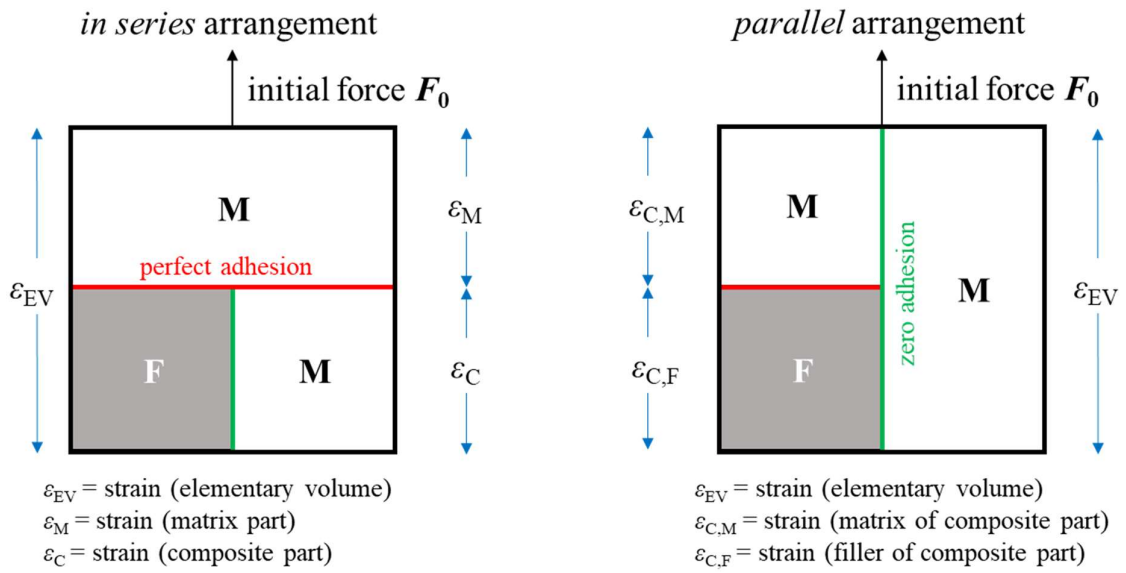

Fig. 12 Representation of Paul´s in series arrangement and Ishai & Cohen´s parallel arrangement.

Hirsch [57] and Takayanagi [58] considered combinations of the Voigt and Reuss models. Hirsch introduced a factor χ balancing their contributions. Takayanagi combined them in a way that allows for introducing a dependency on filler volume content. Counto´s approach [59] was introduced for concrete systems assuming perfect filler-matrix adhesion; coinciding with the Hirsch model for $\chi = 0.5$.

Halpin and Tsai [60] developed an interpolation procedure for composites containing ellipsoidal inclusions by reducing Hermans´ solution [61] of the generalized Hill´s self-consistent model [62]. The shape of the inclusion and its spatial orientation are taken into account by a factor ξ. Due to its simplicity it became popular regardless of limited accuracy.

Lewis and Nielsen [63-65] proposed an alternative model based on Halpin-Tsai [60] and Kerner [66] in which the maximum filler content $v_{F,max}$ and a Poisson ratio-dependent Einstein coefficient K_E occur as additional quantities, Table 4.

Table 4 Overview of two-phase models to predict Young´s moduli of particulate composites.

models	**Young‘s modulus of particle filled composite**
Voigt (1889)	$E_C = E_M\left((1-v_F)+\frac{E_F}{E_M}v_F\right) = E_M(1-v_F)+E_F v_F$ (10)
Reuss (1929)	$E_C = E_M\frac{\frac{E_F}{E_M}}{v_F+\frac{E_F}{E_M}(1-v_F)} = \frac{E_F E_M}{E_F(1-v_F)+E_M v_F}$ (11)
Guth (1945)	$E_C = E_M(1+K_E v_F+14.1v_F^2)$ (12)

Paul (1960)	$E_C = E_M \left(\frac{1+\left(\frac{E_F}{E_M}-1\right)v_F^{\frac{2}{3}}}{1+\left(\frac{E_F}{E_M}-1\right)\left(v_F^{\frac{2}{3}}-v_F\right)} \right)$	(13)
Hirsch (1962)	$E_C = E_M \left(\chi \left((1-v_F) + \frac{E_F}{E_M} v_F \right) + \right) + \frac{(1-\chi)\ \frac{E_F}{E_M}}{v_F + \frac{E_F}{E_M}(1-v_F)}$	(14)
Counto (1964)	$E_C = E_M \left(\frac{\left(1-v_F^{\frac{1}{2}}\right)+v_F^{\frac{1}{2}}\frac{E_F}{E_M}}{\left(1-v_F^{\frac{1}{2}}\right)^2+\left(1-v_F^{\frac{1}{2}}\right)v_F^{\frac{1}{2}}\frac{E_F}{E_M}+v_F^{\frac{1}{2}}} \right)$	(15)
Takayanagi et al. (1964)	$E_C = E_M \Big/ \left(\frac{\frac{5v_F}{(2+3v_F)}}{\left(1-\frac{(2+3v_F)}{5}\right)+\frac{(2+3v_F)}{5}\frac{E_F}{E_M}} + \frac{1-\frac{5v_F}{(2+3v_F)}}{\frac{E_F}{E_M}} \right)$	(16)
Ishai-Cohen (1967)	$E_C = E_M \left(\frac{\frac{E_F}{E_M}+\left(\frac{E_F}{E_M}-1\right)\left(v_F-v_F^{\frac{1}{3}}\right)}{\frac{E_F}{E_M}-\left(\frac{E_F}{E_M}-1\right)v_F^{\frac{1}{3}}} \right)$	(17)
Halpin-Tsai (1969)	$E_C = E_M \left(\frac{1+\frac{\left(\frac{E_F}{E_M}-1\right)}{\left(\frac{E_F}{E_M}+\xi\right)}\xi v_F}{1-\frac{\left(\frac{E_F}{E_M}-1\right)}{\left(\frac{E_F}{E_M}+\xi\right)}v_F} \right)$	(18)
Nielsen (1979)	$E_C = E_M \left(\frac{1+(K_E-1)\left(\frac{\frac{E_F}{E_M}-1}{\frac{E_F}{E_M}+(K_E-1)}\right)v_F}{1-\left(\frac{\frac{E_F}{E_M}-1}{\frac{E_F}{E_M}+(K_E-1)}\right)\left(1+\frac{(1-v_{F,max})\,v_F}{v_{F,max}^2}\right)v_F} \right)$	(19)

Note: moduli of matrix E_M and filler E_F, filler volume content v_F, parameter χ determining stress transfer between fiber and matrix, geometry factor ξ, Einstein coefficient K_E and maximum volume fraction $v_{F,max}$

Other models assume the formation of a third phase between filler and matrix, e.g. models of Christensen-Lo [67] and Takayanagi [68]. However, these models require additional material parameters which are not all measurable by standard test methods but complex and elaborate fitting procedures.

1.5 Modeling the viscoelastic creep behavior

For composites, the creep behavior depends on the viscoelastic mechanical properties of matrix and dispersed phase (fibers or particles), the filler volume content v_F, the interfacial adhesion k_{adh} between filler and matrix and the spatial orientation of the dispersed phase. Furthermore, the experimental parameters such as temperature and initial stress influence creep and creep rate [69]. The creep under constant load is divided in three regimes having different time dependencies, Fig. 13 [70]. After the instantaneous elastic deformation due to

applied initial stress primary creep starts and is characterized by a decreasing creep rate. The regime of secondary creep is reached when the creep rate becomes almost constant. Finally, the creep rate increases again indicating tertiary creep behavior ending in necking or fracture.

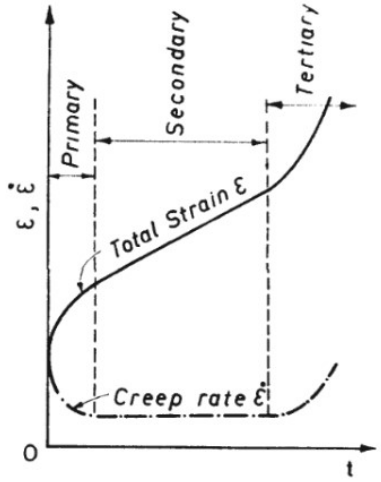

Fig. 13 Time dependent strain and strain rate with the regimes of primary, secondary and tertiary creep [70].

Two categories of quantitative approaches were developed to describe the measured creep behavior of polymers and composites, Table 5.

The measured creep curves can be evaluated in two ways:

1. Developing a rheological model consisting of elastic elements (springs) and viscous elements (dashpots).
   The viscoelastic behavior is generated by appropriate arrangements of Maxwell and Voigt elements [70], Fig. 14, and allows for the evaluation of the creep curves in terms viscosities of dashpots and stiffnesses of springs.
2. Finding appropriate mathematical functions that fit to the creep curves. The coefficients of the function are measures for the creep behavior [71].

Table 5 provides an overview over commonly used models and functions.

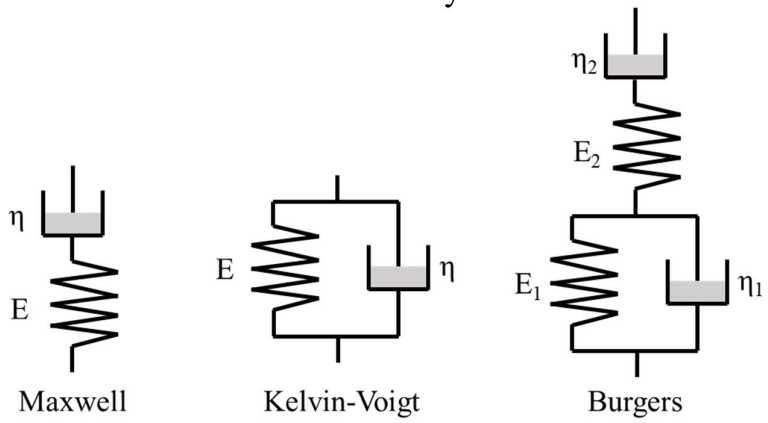

Fig. 14 Rheological models formed by elastic elements (springs) and viscous elements (dashpots).

The empirical functions of Findley [70], Eq. (22), and its modified counterpart [74], Eq. (23), describe creep with an elastic strain and a transient, non-elastic strain. Eq. (22) was employed to describe creep for a variety of materials, such as metals [70], concrete [75], and polymers [76-78]. However, some materials show a non-linear viscoelastic behavior in cases of higher initial stresses. Thus, Eq. (23) provides successful estimates of long-term creep on the basis of short-term creep data at higher stress levels.

In literature, the Burgers model and Findley power law model are most frequently used to describe the creep behavior of polymers and PMC. Other models of Table 5 may provide suitable and good adjustments to measured creep behavior using exponential and power functions or power series [79-81], Eq. (24) – (26), but are less common.

Table 5 Summary of time- and stress-dependent creep models for polymers [70-73].

models	**creep strain/creep compliance**
Burgers	$J(t,\sigma_0)=\left(\frac{1}{E_1}+\frac{1}{E_2}\left(1-e^{-\frac{E_2}{\eta_2}t}\right)+\frac{t}{\eta_1}\right)$ (20) with time t, initial stress σ_0, stiffnesses of Burgers model E_1, E_2 and viscosities of Burgers model η_1, η_2
modified Burgers	$J(t,\sigma_0)=\left(\frac{1}{E_1}+\frac{1}{E_2}\left(1-e^{-\frac{t}{(a\tau^b)}}\right)+\frac{t}{\eta_1}\right)$ (21) with relaxation time τ and fitting parameters a and b
Findley power law	$J(t,\sigma_0)=\frac{\varepsilon_0}{\sigma_0}+\frac{\varepsilon^+}{\sigma_0}t^n=\frac{1}{E_1}+\frac{\varepsilon^+}{\sigma_0}\left(\frac{t}{t_1}\right)^n$ (22) with initial strain ε_0, transient strain ε^+, exponent n, reference time t_1
Findley modified power law	$J(t,\sigma_0)=\frac{\varepsilon_0}{\sigma_0}\sinh\left(\frac{\sigma_0}{\sigma_1}\right)+\frac{\varepsilon^+}{\sigma_0}t^n\sinh\left(\frac{\sigma_0}{\sigma_1}\right)$ (23) with reference stress σ_1
Bailey–Norton	$J(t,\sigma_0)=A\,\sigma_0^{m-1}\left(\frac{t}{t_1}\right)^{n^+}$ (24) with coefficient A and exponents m and n^+
Power series	$J(t,\sigma_0)=J_0+\sum_{i=1}^{m}J_i\left(\frac{t}{t'}\right)^i$ (25) with reference time t', relaxation strengths J_i and index i
Prony–Dirichlet series	$J(t,\sigma_0)=J_0+\sum_{i=1}^{m}J_i\left(1-e^{\left(-\frac{t}{\tau_i}\right)}\right)$ (26) with relaxation times τ_i

1.6 Numerical simulations of mechanical behavior

Due to the complex orientations and arrangements of fibers or filler particles in polymer composites, the experimental characterization of the mechanical behavior is not only supplemented by theoretical derivations but also by numerical simulations. The representative volume element (RVE) based on the finite element method (FEM) allows for mechanical modeling of composites systems by upscaling the mechanical response of a smallest representative unit to the whole bulk behavior [82], Fig. 15.

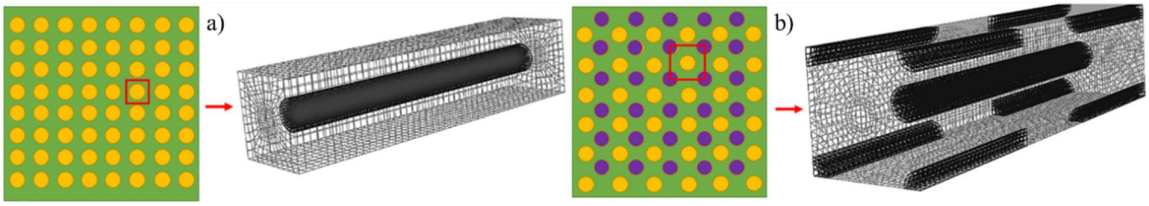

Fig. 15 Two examples of representative volume elements (RVE) of a unidirectional short fiber reinforced composite – a) regular and b) staggered fiber array packing geometry [82].

For defined properties of the constituent materials including elastic or viscoelastic parameters, volume content of dispersed phase, aspect ratio etc., the construction of a RVE yields a mechanical response in terms of the predefined FEM model approach. Pathan et al. [83] and Gusev [84] used the RVE method to calculate the viscoelastic moduli of both unidirectionally aligned continuous fiber (CFRC) and short glass fiber reinforced composites (SGFRC), respectively. Pathan et al. assumed unidirectional linear elastic isotropic fibers embedded in a linear viscoelastic matrix. The probability distributions of all viscoelastic properties by conducting Monte Carlo analyses showed that the theoretical models of Mori-Tanaka [85] and Lielens [86] are the most suitable in predicting the anisotropic viscoelastic response compared to the RVE. Gusev determined viscoelastic stiffnesses of SGFRC based on Monte Carlo models with various fiber orientation distributions (FOD) and found that they correlate well with stiffnesses to the constant strain orientation averaging procedure according to Voigt [84]. Simulations of Ansari et al. [87] showed that the transverse creep-recovery behavior of polymer nanocomposites containing carbon nanotubes is mainly influenced by the nonlinear viscoelastic creep of polymer matrix and interphase material if the load is increased, Fig 16. Relaxation was successfully simulated by Tang et al. [88] who studied the effective stress relaxation stiffness coefficients of a RVE composite containing continuous fiber reinforcements (CFRC).

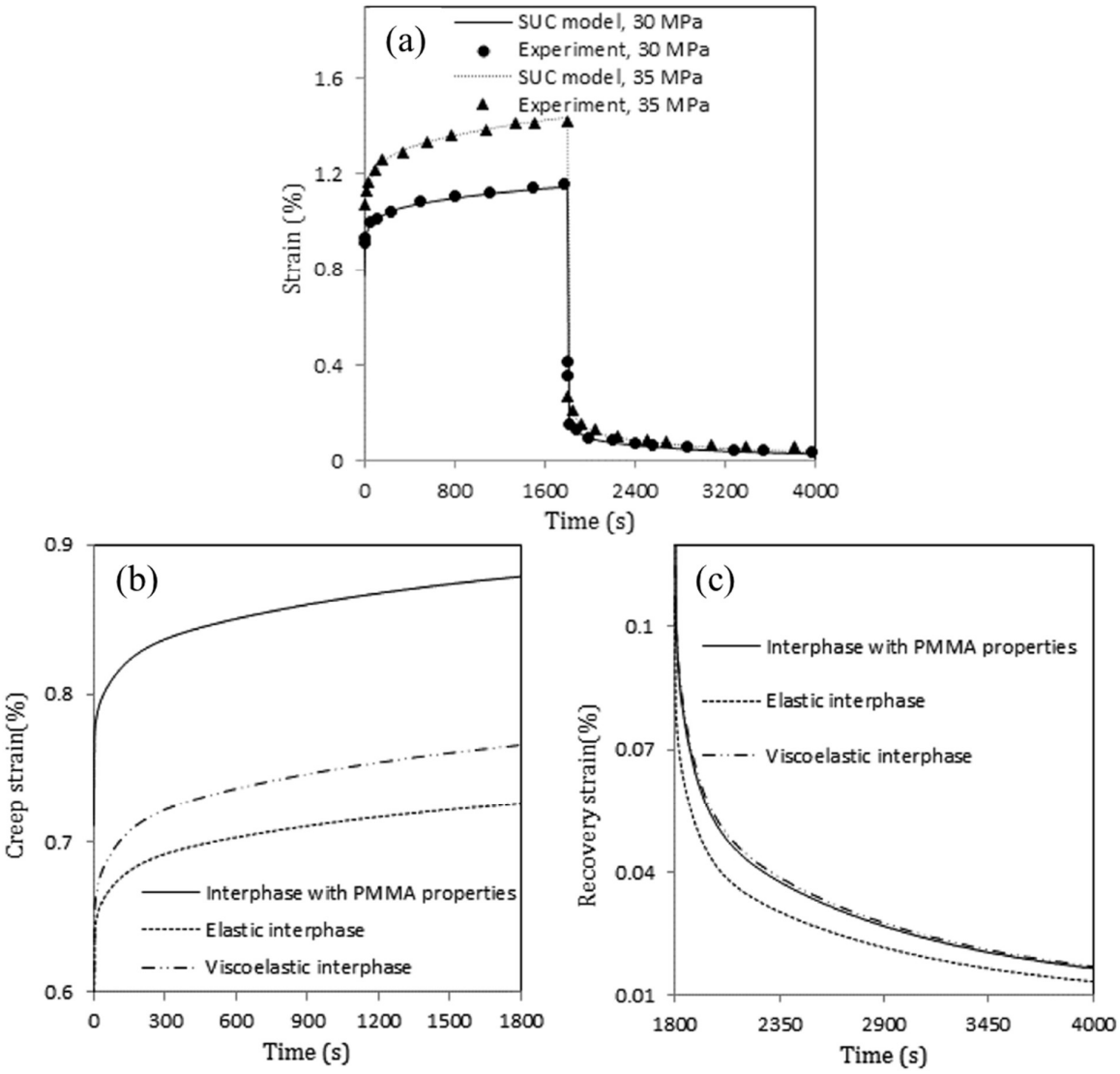

Fig 16 Experimental and simulated creep-recovery curves of neat PMMA at different loading levels (a) supplemented by the simulated interphase behavior of (b) creep and (c) recovery strains of CNT/PMMA composites under transverse loading [87].

1.7 Determination of materials properties

Common methods used to determine elastic, viscoelastic and time-dependent behavior of materials are listed in Table 6. Polymers and polymer composites, especially fiber reinforced ones, exhibit an anisotropic mechanical behavior due to orientations of macromolecules or the dispersed phase during processing and must be considered. Therefore, it is useful to measure material properties taking into account loads acting e.g. parallel or perpendicular to the present orientation.

Table 6 Overview of methods to determine elastic and viscoelastic properties.

method	standard	material parameter	particularities
tensile test	DIN EN ISO 527-1 ASTM D638-02	Young´s modulus E yield stress σ_y tensile stress σ_m stress at break σ_b corresponding strain values ε Poisson´s ratio μ	modulus is determined at 1 mm/min, remaining σ-ε-behavior > 1 mm/min
dynamic mechanical analysis	DIN EN ISO 6721-1	complex modulus E^*, G^*, K^* storage modulus E', G', K' loss modulus E'', G'', K'' phase shift δ damping behavior tan δ	frequency and temperature dependent viscoelastic stiffness
impulse excitation technique	ASTM E1876-22	longitudinal modulus E_l flexural modulus E_f shear modulus G_t Poisson´s ratio μ	non-destructive method using resonant frequencies
creep experiments	ISO 899-1	creep modulus $E(t)$ creep compliance $J(t,\sigma_0)$ creep strain $\varepsilon(t)$	impact-free force application without overshooting, creep times > 1000 h possible

1.7.1 Tensile test

For tensile tests (TT), the uniaxial constant deformation rate yields in a homogenous cross-sectional stress state of the specimen. Normally the stress-strain-curves are evaluated with respect to mechanical properties according to DIN EN ISO 527-1. However, this often underestimates the Young's moduli at higher deformation rates due to initial effects of the machinery for reaching a constant strain rate. To overcome this "problem", the stress-strain-curves can be evaluated using the viscoelastic stress-strain-function (VSSF), Eq. (27) [89]:

$$\sigma(\varepsilon) \underbrace{\cong}_{\varepsilon<\varepsilon_R} E\,\varepsilon_R\left(1-e^{-\frac{\varepsilon}{\varepsilon_R}}\right) \tag{27}$$

with stress $\sigma(\varepsilon)$, strain ε, relaxation strain ε_R and strain rate dependent Young´s modulus E.

Furthermore, the Poisson´s ratio μ can be obtained by simultaneous measurement of the time dependent deformation parallel and perpendicular to the load direction [90]. Here, a second strain gauge, a laser extensometer or a video extensometer is used to acquire length and width data simultaneously resulting in

$$\mu = \frac{\Delta w * l_0}{\Delta l * w_0} \tag{28}$$

with change in length Δl, change in width Δw, initial length l_0, and initial width w_0.

Several studies show the influence of fiber and filler orientation reflecting the anisotropic mechanical behavior. Fig. 17 depicts the change of stress-strain-behavior with respect to loading direction for poly(butylene terephthalate) and polyamide 6 composites yielding in higher moduli and tensile strength but lower ductility parallel to the fiber orientation direction.

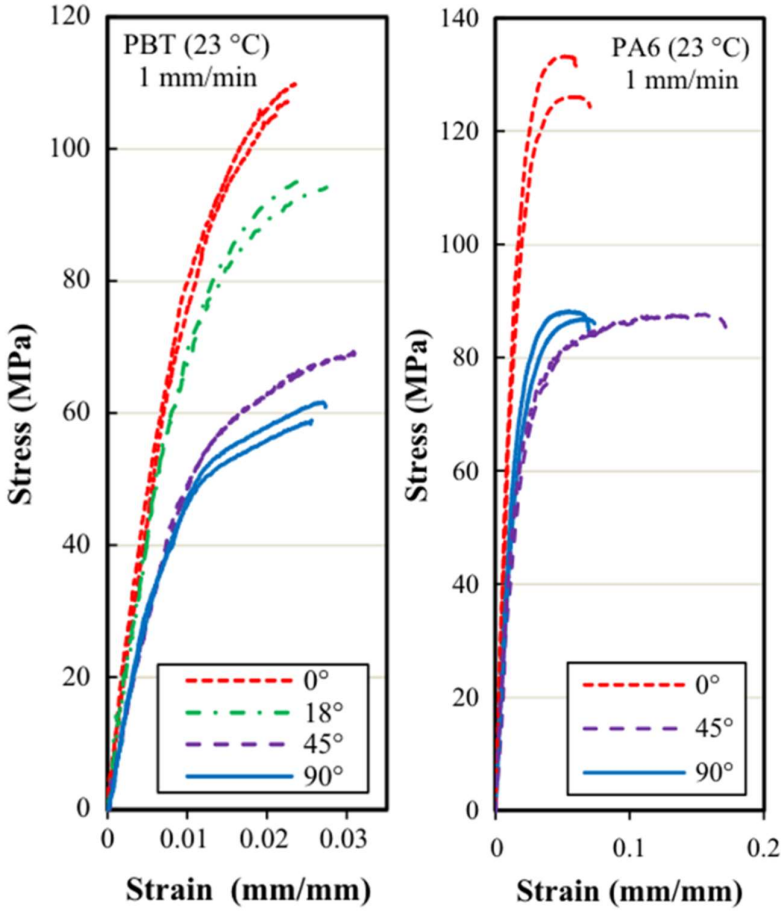

Fig. 17 Stress-strain behavior of PBT/GF30 and PA6/GF35 with 10 % rubber impact modifier tested at varying angles to the mold flow direction [91].

De Monte et al. [92] investigated 1, 2, and 3 mm thick specimens of SGFRC PA66 to study the effect of fiber orientation on tensile behavior at varying angles with respect to the mold flow direction. Young's moduli and tensile strength of 1 mm thick specimen decreased 44 % and 45 %, respectively, with increasing angles from 0° to 90°. This behavior was less pronounced for thicker specimens (Young´s modulus: 1 mm: 44 % and 3 mm: 18 %) which was attributed to higher contributions of the core regions with a preferential fiber orientation perpendicular to the flow direction, Fig. 6. Similar findings were presented by Zhou and Mallick [93] and Wang et al. [94] for injection molded rods and plates of SGFRC of PA66 (ΔE_C = 43 %, $\Delta \sigma_{y,C}$ = 35 %) and PA6 (ΔE_C = 50 %, $\Delta \sigma_{y,C}$ =

50 %), respectively. In e.g. glass beads reinforced composites angular dependencies are only attributed to processing induced orientations of the polymer matrix [95, 96]. Weon and Sue [97] investigated the mechanical behavior of nylon-6/clay nanocomposites with varying aspect ratios (r = 131, 98, 80) and showed that modulus (E = 4.67, 4.09, 3.80 GPa) and yield stress (σ_y = 98, 93, 89 MPa) decreased with decreasing clay aspect ratio and degree of orientation.

1.7.2 Dynamic mechanical analysis

The dynamic mechanical analysis (DMA) is a technique to determine viscoelastic properties of polymers as a function of frequency ω and temperature T under sinusoidal oscillating load (controlled stress mode) or deformation (controlled strain mode). A great variety of sample holders is available to measure under bending (3PB), tensile, compression, and shear properties. The viscoelasticity of polymers generates a phase shift between excitation and response, Fig. 18. A phase shift of 0° corresponds to a purely elastic behavior, a phase shift of 90° to a purely viscous behavior.

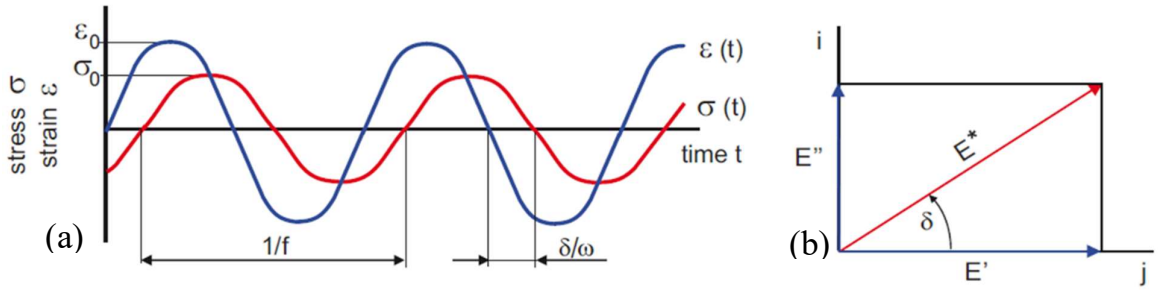

Fig. 18 Sinusoidal oscillation of strain-controlled DMA with input ε(t), response σ(t), and phase shift δ (a); diagram of the complex modulus in the complex plane with j = storage modulus E′, i = loss modulus E′′ (b) [90].

For strain controlled measurements the strain $\varepsilon(\omega,t)$ is given by

$$\varepsilon(\omega,t) = \varepsilon_0(\omega)\, sin(\omega t) = \varepsilon_0(\omega) * e^{i(\omega t)} \tag{29}$$

with strain amplitude $\varepsilon_0(\omega)$. The corresponding measured stress response $\sigma(\omega,t)$ is

$$\sigma(\omega,t) = \sigma_0(\omega)\,(sin(\omega t) + \delta(\omega)) = \sigma_0(\omega) * e^{i(\omega t+\delta(\omega))} \tag{30}$$

with stress amplitude $\sigma_0(\omega)$ and phase angle δ. The complex modulus $E^*(\omega)$ is calculated to

$$E^*(\omega) = \frac{\sigma_0(\omega) * e^{i(\omega t+\delta(\omega))}}{\varepsilon_0(\omega) * e^{i(\omega t)}} = \underbrace{E_0(\omega)\cos\delta(\omega)}_{\text{storage modulus } E'} + i\,\underbrace{E_0(\omega)\sin\delta(\omega)}_{\text{loss modulus } E''} \tag{31}$$

with storage modulus *E*' as a measure of the stored energy, loss modulus *E*'' as a measure of the dissipated energy. The loss factor tan δ characterizes the damping behavior

$$\tan\delta(\omega) = \frac{E''(\omega)}{E'(\omega)} \tag{32}$$

DMA measurements in torsion (DMA-OT) allow for determining the torsional or shear modulus *G* by oscillatory twisting of a rod-like or rectangular specimen, Fig. 19.

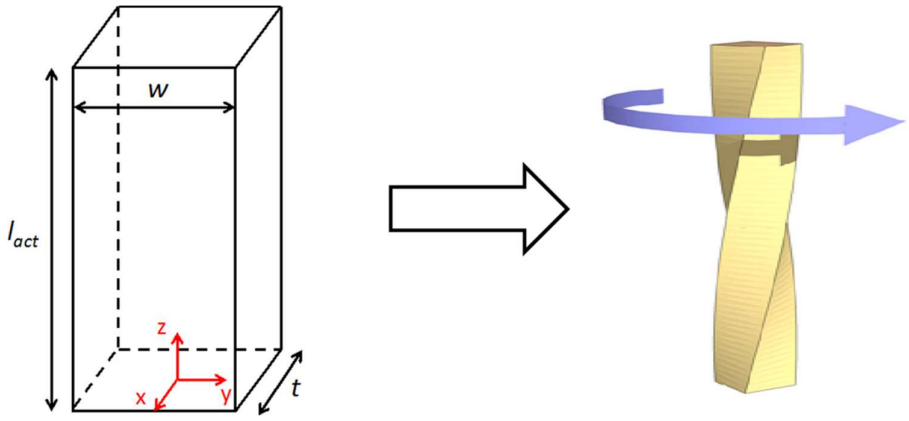

Fig. 19 The torsion of a rectangular test bar having the geometry of width w, thickness t, and the active length l_{act} which is not clamped [98].

For a cylindrical rod, the torsional deformation in the linear regime evokes a linear radius-dependent σ-ε-correlation. Consequently, only shear stress components exist in the sample without stresses normal to the cross-section. However, the torsion of rectangular test bars elicits a non-linear stress distribution over the cross-section and depends on the angular position along the active clamping length l_{act}. Thus, the data have to be evaluated according to *de Saint-Venant* [99] to get the correct storage shear modulus G'^{OT} of a rectangular test bar:

$$G'^{OT} = \frac{M}{J_t \xi} = \frac{M}{\theta} \frac{3 l_{act} * 1000 * g}{w t^3 g(u)} \; with \; g(u) = \frac{1 - 0.378 u^{-2}}{1 + 0.6 u^{-1}} \tag{33}$$

with torque *M*, polar moment of inertia J_t, deformation twist ξ, active length l_{act}, angular displacement θ, width *w* and thickness *t* of the specimen, gravity constant *g*, and $u = w/t$ as the aspect ratio of the bar.

Comparing different excitations and load directions is a sophisticated issue for understanding the influence of morphological and/or fiber or particle orientations on the mechanical behavior. Huayamares et al. [100] compared the viscoelastic properties of quasi-isotropic glass fiber and carbon fiber reinforced epoxies to unidirectional glass fiber reinforced epoxies using DMA-3PB and DMA-OT. They found continuously higher flexural moduli compared to the moduli

calculated from shear modulus G in oscillatory torsion tests. Their conclusion was a lack of proportionality through the Poisson´s ratio between G and E for the investigated materials. Serra-Aguila et al. [101] determined the Young´s moduli of PA66 using TT at strain rates ranging from 1 to 500 mm/min and DMA-3PB at varying frequencies ranging from 0.02 to 12 Hz. They found that tensile modulus exceeds bending modulus by a factor 1.2. An analytical approach was applied by implementing a logarithmic adjustment to convert the frequency-dependent bending moduli to strain rate-dependent tensile moduli or vice versa for varying strain rates and temperatures. Junaedi et al. [102] presented that the mechanical behavior of reinforced polypropylene (PP) depends on the loading direction. Injection molded test bars of a neat PP and composites containing particles with different aspect ratios (milled short carbon fibers, graphite nano-platelets, and titanium dioxide nanoparticles) were investigated in 3PB and TT. Both, the neat material and the composites showed lower bending moduli than tensile moduli independently of aspect ratio. This can be either attributed to different loading states or indicates inhomogeneous mechanical behavior due to shear flow induced orientations of fillers and chain orientations yielding in skin core arrangements.

1.7.3 Impulse excitation technique

The impulse excitation technique (IET) is a non-destructive testing method that determines elastic moduli via vibration mode dependent resonant frequencies measured after an impulse excitation [103]. The procedure is described in the ASTM E1876-22 and is well-established for ceramics and metals [104-106] but hardly for PMC. When comparing properties determined by IET one has to keep in mind that it uses much smaller deformation amplitudes, and larger resonant frequencies compared to DMA leading to higher moduli for IET than for DMA and TT.

For flexural excitation, the specimens are placed on supports located at the vibration nodes of the flexural excitation. A contactless transducer is positioned close to the antinode point and the mechanical impulse is applied at the center of the specimen, Fig. 20. The flexural modulus is determined via the measured flexural resonant frequency

$$E_\mathrm{f} = 0.9465\left(\frac{m f_\mathrm{f}^2}{w}\right)\left(\frac{l^3}{t^3}\right)T_1 \tag{34}$$

$$\text{with } T_1 = 1 + 6.585(1 + 0.0752\mu + 0.8109\mu^2)\left(\frac{t}{l}\right)^2 - 0.868\left(\frac{t}{l}\right)^4 - \left(\frac{8.340(1+0.2023\mu+2.173\mu^2)\left(\frac{t}{l}\right)^4}{1.000+6.338(1+0.1408\mu+1.536\mu^2)\left(\frac{t}{l}\right)^2}\right) \tag{35}$$

with flexural modulus E_f, resonant frequency f_f, mass m, length l, width w, and thickness t of the specimen. T_1 depicts the geometry factor for flexural excitation being dependent on Poisson ratio μ.

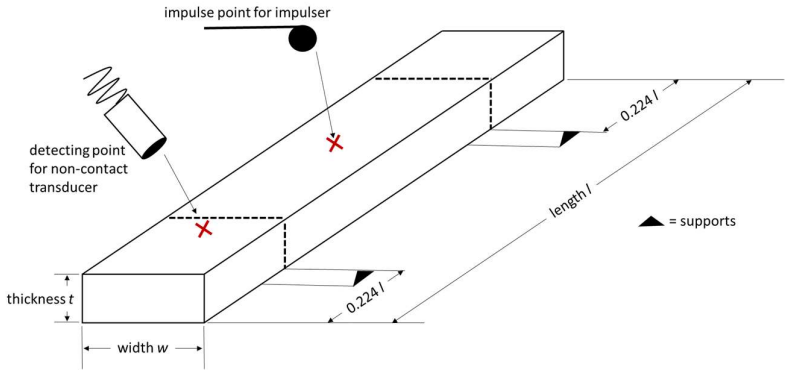

Fig. 20 Schematic of flexural resonant impulse excitation with a rectangular specimen [107].

For longitudinal excitation the specimens are placed on torsional nodes at the midpoints of length and width, the resonant frequency is detected on one end and the mechanical impulse is applied on the other end, Fig. 21.

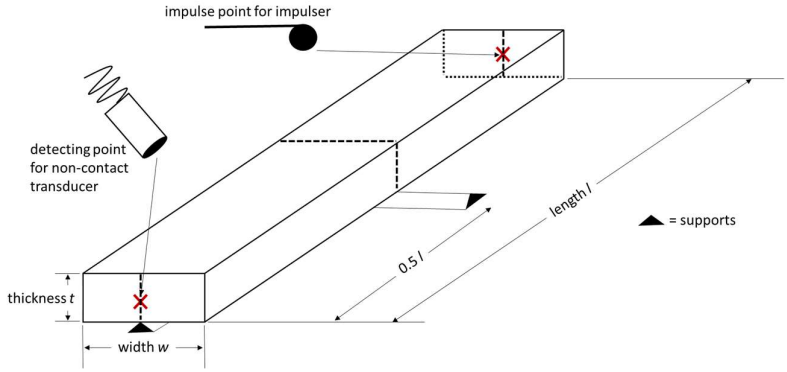

Fig. 21 Schematic of longitudinal resonant impulse excitation for rectangular specimen [107].

The longitudinal modulus is determined via the measured longitudinal frequency

$$E_l = 4mf_l^2\left(\frac{l}{btK}\right) \tag{36}$$

$$\text{with } K = 1 - \left(\frac{\pi^2\mu^2}{8l^2}\frac{2(w^2+t^2)}{3}\right) \tag{37}$$

with longitudinal modulus E_l and longitudinal resonant frequency f_l. K is the geometry factor for longitudinal excitation being dependent on Poisson ratio μ.

For torsional excitation the specimen is placed on the torsional nodes, the mechanical impulse is applied on specimen top at 0.224*l, and the resonant

frequency is measured on the mirrored nodal point of flexural vibration to avoid the detection of spurious flexural vibration frequencies, Fig. 22.

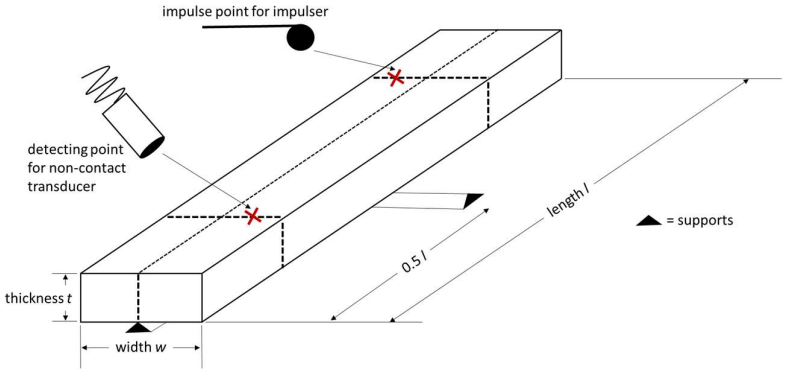

Fig. 22 Schematic of torsional resonant impulse excitation for rectangular specimen [107].

The torsional resonant frequency yields the shear modulus G_t

$$G_t = \left(\frac{4lmf_t^2}{wt}\right) * \left(\frac{B}{1+A}\right) \tag{38}$$

$$\text{with } B = \frac{\frac{w}{t}+\frac{t}{w}}{4\left(\frac{t}{w}\right)-2.52\left(\frac{t}{w}\right)^2+0.21\left(\frac{t}{w}\right)^6} \text{ and} \tag{39}$$

$$A = \frac{0.5062 - 08776\frac{w}{t} + 0.3504\left(\frac{w}{t}\right)^2 - 0.0078\left(\frac{w}{t}\right)^3}{12.03\frac{w}{t} + 9.892\left(\frac{w}{t}\right)^2} \tag{40}$$

with torsional resonant frequency f_t and geometry factors B and A.

Finally, the Poisson's ratios μ_f and μ_l can be determined iteratively using the flexural and longitudinal excitation mode

$$\mu_f = \frac{E_f}{2G_t} - 1 \qquad \mu_l = \frac{E_l}{2G_t} - 1 \tag{41}$$

1.7.4 Tensile creep experiments

The time dependent deformation increase under constant load is measured by creep experiments according to ISO 899-1. The load is applied within 1 – 5 s and kept for the chosen time at constant temperature and humidity [69]. Creep strains decrease with increasing filler content and interfacial adhesion [108-110]. Increasing loads and temperatures enhance both creep strain and creep rate [110, 111]. Furthermore, the orientation distribution of platelet fillers or fibers with respect to the load direction has significant effects on the creep behavior. Hao et al. [112] investigated the anisotropic creep behavior of extruded natural fiber reinforced HDPE plates at varying angles having different fiber orientations and aspect ratios. They summarized that the on-axis creep resistance increases as the

aspect ratio increases due to a higher load-carrying capacity. However, higher aspect ratios yield in a more pronounced anisotropic morphology with enhanced creep strains perpendicular to fiber orientations, Fig. 23.

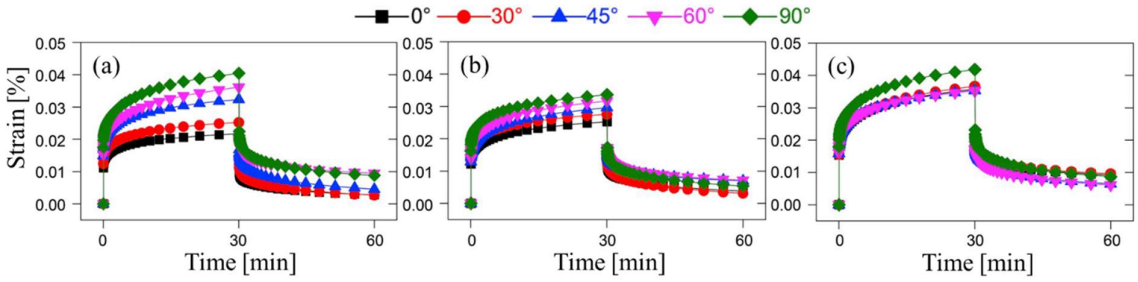

Fig. 23 Creep strains of natural fiber reinforced HDPE samples at different angles between load and extrusion direction [112] - (a) poplar wood, (b) radiata pine, (c) rice husk.

1.8 Characterization of interfacial adhesion

The interfacial adhesion is relevant for the load transfer from matrix to filler particles and fibers. Thus, it affects the mechanical properties modulus, tensile strength and toughness. Quantitative and qualitative evaluation of interfacial adhesion properties includes various sophisticated approaches to comprehend the occurring stress concentrations at the interface. These may arise either from different thermal expansion coefficients between filler and matrix or different strength properties of both materials. Interface properties characterizing methods can be divided in three categories – physical/chemical, microscopic, and mechanical methods [113].

1.8.1 Physical and chemical methods

For PMC, the wettability of the filler or fiber surface is crucial as it yields physical attraction amongst atoms of filler and matrix. Wetting depends on the differences of their surface energies. The adhesion arises from Van der Waals forces, hydrogen bonding forces or acid-base interactions [114].

A quantitative measure of the wetting behavior is the contact angle θ that is formed if a drop wets a surface, Fig. 24. It is linked to the surface energy and surface energy via Young's equation [114], Eq. 42,

$$\sigma^{sv} = \sigma^{sl} + \sigma^{lv} \cos\theta \tag{42}$$

with solid/liquid interfacial tension σ^{sl}, solid surface free energy σ^{sv}, liquid surface tension σ^{lv}, and contact angle θ.

The more similar the surface energies the better the wettability and the interfacial adhesion.

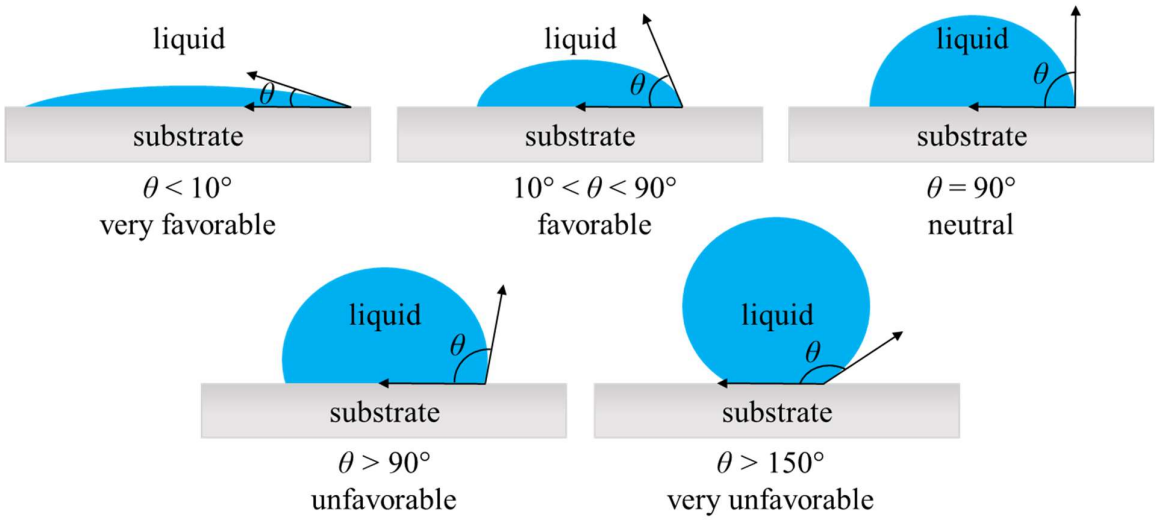

Fig. 24 Wetting behavior of a liquid-solid interface measured by contact angle.

Surface energies can be modified by e.g. corona, plasma, or chemical treatments. In Table 7 surface energies of various solids are listed and serve as a comparison of compatibility.

Table 7 Overview of surface energies for several polymer matrices and dispersed phases.

surface energy [mJ/m^2]			
matrix [115-117]		dispersed phase [118-121]	
PA66	38 to 55	glass beads	40 to 60
PBT	44 to 49	glass fibers	32
BR	26 to 27	aramid fibers	18 to 32
PE-LD	33 to 35	carbon fibers	40 to 50
iPP	31 to 42	carbon black	150 to 170

1.8.2 Microscopic methods

Microscopic methods such as atomic force microscopes (AFM) or SEM provide information of surface roughness and interfacial adhesion of filled systems.

AFM generates topographic images by raster scanning an ultra-sharp tip over the sample surface. Occurring physical interactions between probe and sample surface yield in a deflection of the cantilever, which is reflected by a laser beam and subsequently detected as a height change in a photodiode signal. The height resolution can be as low as 5 – 10 pm, whilst the lateral resolution ranges from sub-nm to a few nm and are both a function of the AFM and tip quality allowing for a quantitative analysis of specimen´s topography [122]. The AFM provides the opportunity to measure the surface roughness of fillers or fibers which plays an important role for the extent of mechanical interlocking at the interface. The

liquid matrix flows in the crevices, solidifies and creates physical interlockings leading to a better interfacial adhesion due to a larger surface area.

Vecchiato et al. [123] showed how different surface treatments alter the morphology of PET fibers and the interfacial adhesion due to an increased surface roughness. Jiang et al. [124] used ultrasonically assisted deposition of carbon nanotubes (CNT) on CF and investigated the modified interfacial properties by roughness measurements using AFM in tapping mode and visualized them using SEM, Fig. 25.

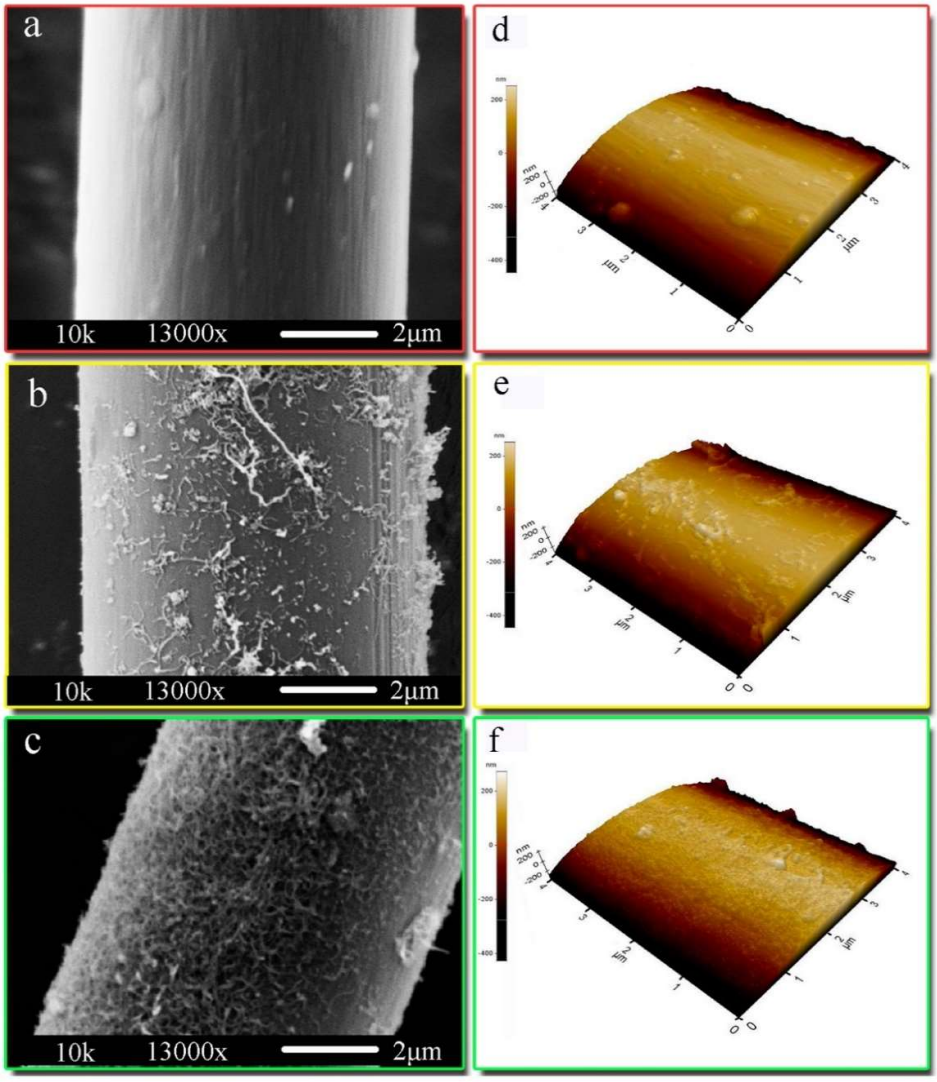

Fig. 25 Scanning electron microscopy (SEM) and atomic force microscopy (AFM) images of carbon fibers (CF) – untreated (a, d), deposited carbon nanotubes (CNT) without ultrasonic (b, e), and with ultrasonic (c, f) [123].

The SEM allows for the investigation of filler or fiber distributions in the matrix, fracture and wetting behavior and a qualitative characterization of the interfacial adhesion between filler and matrix. Fig. 26 shows fracture surfaces of PMC containing CF, graphite, Kevlar fibers, and GF. The CFs are well embedded

and wetted, Fig. 26 (a). Matrix residues on the CF indicate a relatively good fiber matrix adhesion. The individual graphite layers are exfoliated but not wetted, Fig. 26 (b). Kevlar fibers exhibit a ductile fracture pattern and are only slightly wetted with matrix, Fig. 26 (c). The GFs in Fig. 26 (d) exhibit a favorable fiber matrix adhesion and a preferential fiber orientation in load direction whereas the GFs in Fig. 26 (e) represents the "worst-case-scenario" with no or very poor adhesion and fibers oriented perpendicular to the load direction.

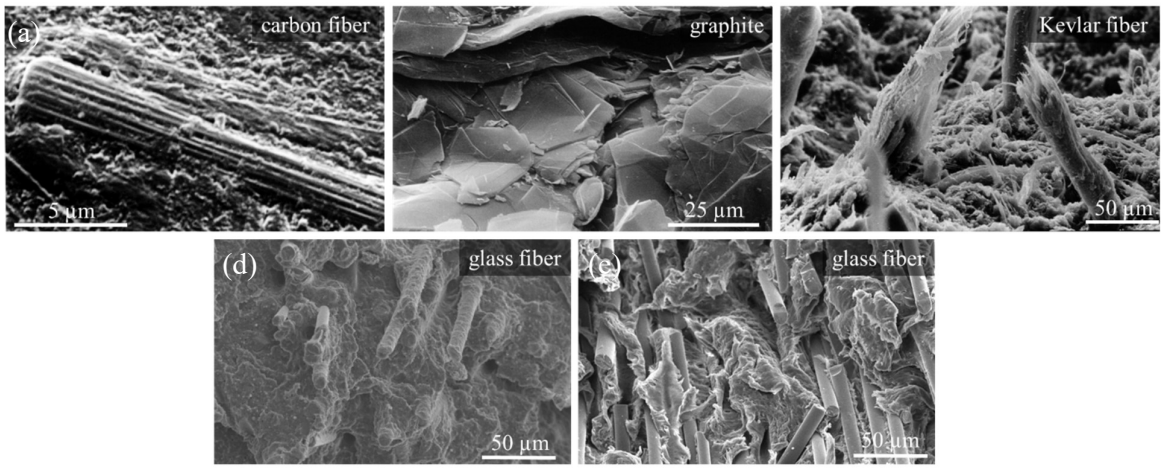

Fig. 26 SEM observations of embedded carbon fiber (a), graphite (b), Kevlar fiber (c), and glass fiber (d), (e) to obtain the filler matrix adhesion [125].

1.8.3 Mechanical methods

The aforementioned mechanical methods provide mechanical properties that are affected indirectly by the interfacial adhesion. However, interfacial strengths can be measured by single fiber tests such as fiber pull-out test (a), micro-bond test (b), or fiber push-through test (c) [126], Fig. 27.

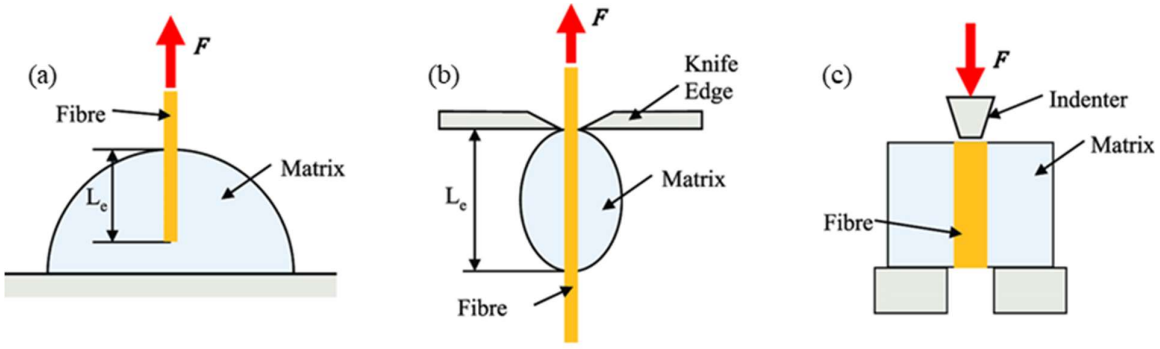

Fig. 27 Microscopic mechanical methods to determine interfacial adhesion – (a) fiber pull-out, (b) microbond, (c) fiber push-through [126].

At first, a single fiber is embedded in the matrix. Then the fiber is pulled out or pushed through and simultaneously a force displacement curve is measured. Zhandarov and Mäder [127] investigated five fiber reinforced (E-glass, basalt, polyvinyl acetate (PVA), carbon, continuous carbon nanotubes (CNT)) matrices

(PP, L20 epoxy, concrete, PA66, RIM epoxy, respectively) to obtain typical force-displacement curves, Fig. 28, from fiber pull-out and micro-bond tests. Subsequently, these curves were evaluated in terms of three energy-based approaches to estimate the interfacial toughnesses.

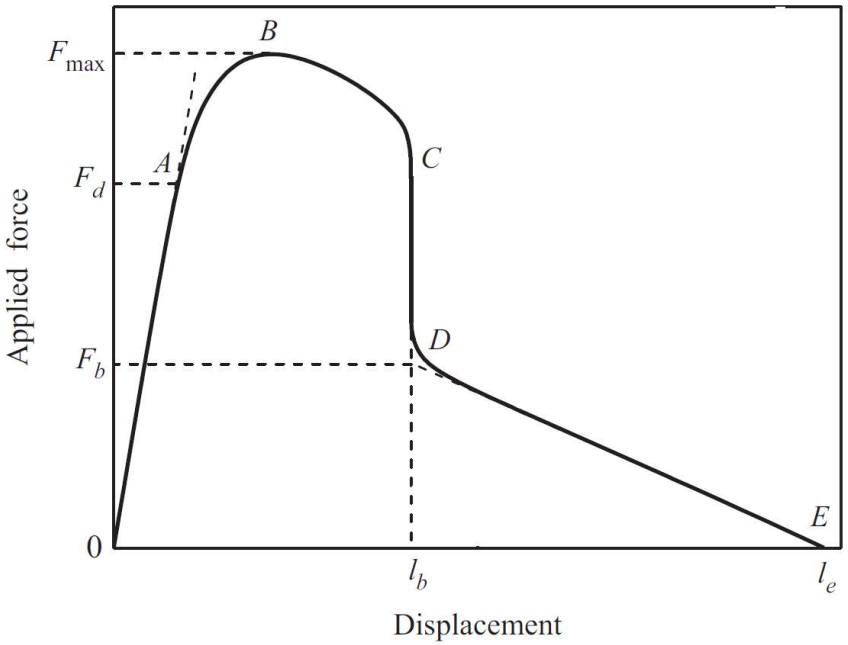

Fig. 28 Idealized force-displacement curve of a pull-out test with segment 0A corresponding to initial loading, interfacial debonding at segment A to D, and occurring "tail" forces in segment DE due to frictional interactions between fiber and matrix [127].

For the composites systems the interfacial toughness decreased in the order basalt/L20 epoxy > carbon/PA66 > CNT/RIM epoxy > E-glass/PP > PVA/concrete. Pardoen et al. [128] showed the methodology and influence of fiber push-through tests and packing density, respectively, obtained for CF composites, Fig. 29.

They highlighted that the load-displacement curves are mainly governed by the friction induced load increase for densely packed areas (black) compared to low volume fiber fraction areas (magenta). Furthermore, displacement-time curves exhibit a displacement jump at the beginning of crack propagation. The slope of the linear region of the load-displacement curve can therefore be seen as a measure of resistance against fiber push-through due to friction or fiber-matrix compatibility with respect to interfacial adhesion.

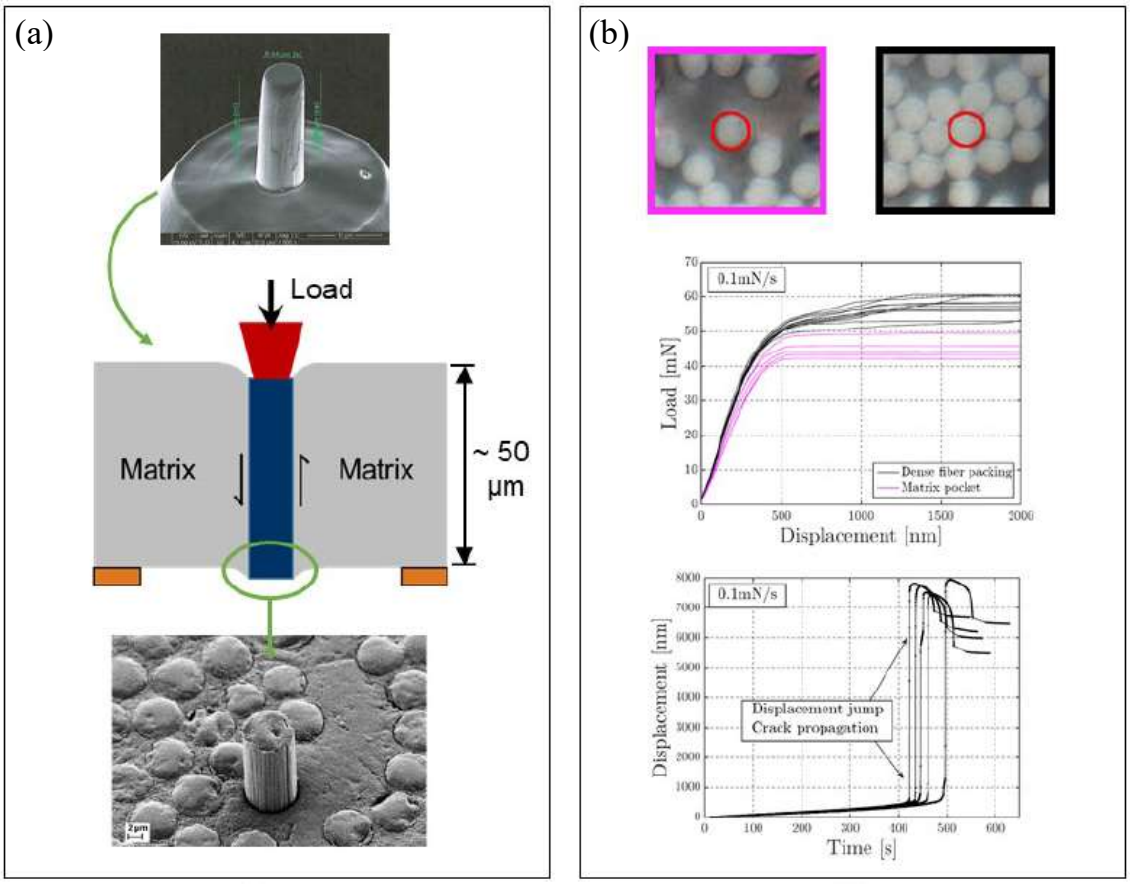

Fig. 29 Methodology and SEM images (a) and resulting micrographs (b) of carbon fiber composites obtained from fiber push-through tests [128].

2 Aim of the work

Polymer matrix composites (PMC) are the materials of choice when it comes to a cost-effective and easy processability. Furthermore, they are adaptable to a great variety of applications with advantaging low densities due to their symbiotically enhanced character of their constituent phases. They are found in a wide range from high performance parts for space flights to the substitution of metals in mass production parts. Nowadays, increasing sustainability demands not only yield in polymeric and filler systems from renewable sources, but contemporary established materials commodities are recycled, recompounded and reused. This leads to the necessity of a fast availability of relevant mechanical properties.

The mechanical behavior of PMC must be known to affirm its functioning during application. The materials characterization often comprises measurements of the time-dependent viscoelastic behavior. Well established and standardized methods e.g. tensile test, dynamic mechanical analysis, or oscillatory torsion are known to describe the viscoelastic behavior in terms of Young´s modulus E, shear modulus G, and Poisson´s ratio μ, while long-term creep compliance $J(t)$ is usually determined by tensile creep measurements. However, the issue "interfacial adhesion" is often ignored although it is a crucial quantity in materials. Therefore, the aim of this work is to **generate progress in the field of efficient testing and accurate modeling** and addresses the following tasks:

- **implementation** of the impulse excitation technique as a non-destructive method to determine mechanical properties based on its comparison to standardized methods for PMC
- gaining a comprehensive understanding of the elastic behavior of PMCs under various loading conditions by employing non-destructive testing and integrating morphological and thermal investigations to **correlate microstructural features with the mechanical respons**e
- developing a model that allows to **introduce interfacial adhesion** to attribute changes in mechanical performance with respect to the elastic and time-dependent viscoelastic behavior considering the load transfer between filler and matrix.
- **modeling the creep behavior** of PMC as a function of matrix creep and a time-dependent interfacial adhesion function for GB composites and introducing fiber orientation effects for GF composites to enable a more accurate representation of long-term composites performance.

The mechanical behavior of PA66 and PBT composites reinforced with varying contents of glass beads is investigated with the focus on elastic quantities determined by tensile test, dynamic mechanical analysis, oscillatory torsion, and impulse excitation technique. The experimental findings are correlated to finite element analysis and morphological investigations such as skin core structures of

crystalline regions and filler distributions. Furthermore, thermo-physical investigations (by DSC) are performed to support the aforementioned findings.

Besides a comprehensive and elaborate thermo-mechanical analysis of particulate reinforced composites, another task of the PhD work is the focus on modeling the viscoelastic behavior considering interfacial adhesion effects on the base of an appropriate two-phase model to predict reliable Young´s moduli E and creep compliances $J(t)$ of particulate and fiber reinforced composites.

The long-term goal is a thorough understanding of reinforcing mechanisms which is further implemented in a modeling approach to calculate the mechanical behavior of PMC. If these interfacial adhesion effects are known for different composites systems, the modeling provides a simple and fast approach to calculate relevant mechanical properties compared to a time-consuming and elaborate thermo-mechanical analysis.

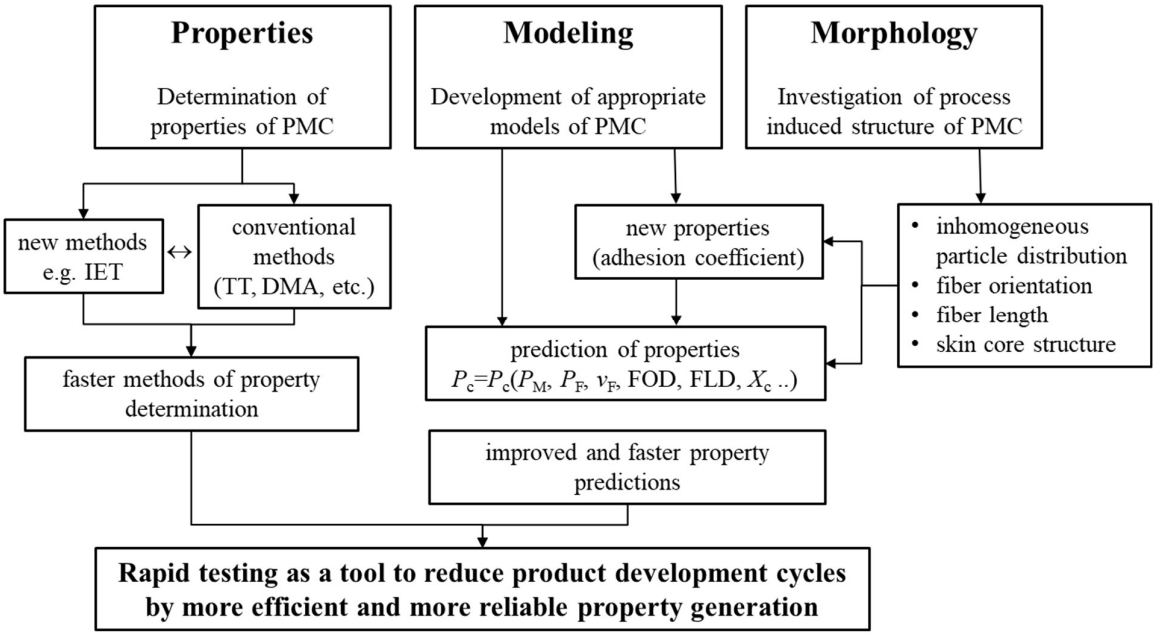

Fig. 31 Flow chart of methodology and techniques employed in the PhD thesis.

3 Materials and methods

The materials investigated to determine elastic and viscoelastic properties were commercially available polyamide 66 (PA66) and poly(butylene terephthalate) (PBT) reinforced with various amounts of glass beads (GB) as spherical inclusions and short glass fibers (GF), Table 8.

Table 8 List of PMC showing matrix polymer, brand name, GB/GF content, Young´s modulus and density according to technical data sheet (TDS).

matrix	filler	brand name	GB/GF content w_F [%]	GB/GF content v_F [-]	Young's modulus E [MPa]	density ρ [g/cm³]
PA66	GB	RADIPOL[1] A45	0	0	3200	1.14
		AKROMID[2] A3 GK 30	30	0.16	5000	1.35
		AKROMID[2] A3 GK 40	40	0.23	5500	1.44
PBT	GB	Ultradur[3] B 2550	0	0	2500	1.30
		Ultradur[3] B 4300 K4	20	0.12	3500	1.45
		Ultradur[3] B 4300 K6	30	0.19	4000	1.53
PBT	GF	Vestodur[4] 2000	0	0	2500	1.31
		Ultradur[3] B 4300 G4	20	0.09	7000	1.45
		Ultradur[3] B 4300 G6	30	0.13	9700	1.53
	GB				63000	2.5
	GF				74000	2.56

[1] brand name of Radici Group, Gandino, Italy (Radici group. Technical data sheet Radipol A45 (2018))
[2] brand name of AKRO-PLASTIC GmbH, Niederzissen, Germany (AKRO-PLASTIC GmbH. TDS AKROMID A3 GK 30 1 natur (36739), AKROMID A3 GK 40 1 natur (1803))
[3] brand name of BASF SE, Ludwigshafen, Germany (BASF. TDS Ultradur B 2550, Ultradur B 4300 K4, Ultradur B 4300 K6, Ultradur B 4300 G4, Ultradur B 4300 G6)
[4] brand name of Evonik Operations GmbH, Wittenburg, Germany (Evonik. TDS Vestodur 2000)

The elastic properties of injection molded test bars (type 1A according to ISO 527- 2) of polar PA66 and PBT GB composites were determined after annealing for 4 hours at 180 °C to minimize effects of the thermal history. Elastic properties of nonpolar polymer matrices reinforced with GB were taken from literature [129-131] for further validation purposes. Aforementioned injection molded PBT GB composites type 1A were also used to investigate the creep behavior.

The PBT GF compounds were processed by the two components injection molding machine Ferromatik Milacron FM F 110 S/2F to plates having length 80 mm, width 80 mm and thickness 2.5 mm, Fig. 32 (left). Three test bars of each plate were taken out both parallel and perpendicular to the flow direction. The test bar geometry is shown in Fig. 32 (right). The plates were manufactured using

conventional injection molding (CIM) and push pull processing (PPP) [132] to introduce different cross-sectional fiber orientation distributions.

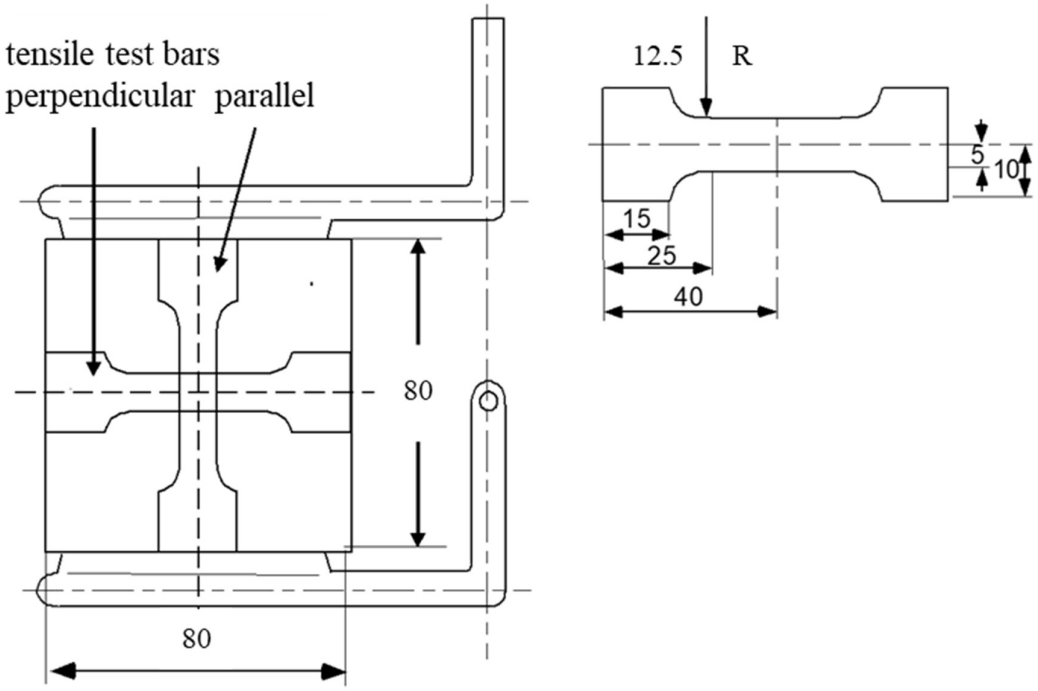

Fig. 32 Geometry of injection molded rectangular plates having dimensions 80 x 80 x 2.5 mm³ (left) and the tensile test bars (right) [132].

The methods to determine characteristic properties of composites are listed in Table 9.

Table 9 Measuring methods, determined quantities, instruments and standards.

method	measured quantity	instrument	standard
digital microscopy	morphology	VHX7000, Keyence (Osaka, Japan)	no standard
DSC	crystallinity	DSC 214 Polyma, Netzsch (Selb, Germany)	EN ISO 11357-9
TGA	filler content w_F	TG 209 F1 Libra, Netzsch (Selb, Germany)	no standard
TGA/STDA	fiber length distribution (FLD)	TGA/STDA 851, Mettler Toledo (Columbus, USA)	no standard
IET	flexural modulus E_f longitudinal modulus E_l shear modulus G_t Poisson´s ratio μ	GrindoSonic MK7 (Leuven, Belgium)	ASTM E1876-22

FEA	stress distribution eigenfrequency f	SIMULIA/ABAQUS2020 ANSYS Workbench 2022R2	no standard
DMA	storage flexural modulus E'_f	DMA 242 E Artemis, Netzsch 3-point bending mode (Selb, Germany)	EN ISO 6721-1
tensile test	Young´s modulus E Poisson´s ratio μ	Zwick Z010, Zwick/Roell (Ulm, Germany)	DIN EN ISO 527-1
oscillatory torsion	storage shear modulus G'	AR 1000, TA Instruments (New Castle, USA)	no standard
creep test	creep compliance J (t)	Zwick 1411 / Zwick 4211 Zwick/Roell (Ulm, Germany)	ISO 899-1
SEM	filler matrix adhesion	JSM-IT100, Jeol (Tokyo, Japan)	no standard

Digital microscopy

Morphological investigations were performed to evaluate processing-induced inhomogeneities that may cause anisotropic elastic behavior. Cross-sectional variations of crystallinities or GB concentrations were investigated under polarized light using a digital microscope, both in transmitted light and reflected light microscopy. Thin sections (thickness $t = 15$ µm) were cut from the specimens after annealing using a microtome (Leica RM2165, Leica Biosystems, Nussloch, Germany), were embedded in Canada balsam under a cover glass on a microscope slide and investigated under polarized light using a digital transmitted light microscope to map entire cross-sections. Polished cross-sections of PA66 GB and PBT GB composites embedded in cold-curing epoxy resin were prepared for reflected light microscopy.

Differential scanning calorimetry (DSC)

The degree of crystallinity X_C was determined by DSC traces ranging from 30 – 300 °C and 25 – 260 °C for PMC of PA66 and PBT, respectively. The heating rate was 10 K/min under nitrogen atmosphere (20 ml/min). As the filler does not contribute to the heat of fusion of the matrix the mass has to be corrected in DSC measurements correspondingly to the filler content. Thus, X_C was evaluated using Eq. (43):

$$X_C = \frac{\Delta h_m + \Delta h_{pc}}{(1 - w_F)\Delta h_m^0} \tag{43}$$

with measured heat of fusion Δh_{m}, heat of fusion of a 100 % crystalline polymer $\Delta h_{\mathrm{m}}^{0}$ taken from [133, 134], post-crystallization enthalpy Δh_{pc}, and filler weight content w_{F}.

Thermogravimetric analysis (TGA), fiber length and fiber orientation distribution (FLD, FOD)

Filler contents of PA66 GB and PBT GB test bars as well as the fiber content of PBT GF plates were determined by TGA measurements from 20 °C to 950 °C with a heating rate of 20 K/min to pyrolize the matrix. To determine the length distributions, the remaining glass fibers were separated from each other and the lengths of a few 100 fibers were measured by image.

The cross-sectional fiber orientations were evaluated using the section method to determine inclination angles θ and plane angles ϕ. These angles allow for calculating the spatial orientation of the fibers. Averaging over the sample cross-section provides the mean orientation factors f_1, f_2 and f_3, Fig. 33.

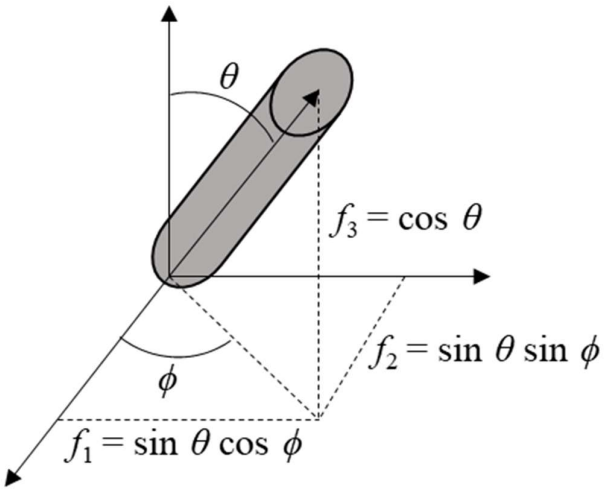

Fig. 33 Orientation factors f_1, f_2, and f_3 of a single fiber with inclination angle θ and phase angle ϕ.

Impulse excitation technique (IET)

Two sets of dumbbell specimens were cut into rectangular bars with dimension of (60x10x4) mm (set 1) and (80x10x4) mm (set 2) for IET measurements to identify geometry effects, as ASTM E1876-22 recommends a length-thickness-ratio of at least 20. Only the 60 mm specimens with a length-thickness ratio of 15 were suitable to the DMA 3-point bending sample holder. Thus, subsequent to IET measurements, the specimens were tested by DMA to directly compare both methods. Five test bars of each grade were tested ten times for the excitation modes flexural, longitudinal and torsional. After that Poisson´s ratio μ was determined iteratively starting with a Poisson´s ratio taken from literature until the absolute deviation remains smaller than 0.02, as required by ASTM E 1876-22.

Finite element analysis (FEA)

Determination of stress distribution: To address maximum stresses of an elementary volume (EV), FEA using the software SIMULIA/ABAQUS2020 was performed in 2D for the middle plane of the EV. The EV holds for a single spherical inclusion embedded in matrix where the diameter of the sphere is representative for the filler volume content v_F. The EV´s are arranged either in a cubic or a hexagonal lattice with maximum achievable filler content of $v_{F,max} = \mu/6 \approx 0.52$ and $v_{F,max} = \mu/27 \approx 0.60$, respectively. A mixed mesh of triangle (S3) and rectangle (S4) shell elements with linear shape functions was used having total number of elements = 53,000 for each arrangement. The top and bottom nodes were coupled in *y*- and *z*-directions with a reference node using a kinematic coupling constraint. For the reference node at the bottom all rotational and translational degrees of freedom were fixed to $u1 = u2 = \ldots.. = u6 = 0$. For the reference node at the top, all degrees of freedom except for the translation in *y*-direction were fixed as well. The displacement in the positive *y*-direction ($u2$) was defined at the top node to apply a uniaxial tensile load. Static linear analysis was carried out by implementing the materials properties of matrix modulus E_M and filler modulus E_F, filler Poisson´s ratio μ_F and matrix Poisson´s ratio μ_M, as well as the filler volume content v_F.

Determination of eigenfrequency *f*: A finite element model was built as an additional evaluation routine for impulse excitation experiments. Therefore, a 3D analysis approach for determining the flexural, longitudinal, and torsional resonant frequencies was introduced to the FEA software ANSYS Workbench 2022R2. The rectangular specimens were uniformly meshed using quadratic shell elements with dimensions of 0.5 mm. As the elastic material parameters were unknown, an inverse parameter optimization approach was applied to determine the elastic parameters *E* and μ using the integrated direct optimization tool of ANSYS Workbench. The iterative parameter optimizer varied both elastic modulus and Poisson's ratio to achieve resonant frequencies approaching those of the IET. Because the flexural and longitudinal modes are influenced by both *E* and μ, a multi-criteria objective function based on the torsional and flexural resonant frequencies or torsional and longitudinal resonant frequencies, respectively, was used.

Dynamic mechanical analysis (DMA)

DMA 242 E Artemis in 3-point bending mode (support distance 50 mm) was used after instrument calibration in accordance to the manufacturer´s procedure to perform strain sweeps with strain amplitude of 20, 50, 80, 110, 150, 200, and 240 µm at a frequency of 1 Hz. The maximum dynamic force was 10.9 N with a proportionality factor of 1.1. Each sample was measured for 5 min at each strain amplitude at 23 °C to determine the storage modulus.

Tensile test (TT)

Tensile tests were performed at 23 °C using a universal testing machine equipped with a 10 kN load cell (resolution: 0.12 %) and a laser extensometer (Zwick/Roell laserXtens extensometer 2-220 HP; resolution: 0.1 µm) at initial clamping length of 80 mm. To address the simultaneous determination of the time-dependent change in length and width their initial values of the laser were set to 22 mm and 9 mm, respectively. Cyclic deformation steered tensile tests were performed in the linear elastic region between 100 N and 1000 N at a displacement rate of 1 mm/min. Four test bars of each PMC were subjected to six cycles. The slopes of the last five cycles provided Young´s modulus and Poisson's ratio for both loading and unloading cycles.

Oscillatory torsion (OT)

The rheometer AR 1000 used for oscillatory torsion measurements was equipped with a clamping device for the rectangular specimen to determine storage shear modulus G'. The initial clamping length was 45 mm. Three test bars (parallel region of dumbbell specimen with $l = 60$ mm) of each PMC were measured at 1 Hz in controlled-stress mode with a maximum torque of 5 mN*m at 23 °C.

Creep testing

For PBT GB composites creep tests were carried out on a Zwick 1411 creep stand equipped with optical strain measurements at 23 °C and 50 % r.h. The initial stresses σ_0 were chosen to be 11, 17, and 22 MPa, respectively, for neat PBT. This corresponds roughly to yield strength ratios of 20, 30, and 40 %. Initial stresses σ_0 were chosen to be 17 and 22 MPa for PBT GB 20 and 11 and 22 MPa for PBT GB 30. Creep strains were measured for maximum of 1000 h.

For PBT GF composites creep tests were performed for 336 h (2 weeks) at 23 °C and 50 % r.h. in the creep stand Zwick 4211 with fully automatized data acquisition. The initial stresses σ_0 were chosen to be 12.5, 25, and 37.5 MPa corresponding to 25, 50, and 75 %, respectively, of the yield stress σ_y of neat PBT. Subsequently, the creep strain curves were corrected for errors in the measured initial length due to non-vertical mounting and sliding in clamps using a method proposed in [135].

Scanning electron microscopy (SEM)

Fracture surfaces of GB and GF composites were sputtered with gold (90 s, 20 mA, 0,1 mbar) and investigated by SEM. For GB composites a JEOL JSM-IT100 equipped with a tungsten cathode was used to study the fracture characteristics at 5.0 kV under vacuum conditions. For GF composites the scanning electron microscope JEOL JSM 6300 F, using an accelerating voltage of 10 kV provided qualitative information about the filler matrix adhesion and the deformation mechanisms parallel and perpendicular to the flow direction of both CIM and PPP test bars.

4 Results and discussion of the results

4.1 Structure-property-relationship of GB composites

During processing shear and elongational flows influence the structure of polymers and composites [24, 25]. Amorphous regions are subjected to internal stresses due to different orientations of macromolecules in the skin and core region. Crystalline regions exhibit varying thicknesses of crystal lamellae as cross-section dependent cooling rates affect the nucleation rate. Additionally, plate-like fillers and fibers are oriented parallel to the flow direction in the skin regions due to shear flows whereas elongational flows in the core region orient them perpendicular to the flow direction. This leads to processing dependent skin core structures also affecting the mechanical properties of PMC.

4.1.1 Morphological and thermo-physical investigations of GB composites

Morphology

The morphologies of neat semi-crystalline PA66 and PBT exhibit processing-induced cross-sectional variations of the spherulitic structures that may cause anisotropic elastic behavior, Fig. 34. The thickness of the skin layer is in the order of 200 µm for both polymer matrices. The smaller spherulites of PBT can be attributed to higher crystallization rates [136, 137]. Because the skin layers solidify faster due to the rapid temperature decrease, the crystallinity remains lower than in the core. This leads to a cross-sectional dependent distribution of internal stresses and more shrinkage in the core. As the strain state of the test bars is fixed, compression stresses in the skin layers and tensile stresses in the core region occur. To overcome these processing dependent influences on morphology and the mechanical properties [138] all test bars were annealed at 180°C prior to mechanical and thermal testing to establish a defined and uniform thermal history.

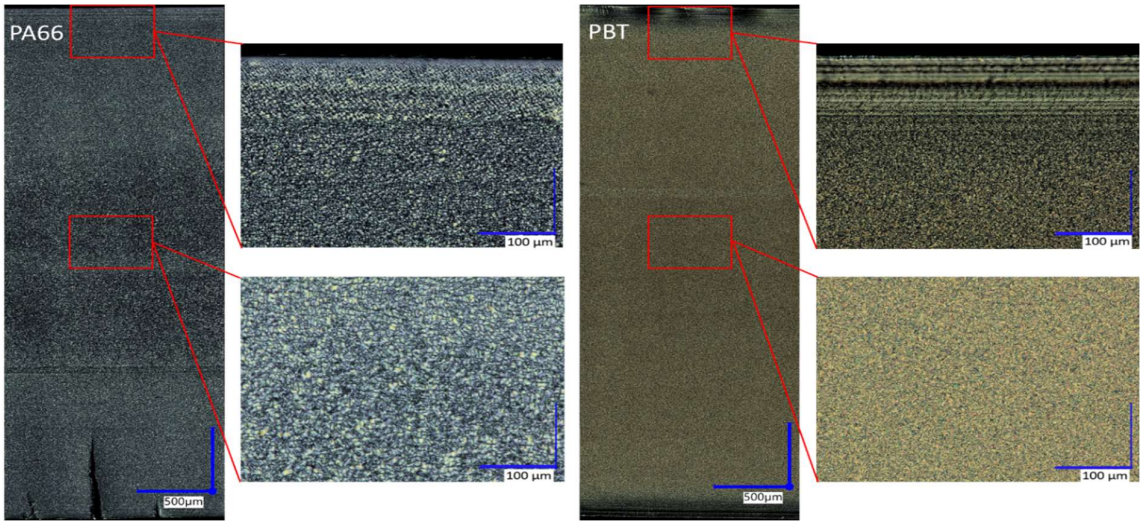

Fig. 34 Skin core morphology of annealed PA66 (left) and PBT (right) along the cross-section; flow direction ↔.

The cross-sectional distribution of GB of both PMC exhibit rather homogeneous GB concentrations over the cross-section, only the outer skin of about 200 µm shows slightly lower GB concentrations, Fig. 35. Concentration differences of GB between skin and core were determined to 5 % for PA66 GB30, 7 % for PA66 GB40, 6 % for PBT GB20, and 3 % for PBT GB30. If matrix moduli and filler matrix adhesion were identical in skin and core, an overall reduced GB content decreases the moduli by approximately 300 MPa for PA66 GB30, 400 MPa for PA66 GB40, 300 MPa for PBT GB20, and 200 MPa for PBT GB30 [139].

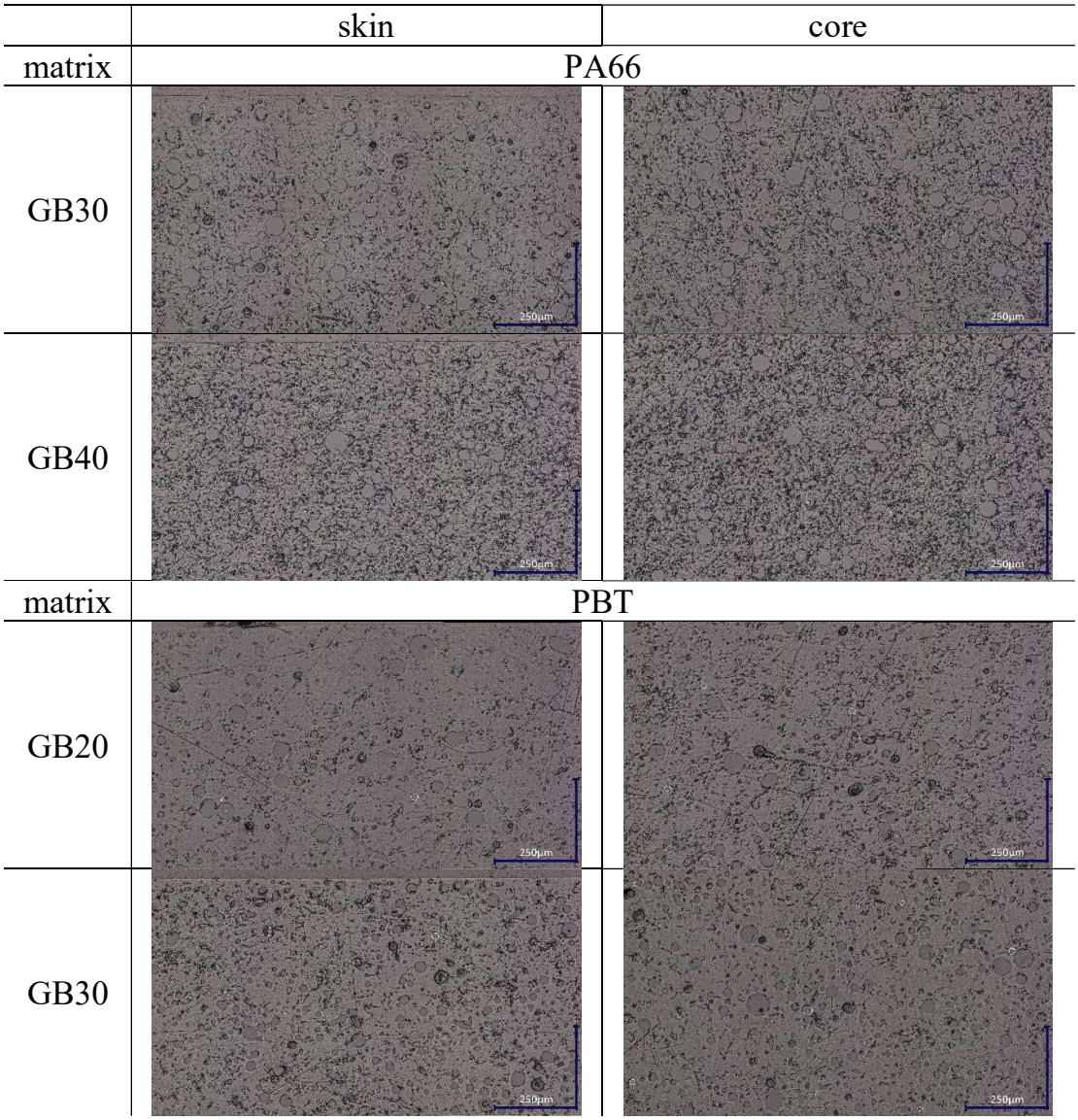

Fig. 35 Cross-sectional GB distributions of PA66 and PBT composites.

Differential scanning calorimetry

Samples of approximately 10 mg were taken out from both skin and core regions of the PMC and investigated with respect to characteristic temperatures, enthalpies and crystallinities, Table 10. The annealing affects the heats of fusion and hence the crystallinities whereas post-crystallization enthalpies and melting temperatures exhibit minor changes. For PA66 composites, crystallinities in the skin region increase from 25 % to 30 %, in the core region from 28 % to 32 %. For PBT composites, the skin region exhibits an increase from 29 % to 33 %, in the core region from 34 % to 37 %.

Table 10 Crystallization and melting behavior of neat PA66 and PBT and their GB composites.

parameter			polymer matrix composite					
			PA66			PBT		
			w_F [%]			w_F [%]		
			0	30	40	0	20	30
$T_{pc}^{initial}$	°C	skin	241	242	240	203	210	210
		core	248	-	245	207	-	-
$\Delta h_{pc}^{initial}$	J/g	skin	-2.1	-1.1	-2.0	-2.7	-0.6	-0.3
		core	-1.4	-	-1.0	-3.8	-	-
$T_M^{initial}$	°C	skin	265	265	264	226	226	226
		core	266	265	265	226	227	227
$\Delta h_M^{initial}$	J/g	skin	65.2	45.4	40.4	47.3	35.4	28.9
		core	71.5	50.7	42.8	48.7	36.8	32.1
$X_C^{initial}$	%	skin	24.8	24.8	25.1	32.9	31.0	29.2
		core	27.5	28.4	27.3	31.1	32.9	32.8
T_{peak}^{anneal}	°C	skin	204	212	210	194	199	203
		core	212	217	213	196	202	204
T_{pc}^{anneal}	°C	skin	243	244	242	206	213	-
		core	-	-	247	210	-	-
Δh_{pc}^{anneal}	J/g	skin	-0.5	-0.2	-1.6	-1.4	-0.7	-
		core	-	-	-1.0	-1.8	-	-
T_M^{anneal}	°C	skin	265	265	264	226	225	228
		core	266	266	265	228	227	228
Δh_M^{anneal}	J/g	skin	76.2	55.3	46.2	52.5	40.5	33.7
		core	82.6	58.0	48.4	53.5	41.9	36.2
X_C^{anneal}	%	skin	29.7	30.9	29.1	37.2	35.5	34.3
		core	32.4	32.5	31.0	36.2	37.4	36.9

*with annealing peak temperature T_{peak}^{anneal}, post-crystallization temperature T_{pc}, melting temperature T_M, enthalpies of post-crystallization Δh_{pc} and melting Δh_M, and degree of crystallinity X_C, for both initial and annealed state

DSC investigations showed that the crystallinities increase due to annealing but the differences between skin and core remain after annealing. Thus, it can be concluded that the stiffnesses of both PMC increase.

4.1.2 Elastic properties of GB composites – methods comparison

Standardized methods such as TT, DMA, and OT are often time-consuming and destructible. The vast development of new bio-based polymers and recyclates with yet unknown properties necessitates the use of faster analyzing tools. The IET is a fast and non-destructive testing method and thus predestined for PMC. However, as PMC are viscoelastic materials one has to keep in mind that IET uses much smaller deformation amplitudes and larger frequencies compared to DMA leading to higher moduli for IET than for DMA and TT. Furthermore, it is necessary to validate measured IET resonant frequencies using FEA to account for geometric deviations that do not comply to those required by ASTM E 1876-22.

Comparison of IET to FEA simulation

The FEA optimization procedure was used to verify the resonant frequencies and the associated elastic constants of non-destructive IET according to ASTM E1876-22 for flexural, longitudinal and torsional vibration mode of both 60 mm and 80 mm long test bars, Table 11.

Table 11 Both experimental arrangements and corresponding FE simulation for IET excitation modes to determine the deformation behavior.

vibration mode	scheme	FE simulation of resonant frequencies
flexural	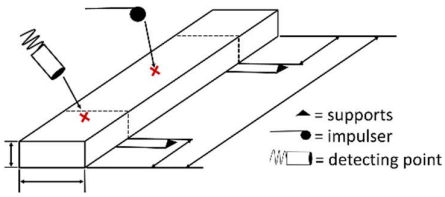	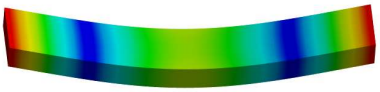
longitudinal	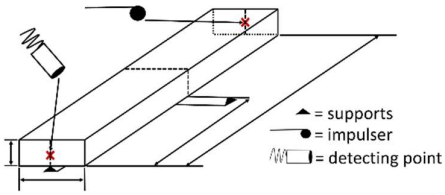	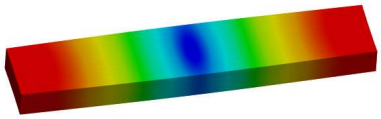
torsional	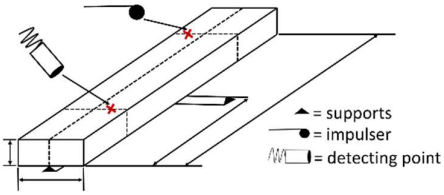	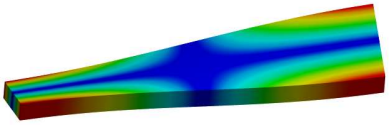

The resonant frequencies determined by measurement and simulation differ less than 1% for each PMC and vibration mode, Table 12. They become higher for shorter samples and higher GB contents. It should be noted that the measured resonant frequencies are denoted with standard deviations (STD), the FEA optimization procedure was performed using mean specimen densities and constant test bar geometries.

Table 12 Resonant frequencies of IET for each material and vibration mode according to ASTM E1876-22 and FEA.

mode	PMC		l = 60 mm resonant frequency			l = 80 mm resonant frequency		
	matrix	w_F	ASTM E1876-22	FEA	diff.	ASTM E1876-22	FEA	diff.
		%	Hz	Hz	%	Hz	Hz	%
flexural	PA66	0	1861 ± 36	1853	0.43	1082 ± 61	1081	0.09
		30	2199 ± 14	2195	0.18	1224 ± 8	1224	0.00
		40	2335 ± 12	2336	0.04	1291 ± 4	1292	0.08
	PBT	0	1670 ± 19	1678	0.48	897 ± 23	895	0.22
		20	1917 ± 28	1916	0.05	1063 ± 4	1063	0.00
		30	2005 ± 11	2005	0.00	1132 ± 6	1132	0.00
longitudinal	PA66	0	14124 ± 131	14072	0.37	10721 ± 30	10716	0.05
		30	16642 ± 56	16502	0.84	12358 ± 42	12314	0.36
		40	17186 ± 48	17153	0.19	12712 ± 19	12712	0.00
	PBT	0	12386 ± 69	12433	0.38	9036 ± 17	8988	0.53
		20	14012 ± 103	13989	0.16	10399 ± 23	10401	0.02
		30	14792 ± 53	14803	0.07	11074 ± 29	11084	0.09
torsional	PA66	0	5328 ± 61	5337	0.17	4048 ± 14	4047	0.02
		30	6270 ± 24	6280	0.16	4651 ± 14	4670	0.41
		40	6631 ± 14	6608	0.35	4901 ± 9	4896	0.10
	PBT	0	4701 ± 28	4703	0.04	3429 ± 45	3434	0.15
		20	5373 ± 41	5378	0.09	3986 ± 9	3977	0.23
		30	5705 ± 20	5694	0.19	4277 ± 11	4257	0.47

The verified resonant frequencies allow for calculating the moduli of each PMC for any given vibration mode and filler content, Table 13. Within the accuracy of measurement, test bars with a length-thickness-ratio of 15 already provide the same stiffnesses like test bars with a length-thickness-ratio of 20. In general, moduli in flexural excitation (E_f^{IET}) are always smaller than moduli in longitudinal excitation (E_l^{IET}). This can be attributed to the process-induced skin core structures with almost amorphous skin regions having slightly lower GB concentrations as skin properties contribute more to E_f^{IET} than to E_l^{IET}. This behavior is more pronounced for PA66 composites due to their lower crystallinity.

Table 13 Comparison of measured (ASTM E1876-22) and simulated (FEA) moduli E_f, E_l, and G_t for PA66 composites and PBT composites for test bar length l = 60 mm and l = 80 mm.

mode	PMC matrix	w_F %	l = 60 mm E^{IET} MPa	E^{FEA} MPa	l = 80 mm E^{IET} MPa	E^{FEA} MPa
flexural	PA66	0	3261 ± 18	3219	3213 ± 37	3214
		30	4950 ± 55	4920	4944 ± 52	4927
		40	5736 ± 42	5723	5673 ± 53	5691
	PBT	0	2795 ± 19	2812	2775 ± 33	2759
		20	3865 ± 25	3839	3712 ± 27	3718
		30	4507 ± 15	4498	4504 ± 25	4483
longitudinal	PA66	0	3386 ± 11	3353	3343 ± 15	3343
		30	5322 ± 23	5362	5293 ± 18	5249
		40	5997 ± 16	5972	5927 ± 23	5928
	PBT	0	2880 ± 10	2900	2855 ± 13	2825
		20	3930 ± 6	3909	3852 ± 11	3859
		30	4682 ± 13	4686	4659 ± 10	4659
Mode	matrix	w_F %	$G_\mathrm{t}^{\mathrm{IET}}$ MPa	$G_\mathrm{t}^{\mathrm{FEA}}$ MPa	$G_\mathrm{t}^{\mathrm{IET}}$ MPa	$G_\mathrm{t}^{\mathrm{FEA}}$ MPa
torsional	PA66	0	1139 ± 12	1145	1132 ± 9	1138
		30	1791 ± 1	1799	1780 ± 15	1798
		40	2113 ± 16	2101	2095 ± 20	2100
	PBT	0	978 ± 5	979	972 ± 7	977
		20	1378 ± 5	1380	1344 ± 8	1346
		30	1640 ± 4	1637	1639 ± 6	1636

* ± represents the standard deviations of five specimens

Comparison of DMA in bending mode to flexural IET

A DMA in 3-point bending mode was used to investigate the flexural properties of the 60 mm specimen used for IET in terms of storage and loss moduli at 23 °C. Strain amplitude sweeps were performed by increasing the strain amplitudes Δx_0 stepwisely from 20 µm to 240 µm. For all PMC the bending storage moduli $E'^{\mathrm{DMA}}_\mathrm{f}$ increased with strain amplitude and reached a maximum modulus asymptoticly if the strain amplitude exceeded 110 µm, Fig. 36 (a) and (b). This behavior did not depend on filler content and originates from changing experimental boundary conditions for small forces e.g. due to friction and sliding of the test bars on the bearing, partial contact of the test bar to the bearing because of a little warpage, and a minor indent of the excitation rod prior to bending. Only for deformation amplitudes exceeding 110 µm the applied force led to a defined contact of test bar and bearing resulting in constant $E'^{\mathrm{DMA}}_\mathrm{f}$ of all PMC. This assumption was also confirmed by the damping behavior tan δ. Constant $E'^{\mathrm{DMA}}_\mathrm{f}$

increases with increasing v_F from neat PA66 to PA66 GB30 and PA66 GB40 by 47 % and 72 %, respectively, from neat PBT to PBT GB20 and PBT GB30 by 33 % and 59 %, respectively.

The comparison of $E'^{\mathrm{DMA}}_{\mathrm{f}}$ determined with strain amplitude 110 µm to $E^{\mathrm{IET}}_{\mathrm{f}}$ shows good correspondence, Fig. 36 (c) and Table 14.

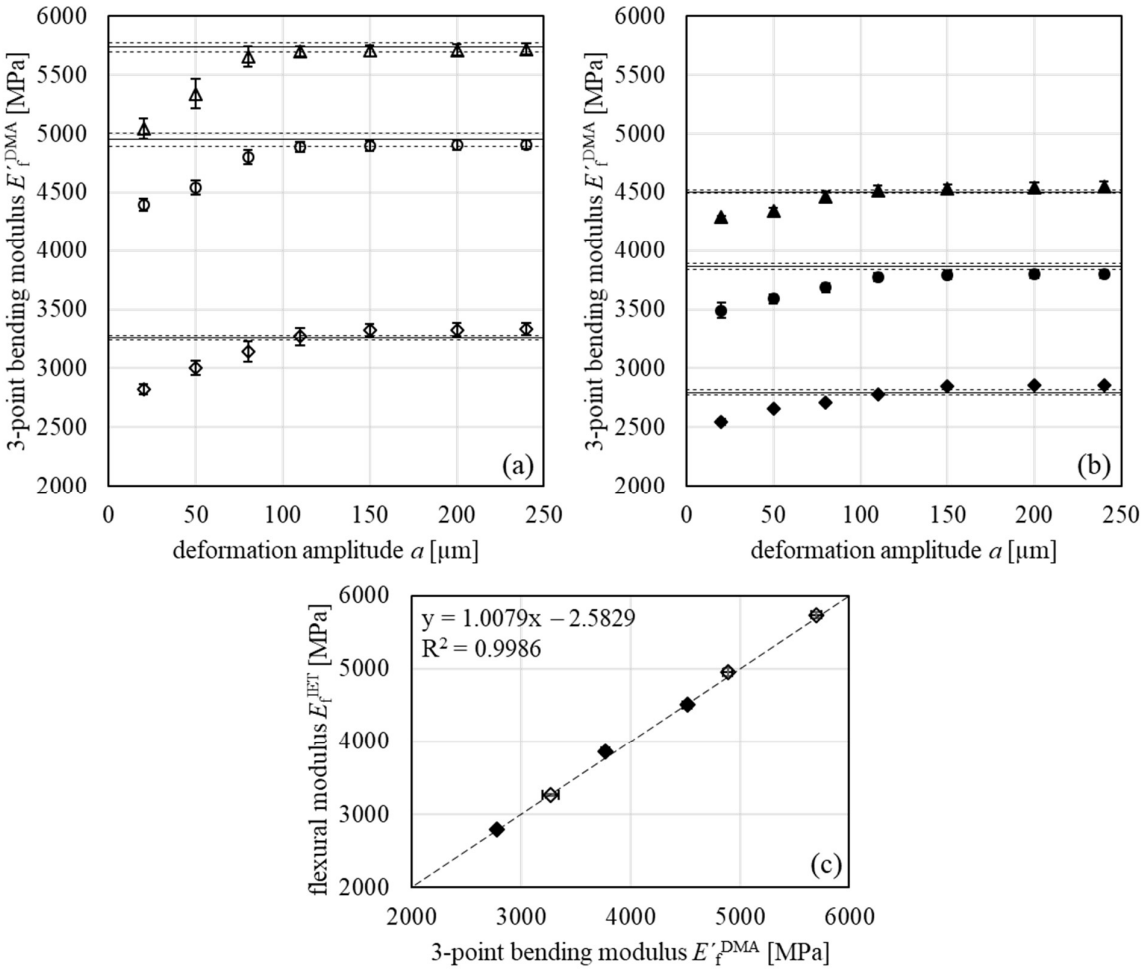

Fig. 36 Deformation amplitude a dependent Young's moduli E'^{DMA}_f in 3-point bending mode (symbols) of PMC with PA66 matrix (a) and PBT matrix (b); the flexural E^{IET}_f (solid lines) with STD (dashed lines) are included for comparison. In (c) symbols (empty = PA66; full = PBT) represent PMC moduli of IET and DMA for a = 110 µm.

Assuming a linear correlation according to Pearson between $E'^{\mathrm{DMA}}_{\mathrm{f}}$ and $E^{\mathrm{IET}}_{\mathrm{f}}$ provided correlation coefficients of significance factor of $r = 1.000$, $p = 0.011$ for PA66 composites and $r = 0.998$, $p = 0.040$ for PBT composites. Both methods yielded identical moduli within the accuracy of measurement although

- the DMA is operated by forced oscillation in contrast to free oscillations for IET,

- the deformation amplitudes of IET were significantly smaller than those of DMA; and
- the frequencies of DMA measurements are three to four orders of magnitude smaller than those of an IET measurement.

Table 14 Pearson correlation and coefficient of variation (CV) of flexural moduli determined by IET and DMA.

matrix	w_F	E'^{DMA}_f / CV	E_f^{IET} / CV	r	p
	%	MPa / %	MPa / %	-	-
PA66	0	3270 ± 75 / 2.29	3261 ± 18 / 0.55		
	30	4890 ± 41 / 0.84	4950 ± 55 / 1.11	1.000	0.011
	40	5700 ± 46 / 0.81	5736 ± 42 / 0.73		
PBT	0	2781 ± 9 / 0.32	2795 ± 19 / 0.68		
	20	3771 ± 35 / 0.93	3865 ± 25 / 0.65	0.998	0.040
	30	4521 ± 40 / 0.88	4507 ± 15 / 0.33		

Comparison of tensile testing to longitudinal IET

Young´s moduli E_l^{TT} were compared to the longitudinal moduli E_l^{IET}, Fig. 37. Stiffnesses of both methods coincide within STD. Furthermore, a larger error susceptibility of TT can be concluded from the determined STD and CV and a slightly higher correlation for specimen length l = 80 mm is revealed by the data correlation according to Pearson, Table 15.

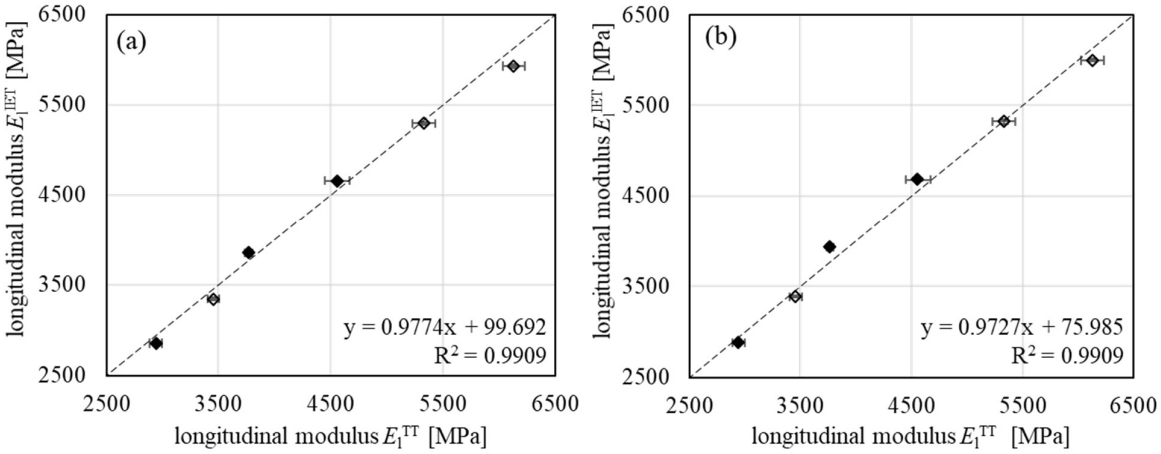

Fig. 37 Correlation between E_l^{TT} and E_l^{IET} for PMC of PA66 (empty symbols) and PBT (full symbols) for sample length l = 60 mm (a) and l = 80 mm (b).

Table 15 Pearson correlation and coefficient of variation (CV) of longitudinal moduli determined by IET and tensile testing.

matrix	w_F	E_l^{TT} / CV unloading	E_l^{IET} / CV l = 60 mm	E_l^{IET} / CV l = 80 mm	r 60 mm / 80 mm	p 60 mm / 80 mm
	%	MPa / %	MPa / %	MPa / %	-	-
PA66	0	3457 ± 53 / 1.53	3386 ± 11 / 0.32	3343 ± 15 / 0.45		
	30	5332 ± 102 / 1.91	5322 ± 23 / 0.43	5293 ± 18 / 0.34	0.999 / 0.998	0.028 / 0.037
	40	6131 ± 100 / 1.63	5997 ± 16 / 0.27	5927 ± 23 / 0.43		
PBT	0	2942 ± 57 / 1.94	2880 ± 10 / 0.35	2855 ± 13 / 0.46		
	20	3769 ± 31 / 0.82	3930 ± 6 / 0.15	3852 ± 11 / 0.29	0.997 / 0.999	0.053 / 0.030
	30	4559 ± 112 / 2.46	4682 ± 13 / 0.28	4659 ± 10 / 0.21		

Comparison of oscillatory torsion to torsional IET

OT loading of rectangular test bars yielded storage shear moduli G'^{OT}_t comparable to torsional moduli G_t^{IET}. Again, shear moduli increase with increasing v_F for both composites systems, Fig. 38.

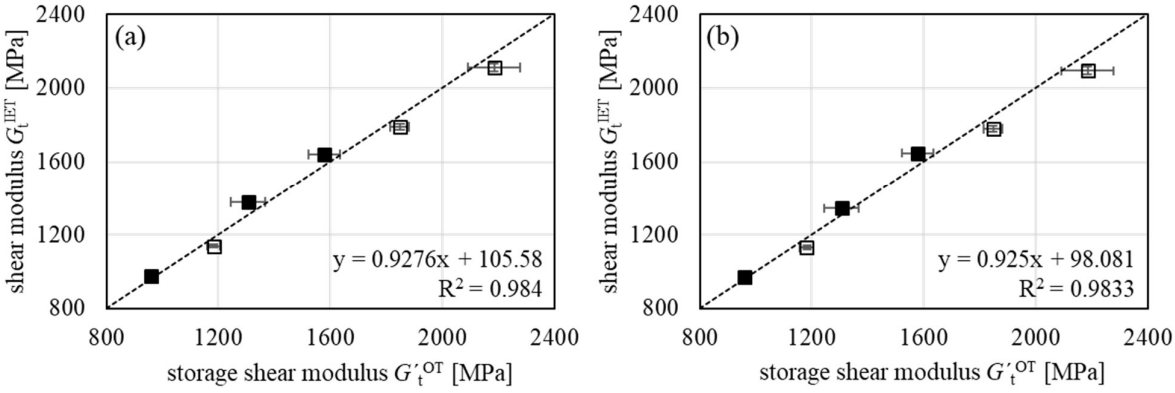

Fig. 38 Correlation between G'^{OT}_t and G_t^{IET} for PMC of PA66 (empty symbols) and PBT (full symbols) for sample length l = 60 mm (a) and l = 80 mm (b).

The STD of OT data indicate more scatter than the torsional IET data. Furthermore, PA66 composites show 50 MPa larger G'^{OT}_t than for G_t^{IET}, whereas for PBT composites slightly lower G'^{OT}_t were found but coinciding within the STD, Table 16. These findings for PMC of PBT might be explained by the more homogeneous morphology compared to PA66 composites. This can be attributed

to the fact that torsional deformation causes also small tensile stresses that are ignored by the evaluation.

Table 16 Pearson correlation and coefficient of variation (CV) of torsional moduli determined by IET and oscillatory torsion.

matrix	w_F	G'^{OT}_t / CV	G_t^{IET} / CV l = 60 mm	G_t^{IET} / CV l = 80 mm	r 60 mm / 80 mm	p 60 mm / 80 mm
	%	MPa / %	MPa / %	MPa / %	-	-
PA66	0	1183 ± 25 / 2.11	1139 ± 12 / 1.05	1132 ± 9 / 0.80		
	30	1849 ± 33 / 1.78	1791 ± 1 / 0.06	1780 ± 15 / 0.84	1.000 / 1.000	0.004 / 0.006
	40	2185 ± 92 / 4.21	2113 ± 16 / 0.76	2095 ± 20 / 0.95		
PBT	0	960 ± 7 / 0.73	978 ± 5 / 0.51	972 ± 7 / 0.72		
	20	1306 ± 61 / 4.67	1378 ± 5 / 0.36	1344 ± 8 / 0.60	0.999 / 1.000	0.033 / 0.001
	30	1578 ± 57 / 3.61	1640 ± 4 / 0.24	1639 ± 6 / 0.37		

Poisson´s ratio μ determined by impulse excitation technique and tensile testing

According to ASTM E1876-22, Poisson´s ratios μ^{IET} of isotropic materials can be determined using an iterative approach considering both torsional and flexural moduli. The Poisson's ratio μ^{TT} is determined by measuring both change in length and width simultaneously. Due to the smaller Poisson´s ratio of glass ranging between 0.18 and 0.3 compared to semi-crystalline thermoplastics ranging from 0.4 to 0.45 [13], Poisson´s ratios of both PMC decrease with increasing filler content, Fig. 39.

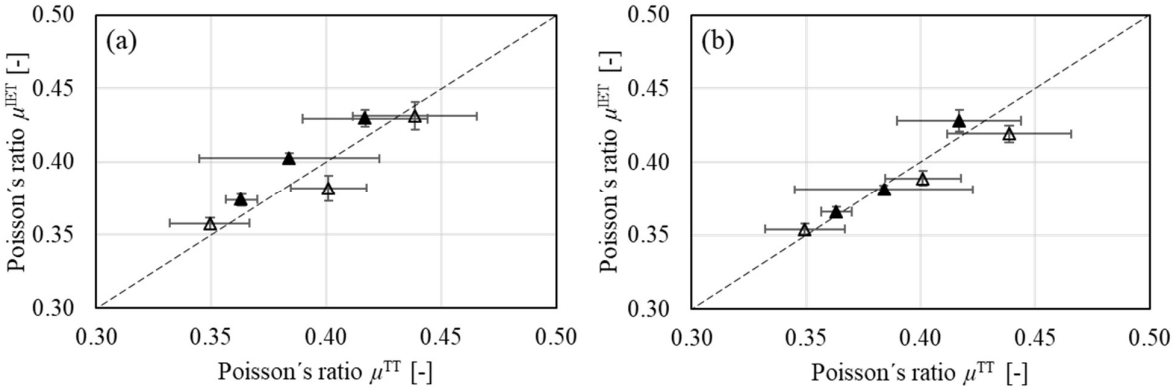

Fig. 39 Correlation between μ^{TT} and μ^{IET} for PMC of PA66 (empty symbols) and PBT (full symbols) for sample length l = 60 mm (a) and l = 80 mm (b).

Both methods yield Poisson´s ratios coinciding within STD and are comparable to those of literature. However, μ^{TT} shows two to three times larger STD than μ^{IET}. This is also reflected by the Pearson correlation where the significance factor p is only reached for 80 mm long PA66 composites, Table 17. The higher STD of μ^{TT} can be explained by insufficient reflection of the extensometer laser light of the polymers.

Table 17 Pearson correlation of Poisson´s ratios μ^{IET} and μ^{TT}.

Matrix	w_F	μ^{TT}	μ^{IET} l = 60 mm	μ^{IET} l = 80 mm	r 60 mm / 80 mm	p 60 mm / 80 mm
	%	-	-	-	-	-
PA66	0	0.44 ± 0.03	0.43 ± 0.01	0.42 ± 0.01	0.959 / 0.999	0.182 / 0.033
	30	0.40 ± 0.02	0.38 ± 0.01	0.39 ± 0.01		
	40	0.35 ± 0.02	0.36 ± 0.01	0.35 ± 0.01		
PBT	0	0.42 ± 0.03	0.43 ± 0.01	0.43 ± 0.01	0.990 / 0.988	0.091 / 0.099
	20	0.38 ± 0.04	0.40 ± 0.01	0.38 ± 0.01		
	30	0.36 ± 0.01	0.37 ± 0.01	0.37 ± 0.01		

4.2 Stiffness modeling of PMC considering interfacial adhesion

Stiffness modeling usually ignores the issue of interfacial adhesion. Today PMC are manufactured not only using commodity matrix and filler systems but also introducing new bio-based matrices, fillers or recyclates with unknown properties due to sustainability reasons. This in turn necessitates easy-to-use modeling approaches. Therefore, one part of this PhD thesis focuses on the development of a modeling approach with access to interfacial adhesion effects.

4.2.1 Theoretical elastic considerations – Elementary volume concept

The elementary volume concept (EVC) is based on geometrical assumptions of Paul and Ishai-Cohen, where the elastic properties of filler composites are

determined by appropriate segmentations in matrix part and composites part. For homogeneously dispersed spherical filler particles with aspect ratio ≈ 1, one can define an elementary volume (EV) consisting of a single particle *F* with diameter *D* embedded in a matrix cube *M* of length *D* + *a* that represents the entire composite, Fig. 40 (a). To ease calculations, the EV of any filler geometry can be converted into a *cube in cube* consideration. Therefore, the inclusion of diameter *D* is transformed to a cube of length *k D* with the efficiency factor *k* taking into account the shape of dispersed phase. Then filler content dependent moduli of composites can be determined by considering macroscopic and microscopic strains and stresses of the EV. Splitting the EV in a matrix part and composites part either *in series* or *parallel* manner with respect to the loading direction lead to microscopic strains ε_M and ε_C, respectively, and the overall strain ε_{EV}, Fig. 40 (b-c).

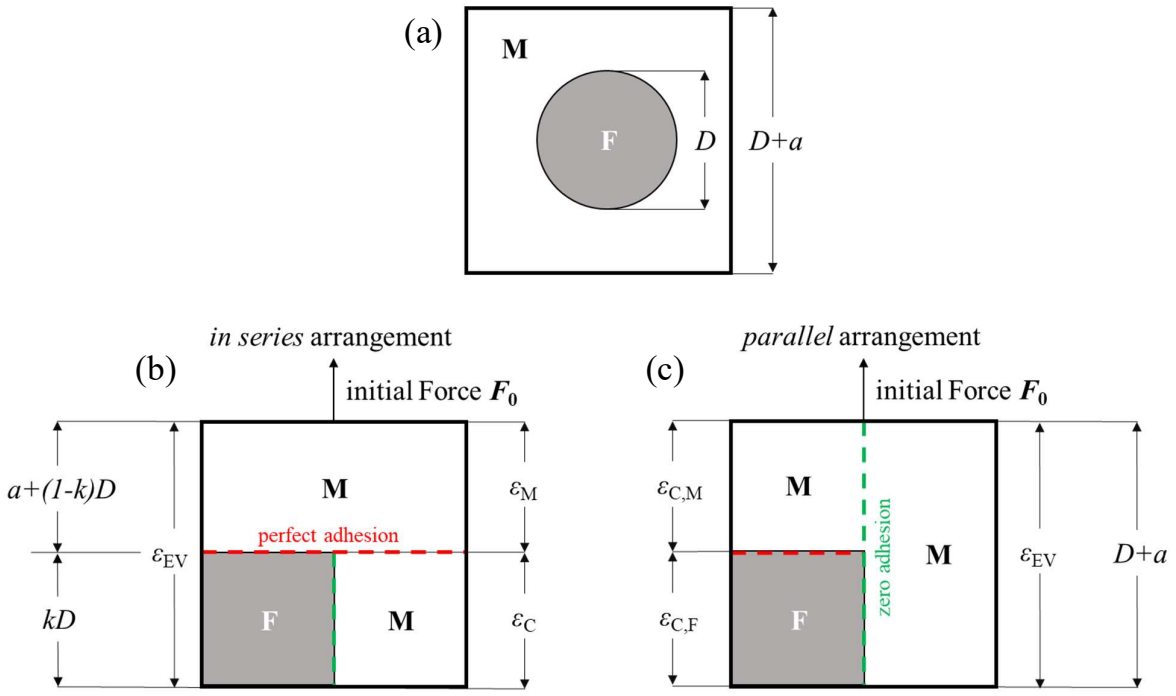

Fig. 40 Elementary volume consisting of a spherical inclusion with diameter D embedded in cubic matrix M having length D + a (top) and transformed cube in cube approach with efficiency factor k in in series and parallel arrangement.

The efficiency factor *k* of spherical inclusions is determined by

$$V_{\text{sphere}} = \frac{\pi}{6} D^3 = k^3 D^3 = V_{\text{cube}} \Rightarrow \quad k = k_{\text{sphere}} = \sqrt[3]{\frac{\pi}{6}} \cong 0.81 \qquad (44)$$

with volume of spherical inclusion V_{sphere} and volume of cube V_{cube}. Thus, the modulus of the EV depends on the filler geometry, the arrangements of matrix part and composites part and how the adhesion acts between filler and matrix.

Depending on the segmentation approach, it is necessary to make assumptions regarding the adhesion between matrix and filler. In the *in series* arrangement, "perfect" adhesion is assumed over the entire cross-section $(D + a)^2$ perpendicular to the load direction between matrix part and composites part, and "zero" adhesion between filler and matrix of the composites part in load direction. In the *parallel* arrangement, "zero" adhesion occurs in load direction over the entire cross-section, and "perfect" adhesion is assumed in the composite part over the filler cross-section $(k\,D)^2$.

In order to determine macroscopic stiffness of the composites in terms of filler volume content v_F, matrix modulus E_M and filler modulus E_F, strains and stresses of EV, matrix part and composite part are considered for purely elastic behavior of each constituent phase, **appendix A**. Furthermore, interfacial adhesion effects can be introduced by a dimensionless adhesion coefficient k_{adh} that ranges from "0" (no adhesion) to "1" (perfect adhesion). The physical meaning of k_{adh} is that it scales the effective contact area of stress transfer between filler and matrix to account for reduced adhesion. Therefore, it is introduced quadratically as it is a measure for the reduction of the edge length of the filler cube.

These considerations yield for the *in series* arrangement

$$E_{EV} = E_M \left(1 + \frac{v_F \frac{k_{adh}^2 E_F - E_M}{E_M}}{1 + v_F^{2/3} \frac{k_{adh}^2 E_F - E_M}{E_M} - v_F \frac{k_{adh}^2 E_F - E_M}{E_M}} \right) \tag{45}$$

becoming identical to Paul´s relation for $k_{adh} = 1$, and for the *parallel* arrangement

$$E_{EV} = E_M \left(1 + \frac{v_F \frac{k_{adh}^2 E_F - E_M}{E_M}}{\frac{k_{adh}^2 E_F}{E_M} - v_F^{1/3} \frac{k_{adh}^2 E_F - E_M}{E_M}} \right) \tag{46}$$

becoming identical to Ishai-Cohen´s relation for $k_{adh} = 1$.

The effects of the adhesion factor are shown for the v_F-dependent relative moduli $E_R = E_C/E_M$ in Fig. 41 for both arrangements with $E_M = 3200$ MPa and $E_F = 63000$ MPa. One can see that stiffening only occurs if $k_{adh} > \sqrt{E_M/E_F}$.

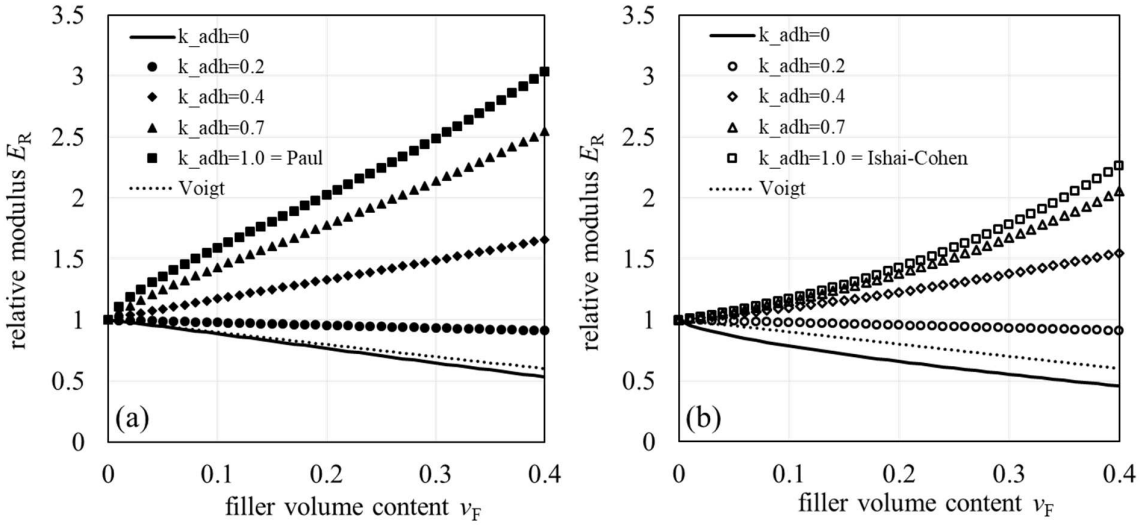

Fig. 41 Relative modulus E_R plotted against the filler volume content v_F for different adhesion coefficients k_{adh} with E_M = 3200 MPa and E_F = 63000 MPa for (a) in series arrangement and (b) parallel arrangement. The dotted lines represent foams with spherical voids according to Voigt.

The *in series* arrangement provide larger moduli than the *parallel* arrangement, and Paul's relation represents the upper bound. As k_{adh} only reduces the contribution of the filler and thus, the moduli, only Eq. (45) is used to elucidate adhesion factors from measured Young´s moduli.

4.2.2 Application: EVC stiffness modeling of PMC with spherical inclusions

Differing to DIN EN ISO 527, the mechanical properties of the PA66 and PBT GB composites, Table 18, were determined by fitting the stress-strain-curves measured at strain rates of 10 %/min using the viscoelastic stress-strain-function (VSSF) [89]

$$\sigma(\varepsilon) \underset{\varepsilon<\varepsilon_{\mathrm{R}}}{\cong} E\varepsilon_{\mathrm{R}}\left(1-e^{-\frac{\varepsilon}{\varepsilon_{\mathrm{R}}}}\right) \tag{47}$$

with Young´s modulus E and relaxation strain ε_{R}. This evaluation avoids effects due to the start of the tensile testing machine. The mechanical properties of non-polar butadiene rubber (BR) [129], low-density polyethylene (PE-LD) [130] and isotactic polypropylene (iPP) [131] reinforced with GB were taken from literature. This widened the range of surface energies of the constituent phases, Table 18, and allowed to refer k_{adh} to it. The tensile properties of all composites reveal a stiffening effect with increasing GB content but only PA66 GB composites show reinforcing behavior indicating a higher filler matrix adhesion.

Table 18 Properties of investigated GB composites.

matrix	w_F %	v_F -	matrix density ρ_M g/cm³	modulus E_{VSSF} MPa	relaxation strain ε_R %	tensile strength σ_{max} MPa	surface energy $\sigma_{surface}$ [116, 117] mJ/m²
PA66	0	0	1.14	3197 ± 28	9.4 ± 0.2	81 ± 0.3	38 to 55
	30	0.16		4955 ± 44	7.8 ± 0.1	91 ± 1.1	
	40	0.23		5452 ± 48	7.2 ± 0.1	86 ± 0.2	
PBT	0	0	1.30	2754 ± 25	9.4 ± 0.1	59 ± 0.1	44 to 49
	20	0.12		3691 ± 33	5.9 ± 0.1	57 ± 0.1	
	30	0.19		4408 ± 39	5.4 ± 0.2	55 ± 0.1	
BR	0	0	0.95	7	6.2		26 to 27
	30	0.15		11	6.3		
	50	0.3		16.8	8		
	65	0.45		48	0.7		
PE-LD	0	0	0.93	98 ± 5	-	8.4 ± 0.2	33 to 35
	20	0.08		124 ± 6	-	7.8 ± 0.5	
	40	0.19		175 ± 27	-	6.2 ± 0.3	
	60	0.35		219 ± 76	-	3.3 ± 0.1	
iPP	0	0	0.91	1070 ± 20	-	31.1 ± 0.5	31 to 42
	20	0.1		1230 ± 10	-	26.0 ± 1.7	
	40	0.2		1280 ± 20	-	18.8 ± 4.9	
	55	0.3		1310 ± 20	-	15.9 ± 1.3	

The interfacial adhesion coefficients k_{adh} were determined using the Excel solver tool and yields calculated moduli of the *in series* E_{EV} that coincide to measured moduli E_{VSSF}. The results were compared to calculated composites moduli E_C according to Ishai-Cohen, Paul and Halpin-Tsai with $\zeta = 2$ for the transversal case, Table 19. It was found that the fitting according to Eq. (45) provides reasonable adhesion coefficients which are well correlated to the surface energies of Table 18. The models of Paul and Ishai-Cohen represent the upper and lower bound solutions, respectively. The Halpin-Tsai approach provides also reasonable E_C but the efficiency factor ζ addresses only geometrical aspects of the filler and is not related to any interfacial adhesion.

As the adhesion coefficient is to range between “1” (perfect adhesion) and “0” (no adhesion) k_{adh} of polar polymer matrices of PA66 and PBT were found to be 0.6 and 0.5, respectively, indicating a slightly higher adhesion of PA66 to GB than PBT. For the non-polar matrix systems BR, PE-LD and iPP smaller k_{adh} ranging from 0.22 to 0.025 were found corresponding to the smaller surface energies. Despite rather low adhesion coefficients all investigated composites exceed the stiffening limit, thus experience stiffening due to incorporated GB, Table 19.

Table 19 Calculated Young´s moduli of various GB composites with evaluated adhesion coefficients and stiffening limits.

matrix	v_F	calculated Young's modulus E_C				adhesion coefficient k_{adh}	stiffening limit $k_{adh,min}^{stiffening}$
		Ishai-Cohen	Paul	Halpin-Tsai	EV ($E_{EV} \equiv E_{VSSF}$)		
	-	MPa				-	-
PA66	0.16	4229 ± 35	5963 ± 44	4770 ± 32	4955 ± 44	0.604 ± 0.017	0.225
	0.23	4899 ± 40	6940 ± 51	5408 ± 36	5452 ± 48	0.570 ± 0.013	
PBT	0.12	3370 ± 30	4744 ± 37	3754 ± 26	3691 ± 33	0.478 ± 0.015	0.209
	0.19	3895 ± 34	5608 ± 43	4449 ± 30	4408 ± 39	0.530 ± 0.013	
BR	0.15	9.2	14.9	10.7	11	0.031	0.011
	0.3	13.3	21.1	16	16.8	0.042	
	0.45	20.4	29.9	24.1	29.9*	n.f.	
PE-LD	0.08	112	173	125	124	0.1	0.039
	0.19	143	232	167	175	0.13	
	0.35	215	331	257	219	0.11	
iPP	0.1	1263	1876	1407	1230	0.22	0.130
	0.2	1565	2414	1824	1280	0.19	
	0.3	1993	3010	2351	1310	0.18	

*to calculate E_{EV} the adhesion factor was set to $k_{adh} = 1$. Note: n.f. means "not fit available".

For BR composites having $v_F = 0.45$ no reasonable k_{adh} were found as for high filler contents not only stiffening due to load transfer occurs. Particle interactions become more likely accompanied by the formation of particle networks with higher stiffnesses [140]. This might be overcome by allowing $k_{adh} > 1$, however, the models of Paul and Ishai-Cohen limit the v_F-dependent stiffening limit s (v_F) to maximum values of 4.3 and 2.9, respectively, not allowing to fit the measured data.

Paul
$$s(v_F) = \frac{E_{EV}}{E_M} = \frac{1}{1 - v_F^{\frac{1}{3}}} \underbrace{\rightarrow}_{v_F=0.45} 4.3 \quad (48)$$

Ishai-Cohen
$$s(v_F) = \frac{E_{EV}}{E_M} = \frac{v_F}{1 - v_F^{\frac{1}{3}}} \underbrace{\rightarrow}_{v_F=0.45} 2.9 \quad (49)$$

This means that the concept fails if particles start to interact with each other at filler contents exceeding 20 %. This behavior was confirmed by the calculated stress distributions for cubic and hexagonal EV arrangements using FEA, Fig. 42. For the cubic arrangement, maximum stresses occur in the matrix between the GB

forming stress lines parallel to the loading direction. The stresses in loading direction increase with filler content and may cause delamination and failure of the interface followed by crack propagation perpendicular to the load direction. For both arrangements the stresses are oriented in load direction, however, the hexagonal arrangement shows a more homogeneous stress pattern depicted as oval “stress islands” around the GB with minimum stresses perpendicular to the load direction. Increasing filler contents lead to the formation of shear stress bands under an angle of 45°, Fig. 42 – hexagonal arrangement with $v_F = 0.40$, reducing the modulus in load direction.

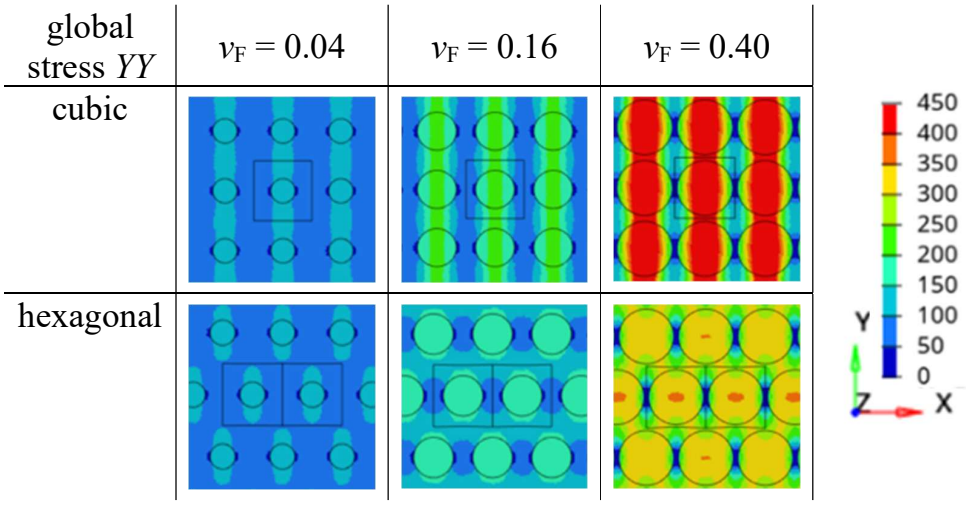

Fig. 42 Tensile stress distributions in loading direction (YY) for cubic and hexagonal EV lattices at varying filler volume contents v_F.

The two considered EV arrangements represent boundaries. Real EV arrangements lie in between. The modulus depends both on the filler volume content and on the chosen arrangement. However, exceeding a certain filler content changes the stress distribution of the two boundary cases in a different manner. The modulus ratio *cubic:hexagonal* deviates more and more from ”1”, Table 20, and the model loses its validity. Furthermore, increasing volume contents ease the crystallization for semi-crystalline polymers due to more induced nucleation leading to higher matrix moduli [141] what also affects the adhesion coefficient.

Table 20 FEA calculated composites moduli E_C of cubic and hexagonal EV arrangements with E_M = 3200 MPa, E_F = 63000 MPa, μ_M = 0.42 and μ_F = 0.22.

v_F	E_C (cubic)	E_C (hexagonal)	ratio cubic : hexagonal
-	MPa	MPa	
0.04	3950	3914	1.01
0.07	4389	4308	1.02
0.16	5988	5656	1.06
0.22	7461	6827	1.09
0.40	14534	11632	1.25

From Fig. 43 it is obvious that the models of Paul and Ishai-Cohen represent upper and lower bounds as they include the measured data as well as the approach according to Halpin-Tsai with $\zeta = 2$. Measured Young´s moduli were well reproduced for Halpin-Tsai and the EVC, but only the latter can also provide quantitative information in terms of k_{adh}.

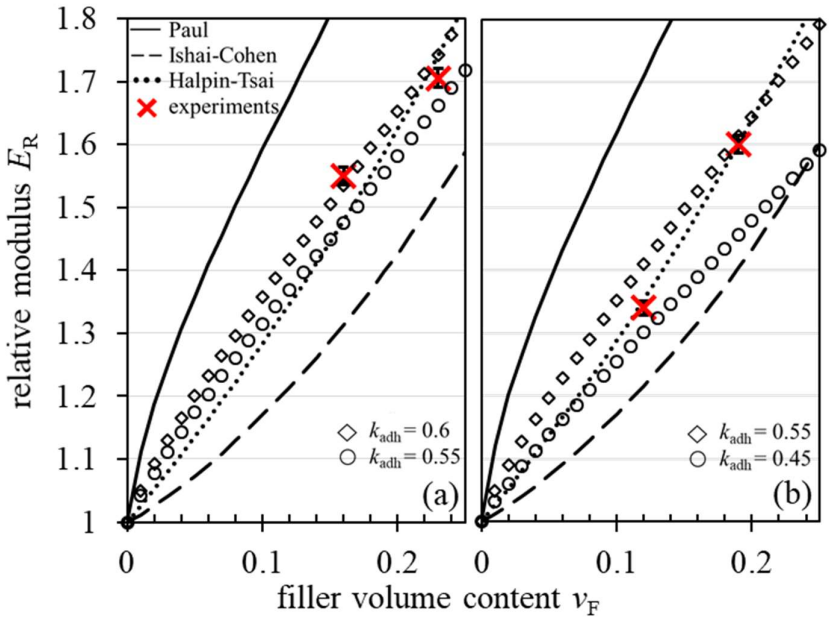

Fig. 43 Relative Young´s moduli calculated according to Paul, Ishai-Cohen, Halpin-Tsai with (ζ = 2) and k_{adh} dependent EVC with experimental ones (x) for (a) PA66, (b) PBT.

To confirm this, fracture surfaces of PA66 and PBT composites were investigated by SEM and they reveal embedded GB only partly covered with matrix material indicating rather mean adhesion, Fig. 44. For PA66 the GB are slightly more covered, Fig. 44 (a) and (b) than for PBT, Fig. 44 (c) and (d) confirming a better adhesion of PA66 and GB. Most fracture surfaces exhibit brittle failure under cryogenic conditions but small fibrils in the vicinity of the GB indicate some ductility which seems to be more pronounced for higher filler contents.

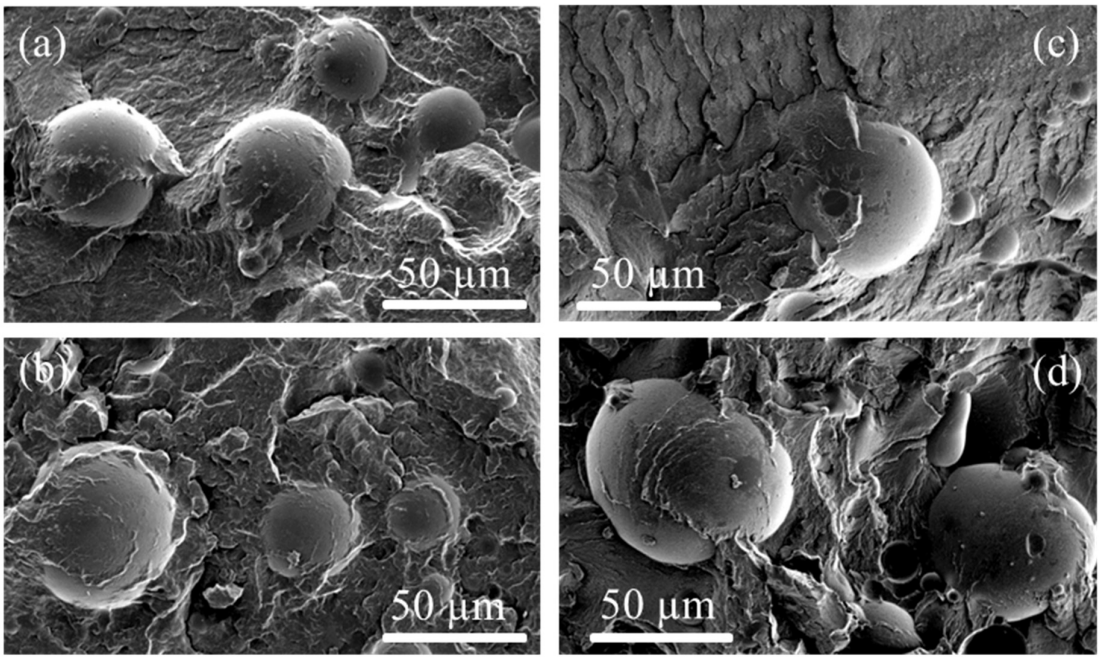

Fig. 44 Fracture surfaces generated under cryogenic condition of (a) PA66 GB30, (b) PA66 GB40, (c) PBT GB20, and (d) PBT GB30.

4.3 Creep modeling of PMC considering interfacial adhesion

Creep of PMC depends on the viscoelastic properties of matrix and filler, filler volume content, interfacial adhesion, preferential filler and fiber orientations as well as experimental parameters such as initial stress and temperature [108]. During creep experiments, time-dependent weakening of filler matrix adhesion reduces the load transfer, thus, increasing matrix stress and creep strain. Consequently, the matrix creep is the crucial quantity for the PMC creep.

Similar to stiffness modeling, interfacial adhesion is hardly considered in literature dealing with creep or creep modeling although it may contribute significantly to the creep behavior of PMC [142-144]. Therefore, this part of the PhD thesis focuses on the introduction of interfacial adhesion to creep modeling.

4.3.1 Theoretical viscoelastic considerations – Creep modeling of PMC with spherical inclusions

The aforementioned approach of a *cube in cube* EV is applied to model creep compliances of PMC containing filler particles with aspect ratio ≈ 1, **appendix A**. The segmentation in a matrix part and a composite part according to Fig. 40 allows for calculating the strains of EV, matrix part, and composites part. The measured creep strain corresponds to the strain of the EV ε_{EV} that is linked to the strains of matrix part ε_M and composites part ε_C via the dimensions of inclusion and EV:

$$\varepsilon_{EV}(\varepsilon_M, \varepsilon_C) = \frac{1-k+d}{1-d}\varepsilon_M + \frac{k}{1-d}\,\varepsilon_C = \left(1 - \frac{k}{1-d}\right)\varepsilon_M + \frac{k}{1-d}\,\varepsilon_C \qquad (50)$$

with geometry factor k and normalized inclusion distance d linked to the filler volume content v_F

$$v_F = \left(\frac{k}{1-d}\right)^3 \tag{51}$$

In creep experiments, a constant initial stress σ_0 is applied to the sample which generates strains of EV, matrix part and composite part in the *in series* EV arrangement. For purely elastic behavior, these strains can be substituted by σ_0, E_{EV}, E_M, and the modulus of the composite part E_C. E_C depends on v_F, E_M and E_F.

strain of EV $$\varepsilon_{EV} = \frac{\sigma_0}{E_{EV}} \tag{52}$$

strain of matrix part $$\varepsilon_M = \frac{\sigma_0}{E_M} \tag{53}$$

strain of composites part $$\varepsilon_C = \frac{\sigma_0}{E_F\left(\frac{k^2}{(1+d)^2}\right)+E_M\left(1-\frac{k^2}{(1+d)^2}\right)} \tag{54}$$

Introducing Eq. (52) – (54) to Eq. (50) yields

$$\frac{\sigma_0}{E_{EV}} = \left(1-\frac{k}{1-d}\right)\frac{\sigma_0}{E_M} + \frac{k}{1-d}\,\frac{\sigma_0}{E_F\left(\frac{k^2}{(1+d)^2}\right)+E_M\left(1-\frac{k^2}{(1+d)^2}\right)} \tag{55}$$

The structure of Eq. (55) allows for introducing an adhesion function $k_{adh}(t)$ having the bounds "0" (no adhesion) and "1" (perfect adhesion). It can account for time dependent changes of the interfacial adhesion. The geometric interpretation is the reduction of the load transferring cross-section. $k_{adh}(t)$ is implemented quadratically representing a measure for the effective edge length of the available cross-section for stress transfer. Eliminating σ_0 in Eq. (55) yields the corresponding compliances.

$$J_{EV}(t,\sigma_0) = \left(1-\frac{k}{1-d}\right)J_M(t,\sigma_0) + \underbrace{\frac{k}{1-d}\,\frac{1}{\boldsymbol{k_{adh}^2(t)}\;E_F\left(\frac{k^2}{(1+d)^2}\right)+E_M\left(1-\frac{k^2}{(1+d)^2}\right)}}_{=constant\ for\ \sigma_0 \ll \sigma_{max}} \tag{56}$$

Substituting k and d with v_F yields

$$J_{EV}(t,\sigma_0) = \frac{1}{E_{EV}(t,\sigma_0)} = \left(1-v_F^{1/3}\right)J_M(t,\sigma_0) + \underbrace{v_F^{1/3}\,\frac{1}{\boldsymbol{k_{adh}^2(t)}\;E_F\,v_F^{2/3}+E_M\left(1-v_F^{2/3}\right)}}_{=constant\ for\ \sigma_0 \ll \sigma_{max}} \tag{57}$$

From Eq. (57) follows that $J_{EV}(t, \sigma_0)$ of PMC is only determined by the matrix creep compliance $J_M(t, \sigma_0)$. The composites part contributes an additional constant strain as long as σ_0 remains small compared to its yield stress σ_{max}. If σ_0 approaches σ_{max} the creep compliance of the composite part becomes also time dependent. Fitting Eq. (57) for different times to measured creep compliance

curves allow for quantifying $k_{adh}(t)$ giving access to changes of the interfacial adhesion.

Application: Creep modeling of PMC with spherical inclusions

The measured creep strains of PBT GB composites were converted to creep compliances and fitted by Burgers model, Eq. (20), and Findley model, Eq. (22). This procedure was performed for time periods up to 250 h and 1000 h using the least square approximation to determine the model parameters and to account for the performance in the corresponding creep regions. Subsequently, the EVC model, Eq. (57), was used to calculate the creep compliances of these composites to extract the time dependent change of interfacial adhesion. After the introduction of the measured matrix creep data, only $k_{adh}(t)$ remains in Eq. (57) as an unknown quantity which can be determined by pointwise fitting.

The measured creep compliances $J(t, \sigma_0)$ of neat PBT and its GB composites exhibit an initial elastic compliance followed by primary and partly starting secondary creep behavior within the measured time range of 1000 h, Fig. 45 (a-c). Only PBT GB30 at $\sigma_0 = 22$ MPa, Fig. 45 (c), clearly exhibits secondary creep with a constant creep rate. The creep compliances increase with initial stress, time, and decreasing filler volume content due to the 20 times stiffer glass beads with negligible creep tendencies for small initial stresses compared to the PBT matrix [145].

Fitting the measured creep compliances using the models of Burgers and Findley provide reasonable fits up to 250 h, especially for small initial stresses. The Findley power law function performs better in both fitting ranges as long as only primary creep occurs, Fig. 45 (a, b). The Burgers model performs better for PBT GB30 at 22 MPa when it comes to secondary creep [146], Fig. 45 (c). The model parameters of Burgers and Findley are summarized in Table 21 and 22, respectively.

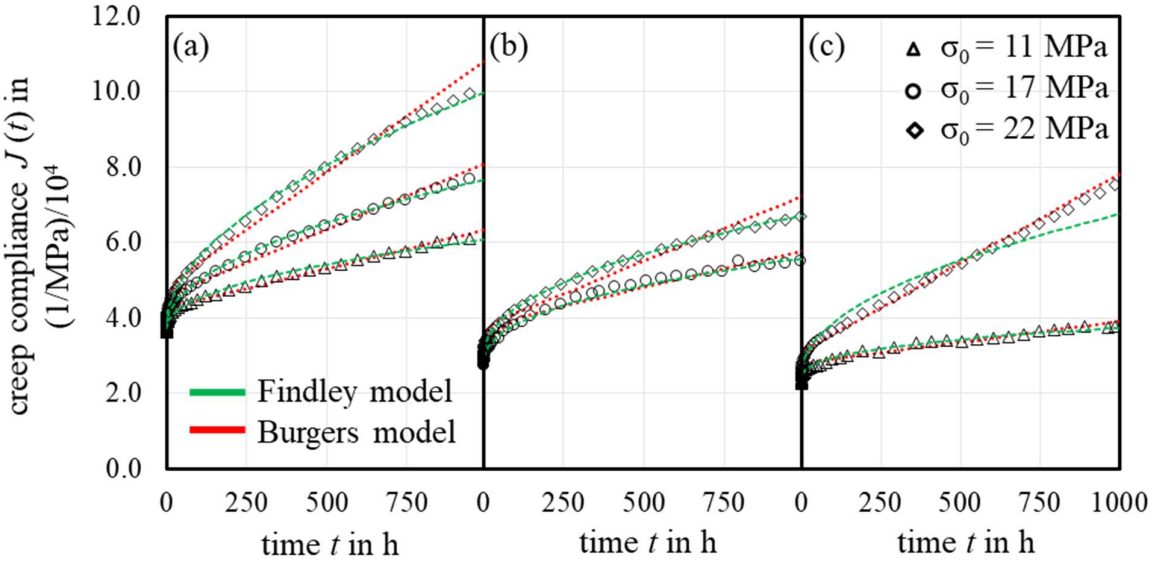

Fig. 45 Measured creep compliances (symbols) of neat PBT (a), PBT GB20 (b), and PBT GB30 (c) with initial stresses σ_0 = 11 MPa (Δ), 17 MPa (o), and 22 MPa (◊) fitted with Findley power law model (green) and Burgers model (red).

The fit parameters of the Burgers model E_1, E_2, η_1, and η_2 decrease with increasing initial stresses (= softening effect due to more free volume) and increase with increasing filler volume content (= stiffening effect due to hard fillers), Table 21. Furthermore, the parameters E_1 and E_2 decrease if the upper time limit is increased from 250 h to 1000 h. This behavior can be attributed to the fitting procedure as the viscous behavior is mainly addressed by dashpot η_1, which contributes more for longer times.

As expected, the parameters E_1 are similar to the moduli of PBT determined by methods of TT or IET. As the first creep strains are measured with a delay of 10 s to 20 s the specimen already experienced some small creep resulting in smaller E_1 compared to other measurement techniques.

Some authors assigned the other model parameters to physical properties, e.g. E_2 is associated with the stiffness of amorphous polymer chains [147] and is to contribute for short term creep. However, the moduli E_2 in Table 21 are too large for amorphous polymers. Similarly, the viscosities η_1 and η_2 are to represent damage of oriented non-crystalline or crystalline regions with characteristic times of damaging processes [148]. Nevertheless, as damage mechanisms in crystalline regions differ from those of amorphous regions with respect to physical processes and characteristic times, it is obvious that all model parameters except E_1 are only fit parameters.

Table 21 Fit parameters of Burgers model according to measured creep compliances at varying initial stresses of neat PBT, PBT GB20, and PBT GB30 showing the effect of chosen fitting time ranges.

range of fitting time	GB content v_F	initial stress σ_0	parameters of Burgers model			
			E_1	E_2	η_1	η_2
h	-	MPa	MPa		GPa h	
0 to 250	0	11	2720	21900	3170	115
		17	2620	21340	1680	92
		22	2570	15900	1090	74
	0.12	17	3540	28100	1750	108
		22	3380	18890	1530	66
	0.19	11	4220	35940	4490	174
		22	4080	18770	1590	47
0 to 1000	0	11	2710	19160	4480	219
		17	2600	14160	2840	141
		22	2560	10684	1660	128
	0.12	17	3500	24100	3310	123
		22	3340	18500	2370	86
	0.19	11	4180	23740	9110	384
		22	4060	15910	2120	64

The fit parameters of the Findley power law model were determined for upper time limits of 250 h and 1000 h, Table 22. The parameter ε_0 represents the initial elastic strain and increases with the initial stress and decreasing v_F. The elastic modulus E_1 corresponds to the moduli of the Burgers model and the moduli determined by TT and IET. The power coefficient n ranges from 0.35 to 0.55, meaning that the Findley model can describe only primary creep. As n increases with the initial stresses, it provides enhanced creep. The introduction of glass beads leads to the smaller n indicating the reduction of the creep. Interestingly, n remains unchanged if the upper fitting time limit is increased from 250 h to 1000 h indicating that n can be determined by short-term creep data to predict long term creep.

The transient strain ε^+ corresponds to the creep strain after 1 h, which should increase with the initial stress. This is only true for the neat PBT, whereas it decreases for the GB filled PBT. Furthermore, the transient strains ε^+ of the GB filled PBT exceed those of the neat PBT by a factor 2 to 3 indicating an enhanced strain rate for GB filled PBT during the first hour of the creep before the creep equilibrium is established.

Table 22 Fit parameters of Findley model according to measured creep compliances at varying initial stresses of neat PBT, PBT GB20, and PBT GB30 showing the effect of chosen fitting time ranges.

range of fitting time	GB content v_F	initial stress σ_0	parameters of Findley power law model			
			ε_0	ε^+	n	$E_1 = \sigma_0/\varepsilon_0$
h	-	MPa	10^{-2}	10^{-6}	-	MPa
0 to 250	0	11	0.41	2.21	0.47	2690
		17	0.64	2.54	0.52	2657
		22	0.86	3.40	0.55	2545
	20	17	0.47	8.73	0.42	3629
		22	0.62	8.36	0.46	3529
	30	11	0.27	7.58	0.35	4149
		22	0.56	6.23	0.48	3907
0 to 1000	0	11	0.41	2.23	0.47	2666
		17	0.64	2.54	0.52	2657
		22	0.86	3.41	0.55	2546
	20	17	0.47	9.06	0.42	3636
		22	0.62	8.36	0.46	3526
	30	11	0.26	8.02	0.35	4165
		22	0.56	6.63	0.48	3929

The models of Findley and Burgers provide parameter sets adaptable to measured data but are not able to predict the creep behavior on base of matrix creep data. Furthermore, they do not consider effects of interfacial adhesion at all.

The EVC model, Eq. (57), predicts creep compliances of PMC having perfect interfacial adhesion ($k_{adh} = 1$) if the creep compliance of the matrix is known. Using the creep compliance of neat PBT with Eq. (57) showed that the predicted compliances were too small. However, the introduction of k_{adh} with values decreasing stepwise from 1 to 0 increases the calculated creep compliances, Fig. 46 – green lines. With decreasing adhesion coefficients, the calculated creep compliances approach the measured ones for k_{adh} between 0.6 and 0.4. Furthermore, it is obvious that k_{adh} is not a constant but a time dependent function. The time dependent interfacial adhesion $k_{adh}(t)$ was determined by pointwise fitting and is displayed in Fig. 46 by red bullet points. It decreases with time indicating that the interfacial adhesion is weakened during the creep experiment. The initial k_{adh} coincide well with those obtained from stiffness modeling.

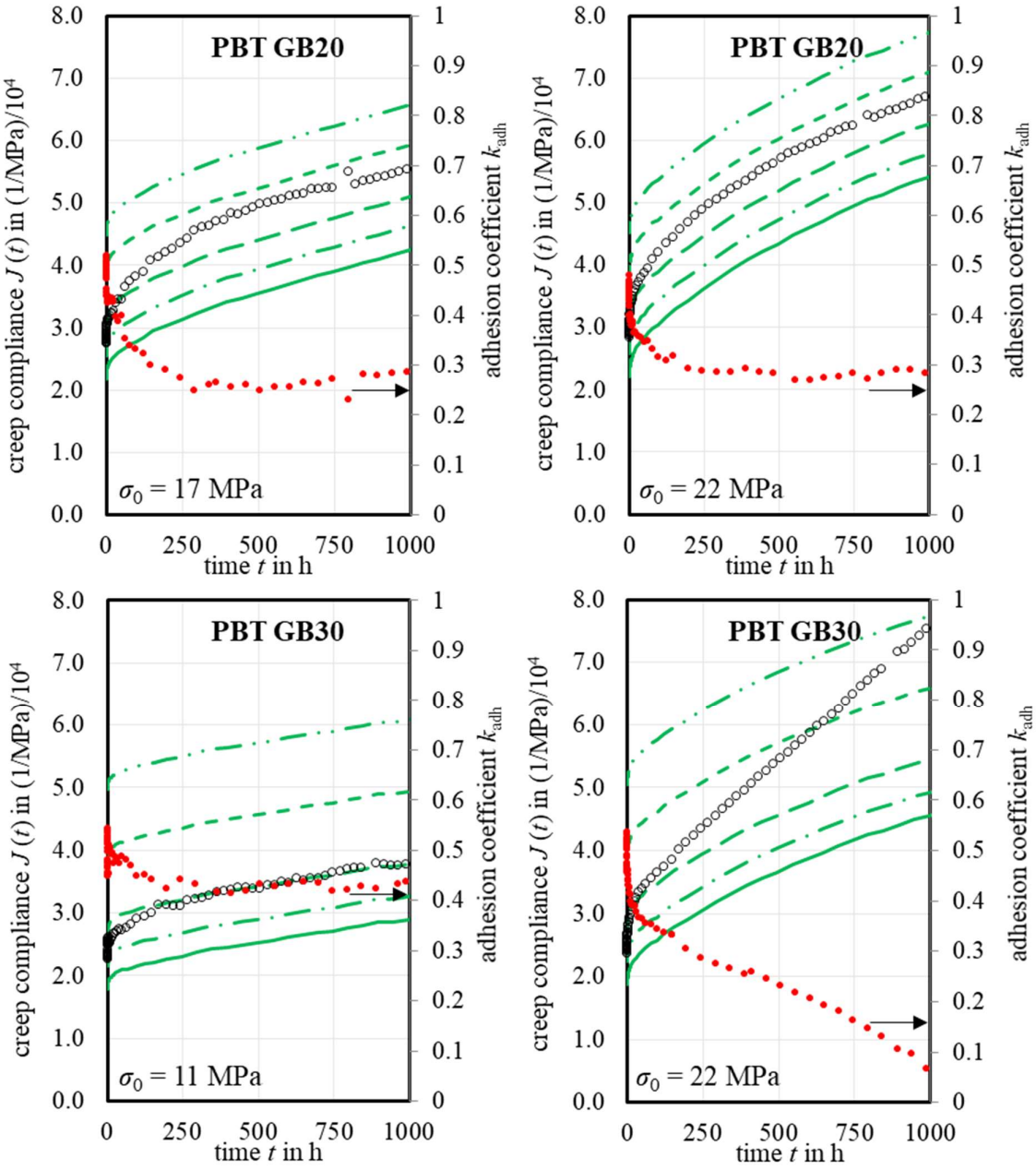

Fig. 46 Measured creep compliances (o) *of PBT GB20 / PBT GB30 compared to calculated ones with adhesion coefficients k_{adh} = 0, 0.2, 0.4, 0.6, and 1 (lines from top to bottom) for various initial stresses and pointwise evaluated adhesion coefficients* (•).

Over 250 h, k_{adh} decreases from 0.55 to 0.36 (PBT GB20 at σ_0 = 17 MPa), 0.50 to 0.32 (PBT GB20 at σ_0 = 22 MPa), 0.53 to 0.45 (PBT GB30 at σ_0 = 11 MPa), and 0.57 to 0.34 (PBT GB30 at σ_0 = 22 MPa). This decrease is faster the higher the initial stresses. Between 250 h and 1000 h, the asymptotic course of $k_{adh}(t)$ tends towards a final value except for PBT GB30 at σ_0 = 22 MPa.

The time dependency of the determined interfacial adhesions could be described by

$$k_{\mathrm{adh}}(t) = -\Delta k_{\mathrm{adh}} * \ln(t) + k_{\mathrm{adh}}^{t=1\,h} \tag{58}$$

with the incremental slope Δk_{adh} and initial adhesion coefficient $k_{\mathrm{adh}}^{t=1\,h}$. The fit parameters are depicted in Table 23.

Table 23 Fit parameters of the time dependent adhesion function of PBT PMC with correlation coefficient R_2.

range of fitting time	GB content v_F	initial stress σ_0	fit parameter of time-dependent adhesion function		
			Δk_{adh}	$k_{\mathrm{adh}}^{t=1\,\mathrm{h}}$	R_2
h	-	MPa	-	-	%
0 to 250	0.12	17	0.017	0.45	95.2
		22	0.016	0.41	99.4
	0.19	11	0.008	0.49	92.4
		22	0.021	0.45	99.0
0 to 1000	0.12	17	0.022	0.45	94.6
		22	0.017	0.41	99.3
	0.19	11	0.009	0.49	92.5
		22	0.027	0.44	97.9
0 – 150, **log**		22	0.020	0.45	99.4
150 – 1000, **lin**		22	0.123	0.97	99.6

For the fitting time limit of 250 h and 1000 h, the $k_{\mathrm{adh}}^{t=1\,\mathrm{h}}$ decrease with the initial stress. However, PBT GB20 show decreasing Δk_{adh} whereas for PBT GB30 increasing Δk_{adh} occur, which can be attributed to the effects of the asymptotic behavior for long times. For PBT GB30 at 22 MPa, the segmental fitting procedure due to the occurrence of the secondary creep provides better fitting of the measured creep compliance.

Introducing the time dependency of $k_{\mathrm{adh}}(t)$ according to Eq. (58) leads to a good adaption to measured creep data, Fig. 47. Only PBT GB30 required a two-step fit procedure assuming a linear decrease of $k_{\mathrm{adh}}(t)$ during secondary creep for times exceeding 150 h.

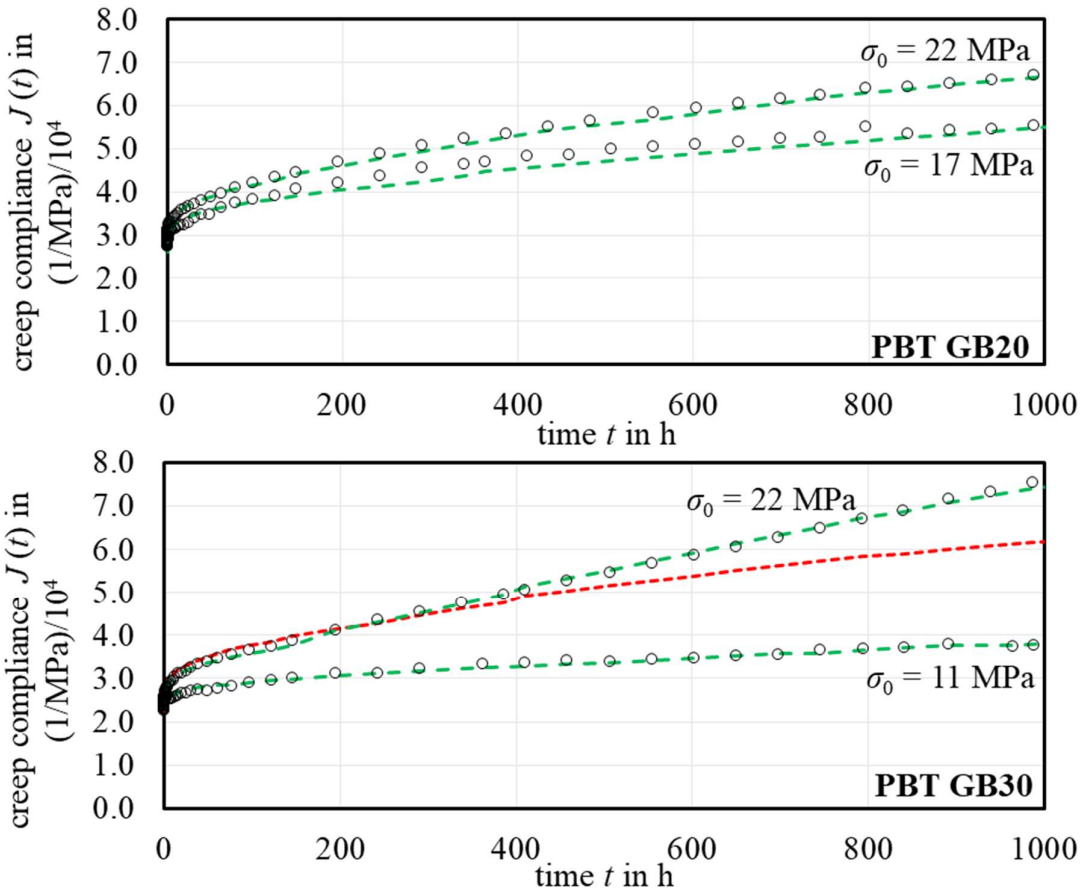

Fig. 47 Comparison of measured creep compliances (o) at varying initial stresses of PBT GB20 and PBT GB30 to calculated creep compliances (green) using Eq. (57) and (58), (red) represents the extrapolation of 250 h fit.

4.3.2 Theoretical viscoelastic considerations – Creep modeling of PMC with fibers

Modeling short fiber reinforced composites (SFRC) using the EVC extends the assumption of *cube in cube* to *cuboid in cuboid* introducing the aspect ratio r of the fiber as an additional parameter. The "macroscopic" creep strain $\varepsilon_{\mathrm{EV}}(t)$ differs from the microscopic strains of matrix part $\varepsilon_{\mathrm{M}}(t)$ and composite part $\varepsilon_{\mathrm{C}}(t)$ and depends also on the orientation of the fibers with respect to the load direction. Therefore, it is necessary to calculate the strains parallel to the fiber axis $\varepsilon_{\mathrm{EV}}^{\parallel}(t)$ and perpendicular to the fiber axis $\varepsilon_{\mathrm{EV}}^{\perp}(t)$. This requires the segmentation of the EV parallel and perpendicular to the fiber orientation, Fig. 48.

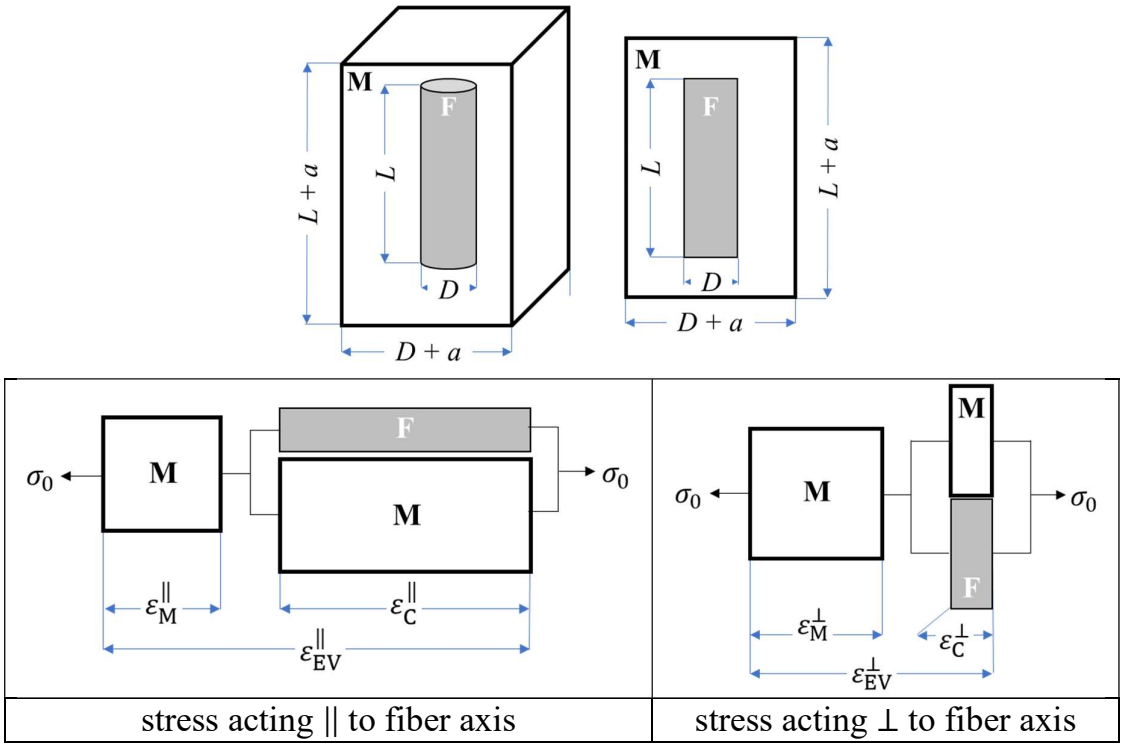

Fig. 48 Elementary volume containing a single fiber of length L and diameter D with distance a to the neighboring fiber and its segmentation in matrix part and composite part with stresses acting parallel ∥ and perpendicular ⊥ to the fiber axis.

Case 1: Stress σ_0 acts parallel to fiber axis

The strain of the EV due to the initial stress σ_0 acting parallel to the fiber direction is given by

$$\varepsilon_{\mathrm{EV}}^{\parallel} = \frac{\Delta(L+a)}{(L+a)} = \frac{\Delta L}{(L+a)} + \frac{\Delta a}{(L+a)} = \frac{L}{(L+a)} \underbrace{\frac{\Delta L}{L}}_{=\varepsilon_{\mathrm{C}}^{\parallel}} + \frac{a}{(L+a)} \underbrace{\frac{\Delta a}{a}}_{=\varepsilon_{\mathrm{M}}^{\parallel}} \tag{59}$$

Extending denominator and nominator with the fiber diameter D yields

$$\varepsilon_{\mathrm{EV}}^{\parallel} = \frac{r}{(r+d)}\,\varepsilon_{\mathrm{C}}^{\parallel} + \frac{d}{(r+d)}\,\varepsilon_{\mathrm{M}}^{\parallel} \tag{60}$$

with aspect ratio r and normalized fiber distance d defined as

$$d = d(v_{\mathrm{F}}, r) = \frac{a}{D} \tag{61}$$

Case 2: Stress σ_0 acts perpendicular to fiber axis

The strain of the EV due to the initial stress σ_0 acting perpendicular to the fiber direction is given by

$$\varepsilon_{\mathrm{EV}}^{\perp} = \frac{\Delta(D+a)}{(D+a)} \tag{62}$$

As the fiber has a circular cross-section the reference lengths of matrix part and composite part have to be corrected by the geometry constant k,

$$\varepsilon_{\mathrm{EV}}^{\perp} = \frac{\Delta k\, D}{(D+a)} + \frac{\Delta a + \Delta(1-k)\, D}{(L+a)} = \frac{k\, D}{(D+a)} \underbrace{\frac{\Delta L}{k\, D}}_{=\varepsilon_{\mathrm{C}}^{\perp}} + \frac{a+(1-k)\, D}{(D+a)} \underbrace{\frac{\Delta a}{a+(1-k)\, D}}_{=\varepsilon_{\mathrm{M}}^{\perp}} \tag{63}$$

which depends on the shape of the inclusion. For short fibers it can be determined by conversion to a square column shaped fiber having same length L and cross-section A.

$$A_{\mathrm{fiber}} = \frac{\pi}{4} D^2 = A_{\mathrm{square\ column}} = k^2 D^2 \Rightarrow k = \sqrt{\frac{\pi}{4}} \cong 0.886 \tag{64}$$

Extending denominator and nominator with the fiber diameter D yields

$$\varepsilon_{\mathrm{EV}}^{\perp} = \frac{k}{(1+d)}\, \varepsilon_{\mathrm{C}}^{\perp} + \frac{d+1-k}{(1+d)}\, \varepsilon_{\mathrm{M}}^{\perp} \tag{65}$$

Eq. (60) and (65) link the macroscopic strain of the EV to microscopic strains of both matrix part and composite part with weighting factors only depending on the geometry of the EV. In case of creep experiments, all strains of Eq. (60) and (65) depend on time and initial stress. Dividing these strains by the initial stress σ_0 yields the time- and stress-dependent creep compliance parallel to the fiber axis

$$J_{\mathrm{EV}}^{\parallel}(t,\sigma_0) = \frac{r}{(r+d)}\, J_{\mathrm{C}}^{\parallel}(t,\sigma_0) + \frac{d}{(r+d)}\, J_{\mathrm{M}}^{\parallel}(t,\sigma_0) \tag{66}$$

and perpendicular to the fiber axis

$$J_{\mathrm{EV}}^{\perp}(t,\sigma_0) = \frac{k}{(1+d)}\, J_{\mathrm{C}}^{\perp}(t,\sigma_0) + \frac{d+1-k}{(1+d)}\, J_{\mathrm{M}}^{\perp}(t,\sigma_0) \tag{67}$$

As mentioned before, if the initial stresses σ_0 remain small compared to the yield stresses σ_y one can assume that the composite part behaves elastically. This means that the creep compliances of the filler $J_{\mathrm{C}}^{\parallel}(t,\sigma_0)$ and $J_{\mathrm{C}}^{\perp}(t,\sigma_0)$ remain constant and can be substituted by the corresponding compliances at $t = 0$ given by the reciprocal moduli of the composite part leading to

$$J_{\mathrm{EV}}^{\parallel}(t,\sigma_0) = \frac{r}{(r+d)} \underbrace{\frac{1}{E_{\mathrm{F}}\, A_{\mathrm{F}}^{\parallel} + E_{\mathrm{M}}\left(1-A_{\mathrm{F}}^{\parallel}\right)}}_{=\frac{1}{E_{\mathrm{composite\ part}}^{\parallel}}} + \frac{d}{(r+d)}\, J_{\mathrm{M}}^{\parallel}(t,\sigma_0) \quad \text{with } A_{\mathrm{F}}^{\parallel} = \frac{\frac{\pi}{4}}{(1+d)^2} \tag{68}$$

and

$$J_{\mathrm{EV}}^{\perp}(t,\sigma_0) = \frac{k}{(1+d)} \underbrace{\frac{1}{E_{\mathrm{F}}\, A_{\mathrm{F}}^{\perp} + E_{\mathrm{M}}\left(1-A_{\mathrm{F}}^{\perp}\right)}}_{=\frac{1}{E_{\mathrm{composite\ part}}^{\perp}}} + \frac{d+1-k}{(1+d)}\, J_{\mathrm{M}}^{\perp}(t,\sigma_0) \quad \text{with } A_{\mathrm{F}}^{\perp} = \frac{k\, r}{(r+d)\,(1+d)} \tag{69}$$

with fiber modulus E_F, matrix modulus E_M, relative cross-sections of fiber parallel to the fiber axis $A_F^{\parallel}$ and perpendicular to the fiber axis $A_F^{\perp}$. From Eq. (68) and (69) can be concluded that the creep compliances of SFRC are completely determined by the creep compliances of the matrix as long as the applied stresses remain small compared to the yield stresses. Thus, the ultimate creep compliances of SFRC with known fiber volume content and aspect ratio can be calculated only by measured creep compliances of the matrix at the given initial stresses.

As aspect ratio r and fiber volume content v_F are accessible parameters, the normalized fiber distance d becomes a function of the fiber volume content v_F and can be estimated according to [149] by the following expression

$$d = d(v_F) = \left(\frac{\pi}{4v_F}\right)^{1/2} - 1 \tag{70}$$

yielding in a v_F-dependent decrease of the normalized fiber distance $d(v_F)$, Fig. 49.

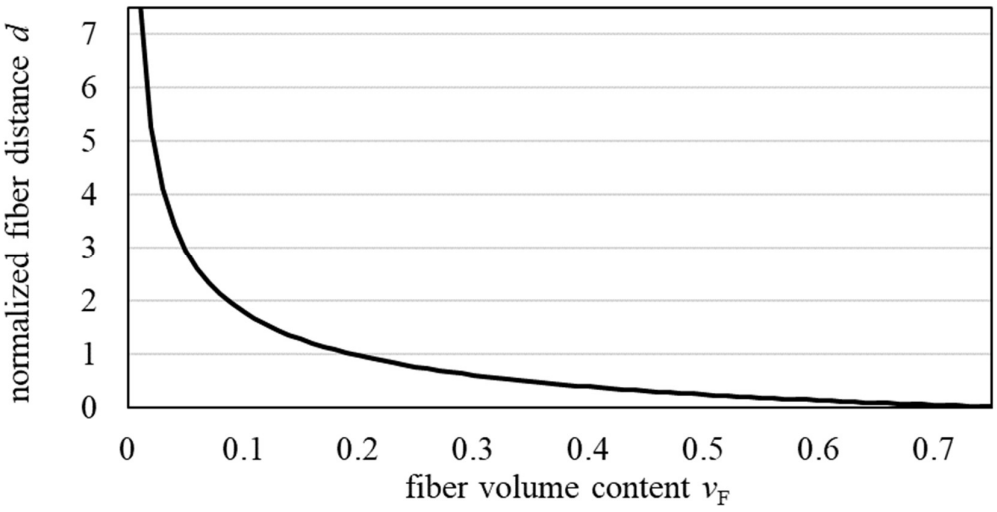

Fig. 49 Normalized fiber distance d as a function of the fiber volume content v_F.

Application: Creep modeling of short fiber reinforced composites (SFRC)

The influence of the manufacturing process was previously analysed by tensile tests according to ISO 527, Table 24. For neat PBT, conventional injection molding (CIM) yields slightly smaller Young´s moduli E and yield stresses σ_y compared to push pull processing (PPP). For PMC, fiber orientation during processing due to shear and elongational flows is reflected by the mechanical properties. Longitudinal E of PBT GF20 and PBT GF30 are 50 % higher for CIM and 80 % higher for PPP compared to neat PBT. PMC´s σ_y parallel to the flow direction (∥) are 100 % higher for CIM and PPP compared to neat PBT whereas for CIM σ_y perpendicular to the flow direction (⊥) are increased only by 30 %, and for PPP σ_y of neat PBT are not exceeded.

Table 24 Young´s moduli E, yield stress σ_y and yield strain ε_y of PBT composites determined according to ISO 527 with respect to the processing technique - conventional injection molding (CIM) or push pull processing (PPP).

		Young's modulus E MPa	yield stress σ_y MPa	yield strain ε_y %	E for EVC MPa
PBT	CIM ∥	2385 ± 64	52.6 ± 1	3 ± 0.01	2400
	CIM ⊥	2417 ± 10	53.3 ± 0.1	3.02 ± 0.02	
	PPP ∥	2524 ± 45	54.5 ± 0.4	3.05 ± 0.2	2500
	PPP ⊥	2492 ± 54	54.6 ± 0.1	3.07 ± 0.05	
PBT GF20	CIM ∥	5498 ± 211	100 ± 3.8	3.05 ± 0.19	5500
	CIM ⊥	3882 ± 108	69.3 ± 1.3	3.88 ± 0.1	3900
	PPP ∥	6207 ± 273	105 ± 1.9	2.66 ± 0.16	6200
	PPP ⊥	3642 ± 140	50.8 ± 1.1	1.9 ± 0.11	3650
PBT GF30	CIM ∥	7400 ± 373	115.8 ± 0.8	2.52 ± 0.4	7400
	CIM ⊥	4427 ± 111	68.4 ± 1.8	3.77 ± 0.06	4400
	PPP ∥	8692 ± 103	101 ± 5.6	1.51 ± 0.11	8700
	PPP ⊥	4308 ± 315	46.2 ± 1.8	1.31 ± 0.04	4300

The initial creep compliances of neat PBT are smaller for PPP (0.38 GPa^{-1}) than for CIM (0.42 GPa^{-1}) due to different matrix stiffnesses. This initial creep compliance is independent of the initial stress. With increasing creep time PBT exhibits a pronounced time and stress dependency shown by the splitting of the creep compliance curves. The same behavior occurs for both PBT GF20 and PBT GF30 ⊥ to the flow direction indicating that nonlinear creep behavior is pronounced at initial stresses of 25 MPa and 37.5 MPa for creep times exceeding approx. 10000 s. For PMC tested ∥ to the flow direction no splitting is observed. Furthermore, the introduction of glass fibers reduces the initial creep compliances of PBT GF20 to approximately 0.25 – 0.27 GPa^{-1} for ⊥ and 0.15 – 0.17 GPa^{-1} for ∥, and for PBT GF30 to approximately 0.21 GPa^{-1} for ⊥ and 0.11 – 0.13 GPa^{-1} for ∥, Fig. 50. The creep rates decrease as well with increasing GF content. The CIM specimens exhibit a linear viscoelastic behavior up to initial stresses of 25 MPa ⊥ to the flow direction and up to 37.5 MPa ∥ to the flow direction. PPP specimens of PBT GF20 do not behave linear viscoelastically ⊥ to the flow direction and exhibit more creep than the CIM specimens, and at 37.5 MPa fracture occurs after one day. The corresponding PBT GF30 samples exhibit linear viscoelastic behavior up to initial stresses of 25 MPa but fracture after 2 to 20 minutes at 37.5 MPa. This indicates that the matrix deformability decreases with GF content for stresses close to σ_y of the matrix. Parallel to the flow direction,

the creep compliances of both PBT GF20 and PBT GF30 coincide for all initial stresses within the experimental error, indicating linear viscoelastic behavior up to at least 37.5 MPa.

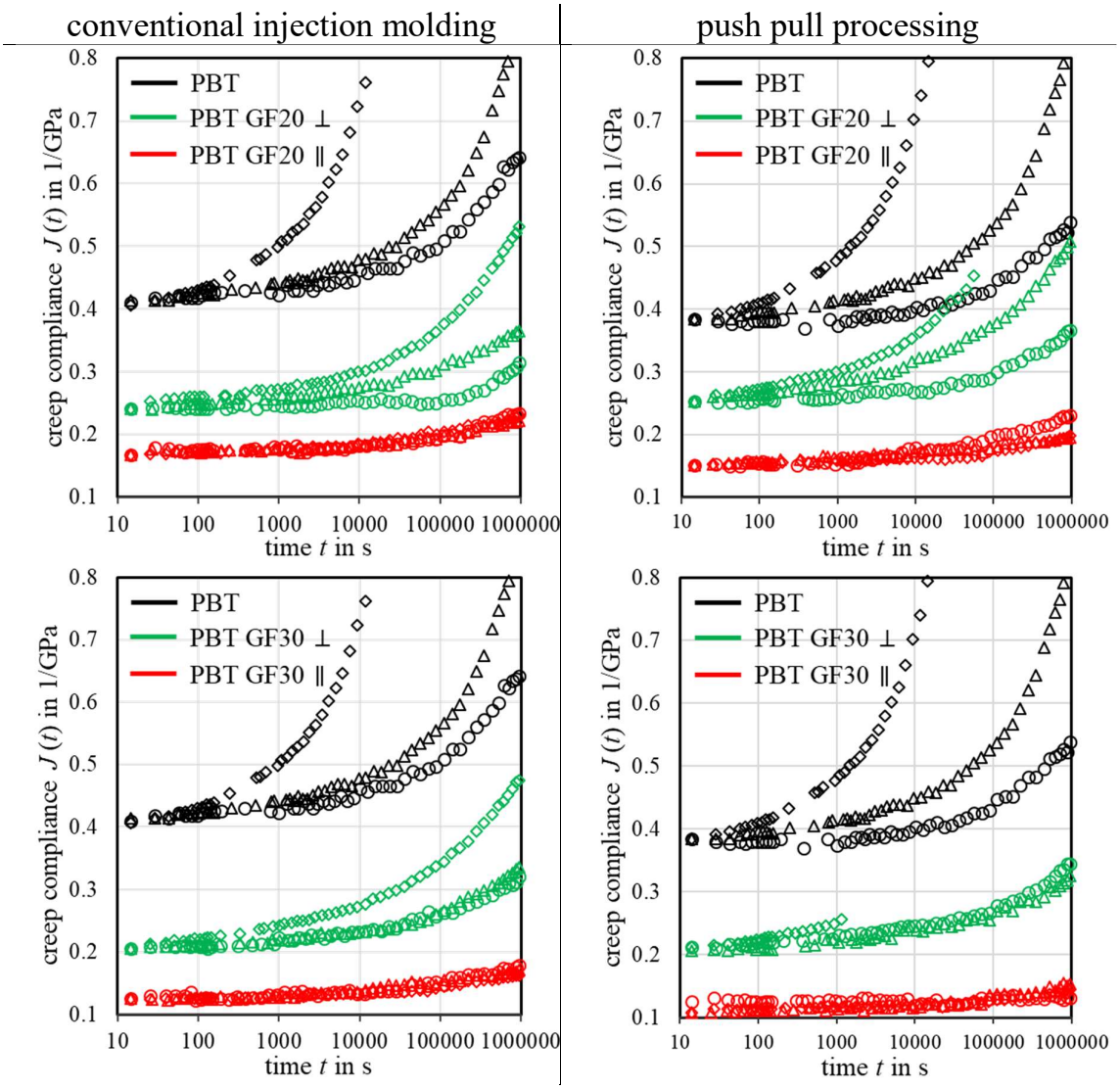

* initial stress σ_0: ○ = 12.5 MPa, Δ = 25 MPa, ◊ = 37.5 MPa

Fig. 50 Creep compliances of neat PBT, PBT GF20 and PBT GF30 determined parallel and perpendicular to the flow direction for initial stresses σ_0 of 12.5 MPa (○), 25 MPa (Δ), 37.5 MPa (◊).

The EVC model for SFRC necessitates the fiber orientation distribution to account anisotropic behaviour according to [150], and the mean aspect ratio r. Their experimental values are shown in Table 25. It can be seen that the injection molding process causes a fiber length degradation being 20 % to 30 % more pronounced for PPP and the higher the v_F. Furthermore, the orientation factors reveal a preferential fiber orientation in flow direction being more pronounced for PPP compared to CIM. However, for both processing techniques orientation factors f_3 in thickness direction are close to "0" implying a laminate state.

Table 25 Effects of processing – conventional injection molding (CIM) or push pull processing (PPP) – on mean fiber length (MFL), mean fiber distance (MFD), aspect ratio (fiber diameter of 7 µm according to the manufacturer) and orientation factors

PMC	v_F	processing	MFL $\langle L \rangle$*	MFD $d(v_F)$	aspect ratio r	orientation factors $f_1 = \cos^2 q$	f_2	f_3
	-		µm	µm	-	-	-	-
PBT GF20	0.09	granules	255	1.95	36	-	-	-
		PPP	212		30	0.753	0.211	0.036
		CIM	235		34	0.713	0.253	0.034
PBT GF30	0.13	granules	288	1.46	41	-	-	-
		PPP	199		28	0.800	0.173	0.027
		CIM	200		28	0.705	0.261	0.034

*MFL and MFD abbreviates mean fiber length and mean fiber distance, respectively.

However, Eq. (68) and (69) represent the creep compliances ∥ and ⊥ to the fiber orientation for unidirectional fiber reinforced composites. In a real SFRC the fibers are misaligned by an angle Θ to the direction of the external load σ_0. This requires a spatial transformation to account for the fiber misalignment with respect to the main axes, **appendix B**. The transformation brings the shear modulus G_{12} into play which was not measured. However, the EVC allows for its derivation from E_{22} because both are formally identical within the EVC what yields the shear correction factor g_J

$$g_J = 2(1+\mu_M)\left[\frac{1+\frac{(1+d-k)\frac{(\mu_M-\mu_F)}{(1+\mu_F)}E_R+(1+d-k)\frac{(\mu_M-\mu_F)}{(1+\mu_F)}A_F^{\perp}E_R}{k+(1+d-k)(E_R-1)+(1+d-k)A_F^{\perp}(E_R-1)}}{1+\frac{\frac{(\mu_M-\mu_F)}{(1+\mu_F)}A_F^{\perp}E_R}{1+A_F^{\perp}(E_R-1)}}\right] \quad (71)$$

with relative modulus E_R, Poisson's ratios μ of fiber and matrix and the geometry of the EV given by aspect ratio r, normalized fiber distance d, and efficiency factor k.

The shear deformation of the misaligned fibers is not caused by the initial stress σ_0 but by the shear stress σ_{0t}, Fig. 51.

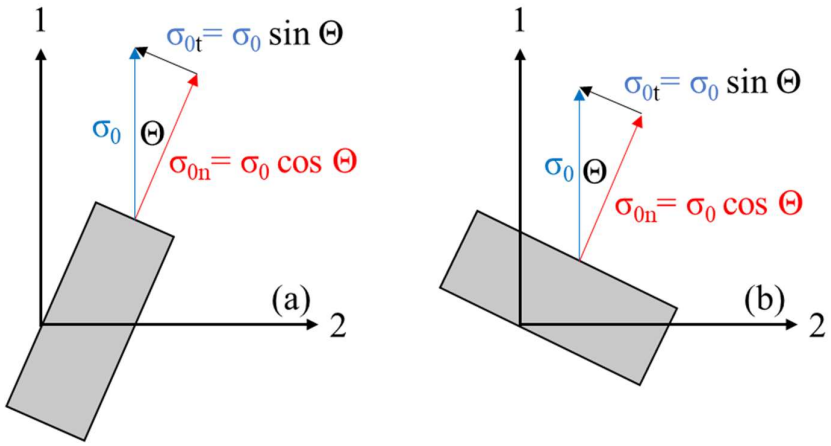

Fig. 51 Determination of effective stresses considering a fiber misalignment Θ.

The shear stress is given by

$$\sigma_{0t} = \sigma_0 \sin\theta \tag{72}$$

with misalignment angle Θ. Thus, the shear correction factor g_J in Eq. (71) has to be changed to

$$G_J = g_J \sin\theta \tag{73}$$

with the effective shear correction factor G_J.

The creep compliance $\bar{J}_{11}(t,\sigma_0)$ parallel to the flow direction is given by

$$\begin{aligned}\bar{J}_{11}(t,\sigma_0) &= J_{11}(t,\sigma_0)\cos^4\theta - 2\mu_{12}\,J_{11}(t,\sigma_0)\sin^2\theta\cos^2\theta \\ &\quad + g_J\,J_{22}(t,\sigma_0)\sin^3\theta\cos^2\theta + J_{22}(t,\sigma_0)\sin^4\theta \\ &= J_{11}(t,\sigma_0)\cos^4\theta - 2\mu_{12}\,J_{11}(t,\sigma_0)\sin^2\theta\cos^2\theta \\ &\quad + G_J\,J_{22}(t,\sigma_0)\sin^2\theta\cos^2\theta + J_{22}(t,\sigma_0)\sin^4\theta\end{aligned} \tag{74}$$

and the measured creep compliance $\bar{J}_{22}(t,\sigma_0)$ perpendicular to the flow direction to

$$\begin{aligned}\bar{J}_{22}(t,\sigma_0) &= J_{11}(t,\sigma_0)\sin^4\theta - 2\mu_{12}\,J_{11}(t,\sigma_0)\sin^2\theta\cos^2\theta \\ &\quad + g_J\,J_{22}(t,\sigma_0)\sin^3\theta\cos^2\theta + J_{22}(t,\sigma_0)\cos^4\theta \\ &= J_{11}(t,\sigma_0)\sin^4\theta - 2\mu_{12}\,J_{11}(t,\sigma_0)\sin^2\theta\cos^2\theta \\ &\quad + G_J\,J_{22}(t,\sigma_0)\sin^2\theta\cos^2\theta + J_{22}(t,\sigma_0)\cos^4\theta\end{aligned} \tag{75}$$

Calculated creep compliances according to Eq. (74) and (75) were compared to measured ones of PBT GF20 and PBT GF30 exemplary for σ_0 = 12.5 MPa, Fig. 52. The required input data were taken from Table 24 and 25. Poisson's ratios μ_{12} were calculated to 0.0044 (PBT GF20) and 0.0061 (PBT GF30) being both close to zero. These small Poisson's ratios result from the highly oriented long fibers that prevent most of the contraction in fiber direction.

The ultimate creep compliances ∥ and ⊥ to the flow direction fall below and exceed the measured creep compliances, respectively, acting as the upper and lower bounds. Furthermore, the measured creep compliances always exceed the predictions, but especially the time dependency is reproduced quite well, Fig. 52. These results base on the assumptions of perfect fiber matrix adhesion and purely elastic behavior of the composite part. A reduced interfacial adhesion should lead to higher compliances.

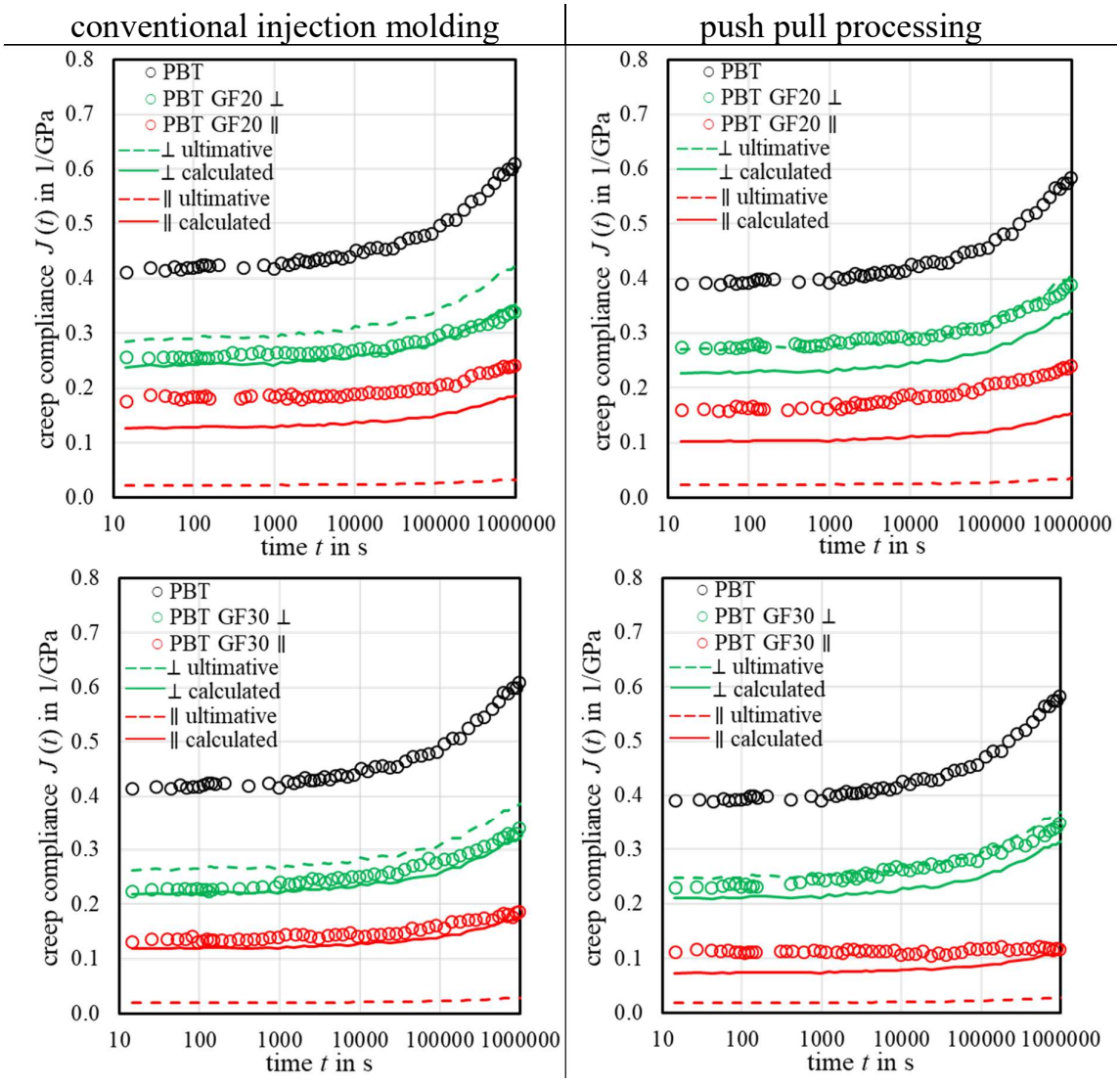

* initial stress σ_0: ○ = 12.5 MPa, E_F for calculation: 74 GPa

Fig. 52 Comparison of measured (symbols), calculated (solid lines) and ultimate creep compliances (dashed lines) for PBT GF20 and PBT GF30 considering the manufacturing process – CIM left, PPP right; ⊥ data in green, ∥ data in red – σ_0 = 12.5 MPa

SEM images of fractured SFRC showed fiber surfaces largely covered with matrix material indicating a good fiber matrix adhesion. This behavior was more pronounced for fibers oriented perpendicular to the stress direction where the

interface is subjected to tensile stresses. In cases of good fiber matrix adhesion, the interface strength exceeds the shear strength of the matrix. If the tensile stress approaches the shear strength the matrix still adheres well to the fibers but starts to exhibit shear flow failure in the vicinity of the fibers. If fracture occurs, a zigzag-shaped matrix structure on the fiber surface is generated due to shear flows in 45°, Fig. 53 (a) and (b). For fibers oriented ∥ to the stress direction, the external tensile stress is transferred by shear stresses along the interface to the fibers. Due to this stress transfer mechanism, the end regions of the fibers are subjected to a constant maximum shear stress. If this shear stress corresponds to the shear strength of the matrix, the matrix slides along the fiber surface leading to fiber pull out and delamination. Consequently, end regions of fibers oriented parallel to the stress exhibit hardly any matrix adherences, Fig. 53 (c) and (d). Matrix adherences were mainly visible on fibers that are clearly oriented ⊥ to the stress direction. Thus, the SEM images of the fracture surfaces showed that the fiber matrix adhesion was good but not perfect and further depending on the stress direction in the interface.

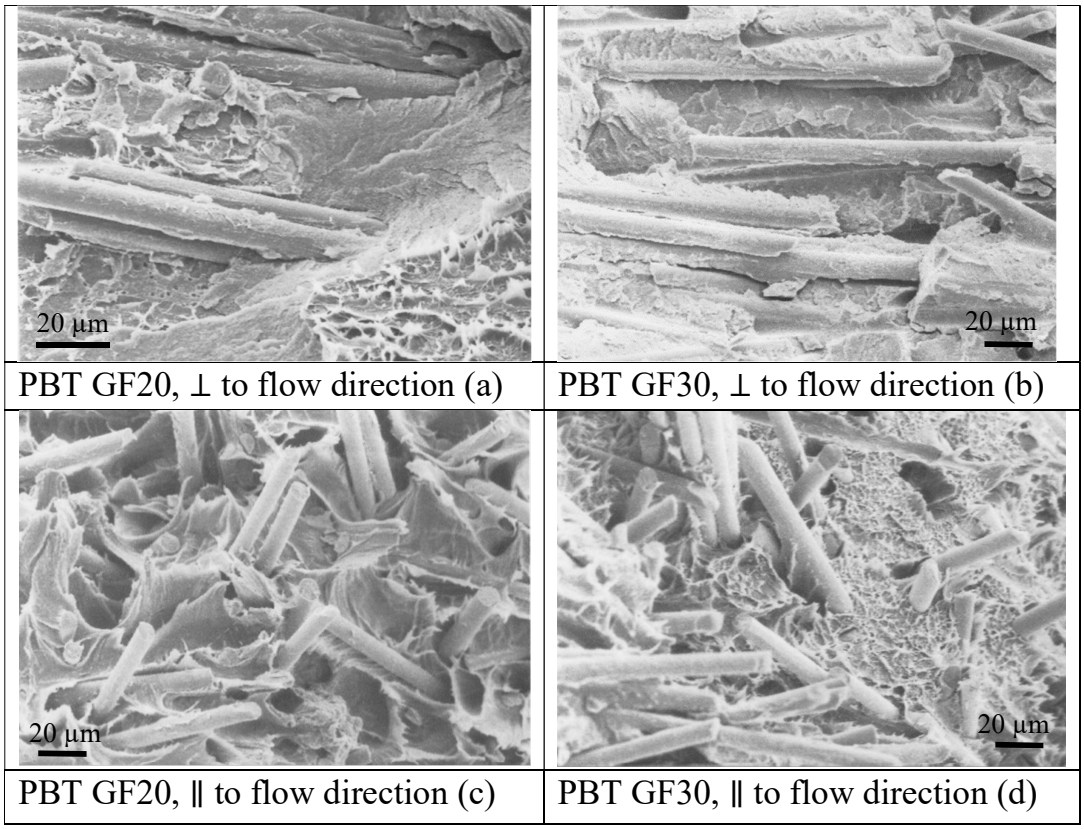

PBT GF20, ⊥ to flow direction (a)	PBT GF30, ⊥ to flow direction (b)
PBT GF20, ∥ to flow direction (c)	PBT GF30, ∥ to flow direction (d)

Fig. 53 SEM images of fractured PBT GF20 and PBT GF30 parallel and perpendicular to the fiber orientation, investigated at 10 kV.

These morphological findings confirm the results of the EVC model for SFRC as the differences between measured and calculated creep compliances occur due

to a none-perfect interfacial adhesion. This might be overcome by the introduction of an adhesion coefficient k_{adh} as it reduces the load transfer to the fibers, thus, increasing the creep compliances. However, the fracture and failure behavior of SFRC, Fig. 53, imply that k_{adh} depends either on the angle between initial stress direction and fiber orientation or that one has to distinguish two adhesion coefficients assigning tensile and shear failure, respectively.

Noticeably, the time range in which the time dependency of the matrix creep corresponds to the creep of SFRC decreases with increasing initial stress. Therefore, a creep time limit t_{limit} was introduced to account for the validity of the EVC by determining the relative deviations of measured and calculated creep compliances ∥ and ⊥ to the flow direction.

$$\Delta J_{\mathrm{rel}}(t) = \frac{J_{\mathrm{meas}}(t) - J_{\mathrm{calc}}(t)}{J_{\mathrm{meas}}(t)} \tag{76}$$

The creep time limit is assumed to be achieved if $\Delta J_{\mathrm{rel}}(t)$ becomes smaller than 80 % of $\Delta J_{\mathrm{rel}}(t = 0)$.

$$\Delta\Delta J_{\mathrm{rel}}(t = t_{\mathrm{limi}}) = 0.8\ \Delta J_{\mathrm{rel}}(t = 0) \tag{77}$$

From Table 26 it can be seen that t_{limit} decreases roughly a factor 30 with each increase of the initial stress and achieves shorter times if the stress acts perpendicular to the flow direction. Furthermore, $\Delta J_{rel,\parallel}$ exceeds $\Delta J_{rel,\perp}$ a factor 2 to 4 indicating that the composite part of the EV has to exhibit some shear creep of its matrix not taken into account by the modeling yet.

Table 26 Creep time limits t_{limit} and relative deviations of calculated and measured creep compliances at varying initial stresses.

Composite	initial stress σ_0	creep time limit $t_{limit,\parallel}$	creep time limit $t_{limit,\perp}$	rel. dev. of ΔJ_{rel} to $t_{limit,\parallel}$	rel. dev. of ΔJ_{rel} to $t_{limit,\perp}$
	MPa	s	s	%	%
PBT GF20 CIM	12.5	614072	350825	28	4.5
	25	23321	2905	27.5	3.4
	37.5	535	220	28.1	5.8
PBT GF20 PPP	12.5	>1217441	441259	37.9	16.4
	25	56666	350615	34.7	16.7
	37.5	535	1220	34.5	16.3
PBT GF30 CIM	12.5	441259	>1217441	11.9	5.5
	25	56666	12310	9.5	2.1
	37.5	220	535	10.4	3.3
PBT GF30 PPP	12.5	23535*	614072	32.9	12
	25	36225	23321	34.1	8.9
	37.5	844	387	33.9	12

*$t_{limit,\parallel}$ is determined too small because the measured creep compliance curve exhibits a small shift to slightly reduced values at creep times of 10,000 s, 23,535 s and 221,926 s; correction of these shifts leads to a $t_{limit,\parallel}$ = 614072 s

Plotting the creep time limits t_{limit} of Table 26 versus the initial stresses σ_0 yields a logarithmic dependency

$$\sigma_{0,i} = a_1 \lg \frac{t_{limit,i}}{t_0} + a_0 \tag{78}$$

with reference time t_0, e.g. 1 s, fit parameters slope a_1 and interception a_0. Solving Eq. (78) with respect to the creep time limit yields an exponential decrease

$$t_{limit,i} = t_0 * 10^{-\frac{a_0 - \sigma_{0,i}}{a_1}} \cong t_0 * 10^{-\frac{\sigma_y - \sigma_{0,i}}{a_1}} \tag{79}$$

with initial stress of level i $\sigma_{0,i}$ and yield stress σ_y implying that the creep behavior of SFRC PBT can be predicted by the matrix creep with sufficient accuracy if the initial load does not exceed 12.5 MPa ($\approx \sigma_y/4$).

5 Conclusion

In this PhD thesis an elaborate mechanical characterization was performed to account for the process-structure-property relationship of selected polymer matrix composites (PMC) – polyamide 66 (PA66) and poly(butylene terephthalate) (PBT) reinforced with various glass bead (GB) contents. The time-dependent mechanical behavior of these PMC filled with GB was investigated using long-term creep testing as well as PBT fiber composites. Furthermore, a model was developed to determine both elastic and viscoelastic properties taking into account interfacial adhesion. The elementary volume concept (EVC) is based on the *cube in cube* assumptions according to Paul and Ishai-Cohen. The appropriate segmentation in matrix and composites part allows to introduce an adhesion coefficient k_{adh} which serves as an area-dependent factor controlling the load transfer to the filler to predict Young´s modulus E and creep compliance $J(t)$.

PA66 and PBT reinforced with various GB contents were investigated using the standardized methods of tensile testing (TT), dynamic mechanical analysis (DMA), and oscillatory torsion (OT). These rather time-consuming methods were compared to the in the polymer field rarely used non-destructive measurement technique of impulse excitation technique (IET). Subsequently, the outcome of mechanical investigations was correlated to morphological and thermal findings. Notably, IET provided comparable moduli to all other methods and offered an easy access to Poisson´s ratio, which are important material properties for engineering and design. These findings were confirmed by finite element (FE) simulations. Comparing DMA and IET in flexural excitation, matching moduli were only found for DMA if the dynamic threshold amplitudes exceed 110 µm in amplitude sweep mode. This was attributed to an insufficient load transfer between sample and pushrod due to friction and sliding in the bearings. The moduli of IET in longitudinal and torsional excitation compared to TT and OT, respectively, were in good agreement but showed an increased error susceptibility for both TT and OT. Furthermore, inhomogeneous mechanical behavior was attributed to the skin core morphology of the test bars as well as varying crystallinities and GB concentrations. Therefore, the IET represents a promising measurement technique to determine elastic moduli of PMC in a cost-effective and non-destructive manner.

The EVC model was successfully introduced to predict both stiffness and creep compliances of spherical reinforced composites. With its input parameters E_M, E_F, $J_M(t)$, and ν_F, the EVC model allowed to account for interfacial adhesion with reasonable adhesion coefficient k_{adh} of 0.6 for PA66, 0.5 for PBT, 0.2 for isotactic polypropylene, 0.13 for low density polyethylene and 0.05 for butadiene rubber. These findings were in line with the corresponding surface energies. Further analysis elucidated that stiffening only occurs if k_{adh} exceeds $\sqrt{E_M/E_F}$. Additional FE simulations revealed that the EVC model is able to calculate correct moduli if

filler volume contents remain smaller than 20 % due to increasing interactions among filler particles and occurring shear flow.

The EVC model was further applied to analyze the creep behavior of GB reinforced PBT composites. The adhesion coefficient showed to be a time dependent function that controls the load transfer presumably via delamination processes and allowed to predict the creep compliances on the base of creep curves of neat matrix.

Creep modeling of GF reinforced PBT composites necessitated additional input such as mean fiber orientation to account for the misalignment between fiber and stress direction, and fiber aspect ratio. Creep compliances parallel and perpendicular to the fiber orientation were predicted systematically too small because of the assumption “perfect adhesion”. The introduction of adhesion functions requires further research as it turned out that the adhesion mechanisms differ for tensile and shear loading of the interface.

6 Contribution to science and practice

Increasing demands on performance and sustainability of polymer parts lead to the ever-increasing development of polymer matrix composites. This necessitates a fast availability of relevant thermophysical or mechanical properties.

This doctoral thesis provides substantial contributions to both scientific understanding and practical application in the field of polymer matrix composites, particularly with respect to their mechanical characterization and property prediction. The research addresses key challenges posed by the increasing complexity of composite materials, including inhomogeneity, interfacial behavior, and the demand for faster, yet accurate, evaluation techniques.

1) Predictive modeling of composite stiffness incorporating interfacial effects
   The development and implementation of a stiffness prediction model based on the elementary volume concept (EVC) enables engineers and researchers to predict the elastic properties of particle-filled composites without experimental testing. By accounting for interfacial adhesion effects, the model improves design reliability, supports virtual prototyping, and facilitates the integration of recycled or bio-based fillers with unknown adhesion properties.
2) Extension of the EVC model to time-dependent behavior
   The extension of the EVC to predict creep behavior introduces a valuable tool for long-term performance assessment of PMCs. It allows the estimation of creep compliance for varying filler contents and stress levels using only matrix properties and adhesion parameters. This reduces the need for time-consuming experimental campaigns and supports accelerated design cycles in automotive, consumer goods, or structural applications.
3) Orientation-sensitive modeling for fiber-reinforced composites
   The model's adaptability to fiber-filled systems, including direction-dependent compliance, represents a further step toward integrated material modeling. By differentiating adhesion effects under tensile and shear stress, the approach supports a more realistic simulation of mechanical behavior in anisotropic systems, such as injection-molded or aligned-fiber composites.
4) Advancement of fast and non-destructive testing methods
   The validation of the impulse excitation technique (IET) as a reliable tool for determining elastic moduli and Poisson's ratios in PMCs offers a practical alternative to conventional methods such as tensile testing or DMA. IET's non-destructive nature, rapid execution, and low material demand make it especially suitable for industrial quality control and for screening novel sustainable composite formulations with variable internal structures.

Overall, the findings of this work contribute to a deeper understanding of processing–structure–property relationships in heterogeneous composite systems and promote the broader adoption of fast, predictive, and sustainable approaches to composite design and evaluation.

References

[1] G.W. Milton. The theory of composites. Library of Congress Cataloging-in-Publication Data (2002), ISBN-13 978-1-4835-6919-2.

[2] S. Thomas. Polymer Composites. Wiley-VCH Verlag & Co.KgaA (2012), ISBN 978-3-527-32624-2.

[3] A.R. Bunsell, B. Harris. Hybrid carbon and glass fibre composites. *Composites* 5, 4 (1974), 157-164, https://doi.org/10.1016/0010-4361(74)90107-4.

[4] F. L. Matthews, R. D. Rawlings. Composite Materials: Engineering and Science. Woodhead Publishing (1974), ISBN 1-85573-473-7.

[5] R. W. Cahn, P. Haasen, E. J. Kramer. Materials science and technology. A comprehensive treatment – Volume 13 Structure and properties of composites. VCH Weinheim (1993), ISBN 3-527-26826-X.

[6] V. Serifi, M. Taric, D. Jevtic, A. Ristovski, M. Sahinagic-Isovic. Historical development of composite materials. The Annals of the University of Oradea. Economic Sciences (2018), DOI:10.15660/AUOFMTE.2018-3.3392.

[7] M.F. Ashby. Phil. Trans. R. Soc. London A (1987), pp. 393-407.

[8] W.B. Addis. Building: 3000 years of design engineering and construction. Phaidon Press (2015), ISBN 9780714869391

[9] L.H. Baekeland. The bakelizer. American Chemical Society (1993).

[10] I.H. Updegraff. Unsaturated Polyester Resins. In: Lubin, G. (eds) Handbook of Composites. Springer (1982), Boston, MA. https://doi.org/10.1007/978-1-4615-7139-1_2.

[11] G. Menges. Menges Werkstoffkunde Kunststoffe. Carl Hanser Verlag (2011), ISBN: 978-3-446-42762-4.

[12] A. Peacock, A. Calhoun. Polymer chemistry. Properties and applications. Carl Hanser Verlag (2006), pp 1-42, ISBN 3-446-22283-9.

[13] Data base Granta EduPack 2022 R2.

[14] J.G. Speight. Handbook of industrial hydrocarbon processes. Elsevier Inc. (2019), Chapter 14, ISBN 978-0-12-809923-0, https://doi.org/10.1016/C2015-0-06314-6.

[15] S. Thomas, C.J. Chirayil. Applications of unsaturated polyester resins: Synthesis, modifications, and preparation methods. Elsevier Science (2023), ISBN 978-0-32-399467-9.

[16] V. Mittal. Spherical and fibrous filler composites (1st ed.). John Wiley & Sons, Inc. (2016), https://doi.org/10.1002/9783527670222.

[17] C. Robeyns, L. Picard, F. Ganachaud. Synthesis, characterization and modification of silicone resins: An "augmented review". *Prog Org Coat* 125, 287-315 (2018), https://doi.org/10.1016/j.porgcoat.2018.03.025.

[18] W.W. Wright, M. Hallden-Abberton. Ullmann´s encyclopedia of industrial chemistry: Polyimides. Wiley-VCH, Weinheim (2002), ISBN 978-3527329434, doi:10.1002/14356007.a21_253.

[19] D. Stoye, W. Funke, L. Hoppe, et.al. Ullmann´s encyclopedia of industrial chemistry: Paints and coatings. Wiley-VCH, Weinheim (2006), ISBN 978-3527306732, doi:10.1002/14356007.a18_359.pub2.

[20] R.A. Shanks, I. Kong. General purpose elastomers: Structure, chemistry, physics and performance. In: Advances in Elastomers I, Springer Verlag (2013), 11-46, ISBN 078-3-642-20924-6, DOI:10.1007/978-3-642-20925-3_2.

[21] I.M. Daniel, O. Ishai. Engineering mechanics of composite materials. Oxford University Press Inc. (2005), ISBN 978-0-19-515097-1.

[22] https://www.oribicomposites.com/thermosets-vs-thermoplastics/ date of access: 19-01-2024.

[23] S. Thomas. Polymer Composites. Wiley-VCH Verlag & Co.KgaA (2012), ISBN 978-3-527-32624-2.

[24] T.A. Osswald, G. Menges. Material science of polymers for engineers. 3rd edition, Hanser, München (2012), ISBN 978-1-56990-514-2.

[25] T.D. Papathanasiou, I. Kuehnert, N.D. Polychronopoulos. 5 – Flow-induced alignment in injection molding of fiber-reinforced polymer composites. Editor(s): T.D. Papathanasiou, A. Bénard, In Woodhead Publishing Series in Composites Science and Engineering, Flow-Induced Alignment in Composite Materials (2nd Edition), Woodhead Publishing, 123-185 (2022), ISBN 978-0128185742, https://doi.org/10.1016/B978-0-12-818574-2.00001-4.

[26] S.R. Raisch. Teilchengefüllte Kunststoffe – Eigenschaften und Anwendungen am Beispiel wärmeleitfähiger und schirmender Compounds. Lecture as part of the module "Polymers and composites", Bonn-Rhein-Sieg University, Rheinbach (2024).

[27] H. Ho, L.T. Drzal. Non-linear numerical study of the single-fiber fragmentation test. Part I: Test mechanics. *Compos Eng* 5, 1231–44 (1995), https://doi.org/10.1016/0961-9526(95)00065-U.

[28] R. Freund, H. Watschke, J. Heubach, T. Vietor. Determination of influencing factors on interface strength of additively manufactured multi-material parts by material extrusion. *J Appl Sci* 9(9), 1782 (2019), https://doi.org/10.3390/app9091782.

[29] G. Fourche. An overview of the basic aspects of polymer adhesion. Part I: Fundamentals. *Polym Eng Sci* 35, 957–967 (1995), https://doi.org/10.1002/pen.760351202.

[30] N.A. de Bruyne. The Physics of Adhesion. *J Sci Instrum* 24, 29–35 (1947), DOI 10.1088/0950-7671/24/2/301.

[31] R. Freund, H. Watschke, J. Heubach, T. Vietor. Determination of influencing factors on interface strength of additively manufactured multi-material parts by material extrusion. *J Appl Sci* 9(9), 1782 (2019), https://doi.org/10.3390/app9091782.

[32] J.J. Bikerman. Causes of poor adhesion. *Indus Eng Chem* 59 (9), 40-44 (1967), https://doi.org/10.1021/ie51403a010.

[33] W. Brockmann, P.L. Geiß, J. Klingen, B. Schröder. Adhesive bonding: Materials, applications and technology. Wiley-VCH Verlag GmbH & Co. KgaA, 11–28 (2008), ISBN 9783527318988.

[34] G. Wypych. 2 – Mechanisms of adhesion. Handbook of Adhesion Promoters 5-44 (2018), https://doi.org/10.1016/B978-1-927885-29-1.50004-3.

[35] Z.B. Ahmad, M.F. Ashby, P.W.R. Beaumont. The contribution of particle-stretching to the fracture-toughness of rubber modified polymers. *Scr Metall* 20, 843-848 (1986), https://doi.org/10.1016/0036-9748(86)90452-7.

[36] H. Kargarzadeh, I. Ahmad, I. Abdullah. Mechanical properties of epoxy-rubber blends. In: J. Parameswaranpillai, N. Hameed, J. Pionteck, E. Woo (eds.). Handbook of Epoxy Blends. Springer International Publishing Switzerland (2015), ISBN 978-3-319-40041-9, DOI: 10.1007/978-3-319-18158-5_11-1.

[37] R.A. Pearson, A.F. Yee. Toughening mechanisms in thermoplastic-modified epoxies: 1. Modification using poly(phenylene oxide). *Polymer* 34 (17), 3658-3670 (1993), https://doi.org/10.1016/0032-3861(93)90051-B.

[38] J.W. Hutchinson. Mechanisms of toughening in ceramics. In: P. Germain, M. Piau, D. Caillerie (eds.). Theoretical and applied mechanics. Elsevier, North-Holland (1989).

[39] M. Bengisu, O.T. Inal. Whisker toughening of ceramics – toughening mechanisms, fabrication, and composites properties. *Annu Rev Mater Sci* 24, 83-124 (1994).

[40] R.K. Nalla, J.H. Kinney, R.O. Ritchie. Effect of orientation on the in vitro fracture toughness of dentin: the role of toughening mechanisms. *Biomaterials* 24(22), 3955-3968 (2003), https://doi.org/10.1016/S0142-9612(03)00278-3.

[41] J.W. Hutchinson. Crack tip shielding by microcracking in brittle solids. *Acta Metall* 35, (1987), 1605-1619, https://doi.org/10.1016/0001-6160(87)90108-8.

[42] F.F. Lange. Interaction of a crack front with a second-phase dispersion. *Philos Mag* 22, (1970), 983-992, https://doi.org/10.1080/14786437008221068.

[43] J.P. Pascault. Yielding and fracture of toughened networks. In: J.P. Pascault, H. Sautereau, J. Verdu, R.J.J Williams (eds) Thermosetting polymers. Marcel Dekker Incorporated, New York, (2002), 389–408, ISBN 978-1-4899-0398-3.

[44] K.T. Faber, A.G. Evans. Crack deflection processes. 1. Theory. *Acta Metall.* 31, (1983), 565-576.

[45] R.W. Cahn, P. Haasen, E.J. Kramer. Materials science and technology: A comprehensive Treatment – Vol. 13. Structure and properties of composites. VCH, Weinheim (1993), ISBN 3-527-26826-X.

[46] H.L. Cox. The elasticity and strength of paper and other fibrous materials. *Br J Appl Phys* 3 (3), 72-79 (1952), DOI: 10.1088/0508-3443/3/3/302.

[47] B. Turcsanyi, B. Pukanszky, F. Tudos. Composition dependence of tensile yield stress in filled polymers. *J Mater Sci Lett* 7, 160–2 (1988).

[48] J. Liang. Reinforcement and quantitative description of inorganic particulate-filled polymer composites. *Compos Part B-Eng* 51, 224-232 (2013), https://doi.org/10.1016/j.compositesb.2013.03.019.

[49] R. Hill. Elastic properties of reinforced solids: Some theoretical principles. *J Mech Phys Solids* 11, 357-372 (1963), https://doi.org/10.1016/0022-5096(63)90036-X.

[50] Z. Hashin, S. Shtrikman. A variational approach to the theory of the elastic behavior of multiphase materials. *J Mech Phys Solids* 11, 127-140 (1963), https://doi.org/10.1016/0022-5096(63)90060-7.

[51] W. Voigt. Ueber die Beziehung zwischen den beiden Elasticitätsconstanten isotroper Körper. *Ann Phys* 274, 573-587 (1889), https://doi.org/10.1002/andp.18892741206.

[52] A. Reuss. Berechnung der Fließgrenze von Mischkristallen auf Grund der Plastizitätsbedingung für Einkristalle. Zamm-Z *Angew Math Me* 9, 49-58 (1929), https://doi.org/10.1002/zamm.19290090104.

[53] E. Guth. Theory of filler reinforcement. *J Appl Phys* 16, 20-25 (1945), https://doi.org/10.1063/1.1707495.

[54] A. Einstein. Eine neue Bestimmung der Moleküldimensionen. *Ann Phys* 19, 289-306 (1906), https://doi.org/10.1002/andp.19063240204.

[55] B. Paul. Prediction of constants of multiphase materials. *Trans Am Inst Min Metall Pet Eng* 218, 36-41 (1960).

[56] O. Ishai, I.J. Cohen. Elastic properties of filled and porous epoxy composites. *Int J Mech Sci* 9, 539-546 (1967), https://doi.org/10.1016/0020-7403(67)90053-7.

[57] T.J. Hirsch. Modulus of elasticity of concrete affected by elastic moduli of cement paste matrix and aggregate. *Amer Conc I* 59, 427-452 (1962).

[58] M. Takayanagi, S. Uemura, S. Minami. Application of equivalent model method to dynamic rheo-optical properties of crystalline polymer. *J Polym Sci Pol Sym* 5, 113-122 (1964), https://doi.org/10.1002/polc.5070050111.

[59] U.J. Counto. The effect of the elastic modulus of the aggregate on the elastic modulus, creep and creep recovery of concrete. *Mag Concrete Res* 16, 129-138 (1964), https://doi.org/10.1680/macr.1964.16.48.129.

[60] J.C. Halpin, S.W. Tsai. Effects of 95esa95ior95ntal factors on composite materials. Technical Report. AFML-TR 67 – 423 (1969).

[61] J.J. Hermans. The elastic properties of fiber reinforced materials when the fibers are aligned. Proceedings of the Koninklijke Nederlandse Akademie van Wetenschnappen; Amsterdam; Series B; Vol. 70; No. 1 1 – 9 (1967).

[62] R. Hill. Theory of mechanical properties of fibre – strengthened materials – III. Self – Consistent Model. *J Mech Phys Solids* 13, 189 – 198 (1965), https://doi.org/10.1016/0022-5096(65)90008-6.

[63] L.E. Nielsen. Generalized equation for the elastic moduli of composite materials. *J Appl Phys* 41, 1626–1627 (1970), https://doi.org/10.1063/1.1658506.

[64] T.B. Lewis, L. E. Nielsen. Dynamic mechanical properties of particulate filled composites. *J Appl Polym Sci* 14, 1449-1471 (1970), https://doi.org/10.1002/app.1970.070140604.

[65] L.E. Nielsen. Dynamic mechanical properties of polymers filled with agglomerated particles. *J Appl Polym Sci* 17, 1897–1901 (1979), https://doi.org/10.1002/pol.1979.180171106.

[66] E.H. Kerner. The elastic and thermo-elastic properties of composite media. *Proc Phys Soc B* 69, 808-813 (1956), http://dx.doi.org/10.1088/0370-1301/69/8/305.

[67] A. Dorigato, Y. Dzenis, A. Pegoretti. Filler aggregation as a reinforcement mechanism in polymer nanocomposites. *Mech Mater* 61, 79 – 90 (2013), https://doi.org/10.1016/j.mechmat.2013.02.004.

[68] X.L. Ji, J.K. Jing, W. Jiang, B.Z. Jiang. Tensile modulus of polymer nanocomposites. *Polym Eng Sci* 42, 983 – 993 (2002), https://doi.org/10.1002/pen.11007.

[69] S.Y. Fu, X.Q. Feng, B. Lauke, Y.W. Mai. Effects of particle size, particle/matrix interface adhesion and particle loading on mechanical properties of particulate-polymer composites. *Compos. Part B-Eng* 39, 933–961 (2008), https://doi.org/10.1016/j.compositesb.2008.01.002.

[70] W.N. Findley, J.S. Lai, K. Onaran. Creep and relaxation of nonlinear viscoelastic materials. Dover Publication, Inc.: New York, NY, USA (1989).

[71] B. Ediger. Einfluss der Teilchengeometrie auf das Verhalten von Verbundwerkstoffen mit Nicht-Linear-Viskoelastischen Eigenschaften, Dargestellt am Beispiel Gefüllten und Verstärkten Polypropylens. Ph.D. Thesis, Universität Stuttgart, Stuttgart, Germany (1986).

[72] J.D. Ferry. Viscoelastic properties of polymers. John Wiley & Sons: New York, NY, USA (1980), ISBN 9780444601926.

[73] H. Altenbach. Classical and non-classical creep models. In Creep and Damage in Materials and Structures. International Centre for Mechanical Sciences; Altenbach, H., Skrzypek, J.J., Eds.; Springer: Vienna, Austria (1999), Volume 399, ISBN 978-3-211-83321-6, https://doi.org/10.1007/978-3-7091-2506-9_2.

[74] L.C. Cessna. Stress-time superposition of creep data for polypropylene and coupled glass-reinforced polypropylene. *Polym Eng Sci* 11, 211–219 (1971), https://doi.org/10.1002/pen.760110308.

[75] J.A. Gonilha, J.R. Correia, F.A. Branco. Creep response of GFRP–concrete hybrid structures: Application to a footbridge prototype. *Compos. Part B-*

Eng 53, 193–206 (2013), https://doi.org/10.1016/j.compositesb.2013.04.054.

[76] P. Georgiopoulos, E. Kontou, A. Christopoulos. Short-term creep behavior of a biodegradable polymer reinforced with wood-fibers. *Compos. Part B-Eng* 80, 134–144 (2015), https://doi.org/10.1016/j.compositesb.2015.05.046.

[77] M. Eftekhari, A. Fatemi. Creep behavior and modeling of neat, talc-filled, and short glass fiber reinforced thermoplastics. *Compos. Part B-Eng* 97, 68–93 (2016), https://doi.org/10.1016/j.compositesb.2016.04.043.

[78] M.R.M. Asyraf, M.R. Ishak, S.M. Sapuan, N. Yidris. Comparison of static and long-term creep behaviors between balau wood and glass fiber reinforced polymer composite for cross-arm application. *Fibers Polym* 22, 793–803 (2021), https://doi.org/10.1007/s12221-021-0512-1.

[79] D.N. Robinson, W.K. Binienda, M.B. Ruggles. Creep of polymer matrix composites. I: Norton/Bailey creep law for transverse isotropy. *J Eng Mech-ASCE* 129, 310–317 (2003), https://doi.org/10.1061/(ASCE)0733-9399(2003)129:3(310).

[80] R. Buchdahl, L.E. Nielsen. The application of Nutting´s equation to the viscoelastic behavior of certain polymeric systems. *J Appl Phys* 22, 1344 (1951), https://doi.org/10.1063/1.1699864.

[81] J. Simsiriwong, R.W. Sullivan, H.H. Hilton. Viscoelastic creep compliance using prony series and spectrum function approach. In Challenges in Mechanics of Time-Dependent Materials and Processes in Conventional and Multifunctional Materials; B. Antoun, H. Qi, R. Hall, G. Tandon, H. Lu, C. Lu (eds.). Conference Proceedings of the Society for Experimental Mechanics Series; Springer: New York, NY, USA (2013) Volume 2. https://doi.org/10.1007/978-1-4614-4241-7_21.

[82] Z. Wang, D.E. Smith. Numerical analysis on viscoelastic creep responses of aligned short fiber reinforced composites. *Compos Struct* 229, 111394 (2019), ISSN 0263-8223, https://doi.org/10.1016/j.compstruct.2019.111394.

[83] M.V. Pathan, V.L. Tagarielli, S. Patsias. Numerical predictions of the anisotropic viscoelastic response of uni-directional fibre composites. *Compos Part A-Appl S* 93, 18-32 (2017), ISSN 1359-835X, https://doi.org/10.1016/j.compositesa.2016.10.029.

[84] A.A. Gusev. Finite element estimates of viscoelastic stiffness of short glass fiber reinforced composites, *Compos Struct* 171, 53-62 (2017), ISSN 0263-8223, https://doi.org/10.1016/j.compstruct.2017.03.021.

[85] T. Mori, K. Tanaka. Average stress in matrix and average elastic energy of materials with misfitting inclusions. *Acta Metall Mater* 21, 5, 571-574 (1973), ISSN 0001-6160, https://doi.org/10.1016/0001-6160(73)90064-3.

[86] G. Lielens. Micro-macro modeling of structured materials. Université Catholique de Louvain, Belgium, 1999.

[87] R. Ansari, M.K. Hassanzadeh-Aghdam. Micromechanical investigation of creep-recovery behavior of carbon nanotube-reinforced polymer nanocomposites. *Int J Mech Sci* 115–116, 45-55 (2016), ISSN 0020-7403, https://doi.org/10.1016/j.ijmecsci.2016.06.005.

[88] T. Tang, S.D. Felicelli. Computational evaluation of effective stress relaxation behavior of polymer composites. *Int J Eng Sci* 90, 76-85 (2015), ISSN 0020-7225, https://doi.org/10.1016/j.ijengsci.2015.02.003.

[89] B. Möginger, U. Fritz. Viskoelastische Spannungs-Dehnungs-Beziehung thermoplastischer Polymere: Herleitung und experimentelle Überprüfung. Kautschuk und Gummi Kunststoffe 47 (4), 256–261 (1994).

[90] W. Grellmann, S. Seidler. Polymer testing (2nd edition). Hanser Verlag, München (2013), ISBN 978-1-56990-548-7.

[91] S. Mortazavian, A. Fatemi, Effects of fiber orientation and anisotropy on tensile strength and elastic modulus of short fiber reinforced polymer composites. *Compos Part B-Eng* 72, 116-129 (2015), ISSN 1359-8368, https://doi.org/10.1016/j.compositesb.2014.11.041.

[92] M. De Monte, E. Moosbrugger, M. Quaresimin. Influence of temperature and thickness on the off-axis 98esa98ior of short glass fibre reinforced polyamide 6.6-Quasi-static loading. *Compos Part A.Appl S* 41(7), 859–71 (2010).

[93] Y. Zhou, P.K. Mallick. A non-linear damage model for the tensile behavior of an ©njection molded short E-glass fiber reinforced polyamide-6,6. *Mater Sci Eng A* 393 (1), 303–9 (2005).

[94] Z. Wang, Y. Zhou, P.K. Mallick. Effects of temperature and strain rate on the tensile behavior of short fiber reinforced polyamide-6. *Polym Compos* 23 (5), 858–71 (2002).

[95] E. Hnátková, Z. Dvorak. Effect of the skin-core morphology on the mechanical properties of injection-moulded parts. *Materiali in tehnologije* 50, 195-198 (2016), 10.17222/mit.2014.151.

[96] H.S. Katz. Solid spherical fillers. In *Handbook of Fillers for Plastics*, H. S. Katz and J. V. Milewski, Eds., Van Nostrand Reinhold, New York, 429 (1987), ISBN 978-0-442-26024-8.

[97] J.I. Weon, H.J. Sue. Effects of clay orientation and aspect ratio on mechanical behavior of nylon-6 nanocomposite. *Polymer* 46 (17), 6325-6334 (2005), ISSN 0032-3861, https://doi.org/10.1016/j.polymer.2005.05.094.

[98] C. Dessi, G.D. Tsibidis, D. Vlassopoulos, M. De Corato, M. Trofa, G. D'Avino, P.L. Maffettone, S. Coppola. Analysis of dynamic mechanical response in torsion. *J Rheol* 1, 60 (2), 275–287 (2016), https://doi.org/10.1122/1.4941603.

[99] A.J.C.B. Saint-Venant. Mémoire sur la torsion des prismes. Mémoires présentés par divers savants à l´Académie de Sci. 14, 233-560 (1856).

[100] S. Huayamares, D. Grund, I. Taha. Comparison between 3-point bending and torsion methods for determining the viscoelastic properties of fiber-reinforced epoxy. *Polym Test* 85, 106428 (2020), https://doi.org/10.1016/j.polymertesting.2020.106428.

[101] A. Serra-Aguila, J.M. Puigoriol-Forcada, G. Reyes, J. Menacho. Estimation of tensile modulus of a thermoplastic material from dynamic mechanical analysis: Application to polyamide 66. *Polymers* 14, 1210 (2022), https://doi.org/10.3390/polym14061210.

[102] H. Junaedi, M. Baig, A. Dawood, E. Albahkali, A. Almajid. Mechanical and physical properties of short carbon fiber and nanofiller-reinforced polypropylene hybrid nanocomposites. *Polymers* 12, 2851 (2020), https://doi.org/10.3390/polym12122851.

[103] G. Roebben, B. Bollen, A. Brebels, J. Van Humbeeck, O. Van der Biest. Impulse excitation apparatus to measure resonant frequencies, elastic moduli, and internal friction at room and high temperature. *Rev Sci Instrum* 68, 4511 (1997), https://doi.org/10.1063/1.1148422.

[104] B.A. Latella, S.R. Humphries. Young´s modulus of a 2.25Cr-1Mo steel at elevated temperature. *Scripta Mater* 51, 635-639 (2004), https://doi.org/10.1016/j.scriptamat.2004.06.028.

[105] A. Hauert, A. Rossoll, A. Mortensen. Young´s modulus of ceramic particle reinforced aluminium: Measurement by the impulse excitation technique and confrontation with analytical models. *Compos Part A-Appl S* 40, 524-529 (2009), https://doi.org/10.1016/j.compositesa.2009.02.001.

[106] M. Dal Bó, V. Cantavella, E. Sanchéz, F.A. Gilabert, A.O. Boschi, D. Hotza. An estimate of quartz content and particle size in porcelain tiles from young´s modulus measurements. *Ceram Int* 43, 2233-2238 (2017), https://doi.org/10.1016/j.ceramint.2016.10.204.

[107] ASTM E1876-22. 2021. Standard test method for dynamic Young´s modulus, shear modulus, and Poisson´s ration by impulse excitation technique. ASTM International.

[108] A. J. Nuñez, N. E. Marcovich, M. I. Aranguren. Analysis of the creep behavior of polypropylene-woodflour composites. *Polym Eng Sci* 44, 1594-1603 (2004), https://doi.org/10.1002/pen.20157.

[109] M.A. Hidalgo-Salazar, J.H. Mina, P.J. Herrera-Franco. The effect of interfacial adhesion on the creep 100esa100ior of LDPE–Al–Fique composite materials. *Compos Part B- Eng* 55, 345-351 (2013), ISSN 1359-8368, https://doi.org/10.1016/j.compositesb.2013.06.032.

[110] B.A. Acha, M.M. Reboredo, N.E. Marcovich. Creep and dynamic mechanical behavior of PP–jute composites: Effect of the interfacial adhesion. *Compos Part A-Appl S* 38 (6), 1507-1516 (2007), ISSN 1359-835X, https://doi.org/10.1016/j.compositesa.2007.01.003.

[111] H. Sokairge, F. Elgabbas, A. Rashad, H. Elshafie. Long-term creep behavior of basalt fiber reinforced polymer bars. *Constr Build Mater* 260, 120437 (2020), ISSN 0950-0618, https://doi.org/10.1016/j.conbuildmat.2020.120437.

[112] X. Hao, H. Zhou, B. Mu, L. Chen, Q. Guo, X. Yi, L. Sun, Q. Wang, R. Ou. Effects of fiber geometry and orientation distribution on the anisotropy of mechanical properties, creep behavior, and thermal expansion of natural fiber/HDPE composites. *Compos Part B-Eng* 185, 107778 (2020), ISSN 1359-8368, https://doi.org/10.1016/j.compositesb.2020.107778.

[113] J. Jose, K. Malhotra, S. Thomas, K. Joseph, G. Koichi, M.S. Sreekala. State of the art, new challenges, and opportunities. In Polymer Composites, Macro- and Microcomposites; T. Sabu, J. Kuruvilla, S. K Malhotra, G. Koichi, M. S. Sreekala, (eds) Wiley-VCH: Weinhein, Germany (2012); Volume 1, ISBN 9783527326242.

[114] https://www.kruss-scientific.com/en/know-how/glossary/youngs-equation date of access: 21.05.2024.

[115] A. Kopczynska, G.W. Ehrenstein. Oberflächenspannung von Kunststoffen. Messmethoden am LKT. Sonderdrucke am Lehrstuhl für Kunststofftechnik, Friedrich-Alexander-Universitat Erlangen-Nürnberg, https:// www. Lkt.tf.fau.de/files/2017/06/Oberflächenspannung.pdf (2017).

[116] G. Erhard. Konstruieren mit Kunststoffen. 4. Auflage, 152–153, Carl Hanser Verlag, (2008), ISBN 978-3-445-41646-8.

[117] A. Ansafirar, G.W. Crichtlow, R. Guo, R.J. Ellis. Assessing effect of the migration of a paraffin wax on the surface free energy of natural rubber.

Rubber Chem Technol 82, 113–120 (2009), https:// doi. Org/ 10. 5254/1. 35570 01.

[118] B. Sansao, J.J. Kellar, W.M. Cross, K. Schottler, A. Romkes, Comparison of surface energy and adhesion energy of surface-treated particles. *Powder Technol* 384, 267-275 (2021), ISSN 0032-5910, https://doi.org/10.1016/j.powtec.2021.02.029.

[119] N. Ismail, M.B. de Rooij, D.J. Shipper, N.H.M Zini. Determination of surface energy of aramid fibre. In: M. F. B. Abdollah, H. Amiruddin, A. S. Phuman Singh, F. Abdul Munir, A. Ibrahim (eds) Proceedings of the 7th International Conference and Exhibition on Sustainable Energy and Advanced Materials, Melaka, Malaysia. ICE-SEAM (2021). Lecture Notes in Mechanical Engineering. Springer, Singapore. https://doi.org/10.1007/978-981-19-3179-6_77 (2022).

[120] E. Papirer, S. Li, H. Balard, J. Jagiello. Surface energy and adsorption energy distribution measurements on some carbon blacks. *Carbon* 29, 1135-1143 (1991), 10.1016/0008-6223(91)90031-D.

[121] A. Ari, A. Bayram, M. Karaha, S. Karagöz. Comparison of the mechanical properties of chopped glass, carbon, and aramid fiber reinforced polypropylene. *Polymers and Polymer Composites* 30, (2022), doi:10.1177/09673911221098570.

[122] Application note Oxford Instruments Asylum Research Inc. Characterization of the interfacial layer in polymer-based composites using AFM. Date of access: 22.01.2024, https://afm.oxinst.com/assets/uploads/Asylum%20Research/App%20Notes/Characterization_of_Polymer_Composite_Using_AFM-19NOV2021[1].pdf

[123] S. Vecchiato, J. Ahrens, A. Pellis, D. Scaini, B. Mueller, E. Herrero Acero, G. M. Guebitz. Enzymatic functionalization of HMLS-polyethylene terephthalate fabrics improves the adhesion to rubber. ACS Sustainable Chemistry & Engineering, 5(8), 6456-6465 (2017).

[124] J. Jiang, C. Xu, Y. Su, Q. Guo, F. Liu, C. Deng, X. Yao, L. Zhou. Influence of Carbon Nanotube Coatings on Carbon Fiber by Ultrasonically Assisted Electrophoretic Deposition on Its Composite Interfacial Property. *Polymers* 8, 302 (2016), https://doi.org/10.3390/polym8080302.

[125] J. Steinhaus. Schadenanalyse und Bauteilprüfung an Kunststoffen. DGM seminar at University of Applied Sciences, Rheinbach (2022).

[126] J. Thomason, J. Rudeiros-Fernández. Characterization of interfacial strength in natural fibre – polyolefin composites at different temperatures.

Composite Interfaces 29, 1-22 (2021). DOI: 10.1080/09276440.2021.1913901.

[127] S. Zhandarov, E. Mäder. Determining the interfacial toughness from force–displacement curves in the pull-out and microbond tests using the alternative method. *Int J Adhes* 65, 11-18 (2016), ISSN 0143-7496, https://doi.org/10.1016/j.ijadhadh.2015.10.020.

[128] T. Pardoen, N. Klavzer, S. Gayot, F. Van Loock, J. Chevalier, X. Morelle, V. Destoop, F. Lani, P. Camanho, L. Brassart, B. Nysten, C. Bailly. Nanomechanics serving polymer-based composite research. *C R Phys* 22, 331-352 (2021), doi: 10.5802/crphys.56, https://comptes-rendus.academie-sciences.fr/physique/articles/10.5802/crphys.56/.

[129] M. Lohrmann. Zweidimensionale Ermittlung der Änderung des mechanischen Verhaltens von gefüllten Elastomeren bei Variation der Füllstoffart. *Fraunhofer-Institut für Chemische Technologie ICT* (1996).

[130] D.Y. Chimeni, E. Vallée, L. Sorellis, D. Rodrigue. Effect of glass bead size and content on the thermomechanical properties of polyethylene composites. *Poly Eng Sci* 58, 1826-1836 (2018), https://doi.org/10.1002/pen.24788.

[131] O. Balkan, H. Demirer. Mechanical properties of glass bead- and wollastonite-filled isotactic-polypropylene composites modified with thermoplastic elastomers. *Polym Compos* 31, 1285-1308 (2010), https://doi.org/10.1002/pc.20953.

[132] H.C. Ludwig. Push pull processing – a new processing technique to optimize materials properties of reinforced and neat thermoplastics (in German), thesis Uni Stuttgart, 1998.

[133] M. Doumeng, F. Berthet, K. Delbé, O. Marsan, J. Denape, F. Chabert. Effect of size, concentration, and nature of fillers on crystallinity, thermal, and mechanical properties of polyetheretherketone composites. *J Appl Polym Sci* 139(5), e51574 (2022), https://doi.org/10.1002/app.51574.

[134] B. Wunderlich. Advanced thermal analysis laboratory (ATHAS), Bept. Chem. University Tennessee, Knoxville, TN 37996-1600, USA 38

[135] B. Möginger. Einfluss der Verarbeitung auf Morphologie und Deformationsverhalten von Polybutylen-Terephthalat (PBT)—Appendix B. Ph.D. Thesis, University of Stuttgart, Stuttgart, Germany, 1993.

[136] Y. Furshima, S. Kumazawa, H. Umetsu, A. Toda, E. Zhuravlev, A. Wurm, C. Schick. Crystallization kinetics of poly(butylene terephthalate) and its talc composites. *J Appl Polym Sci* 134(16), 44739 (1-11) (2017), https://doi.org/10.1002/app.44739.

[137] A.M. Rhoades, J.L. Williams, R. Androsch. Crystallization kinetics of polyamide 66 at processing-relevant cooling conditions and high supercooling. *Thermochimica Acta* 603, 103–109 (2015), doi:10.1016/j.tca.2014.10.020.

[138] E. Ramakers-van Dorp, B. Eger, C. Raschen, M. Urbanek, B Möginger, B. Hausnerova. Local process-dependent structural and mechanical properties of extrusion blow molded high-density polyethylene hollow parts. *Polym Test* 82, 106314 (2020), https://doi.org/10.1016/j.polymertesting.2019.106314.

[139] J. Rech, E. Ramakers-van Dorp, P. Michels, B. Möginger, B. Hausnerova. Introduction of an adhesion factor to *cube in cube* models and its effect on calculated moduli of particulate composites. *Sci Rep* 12, 16225 (2022), https://doi.org/10.1038/s41598-022-20629-2.

[140] M.A. Kashfipour, N. Mehra, J. Zhu. A review on the role of interface in mechanical, thermal, and electrical properties of polymer composites. *Adv. Compos. Hybrid Mater.* **1**, 415–439 (2018), https:// doi. Org/ 10. 1007/ s42114- 018- 0022-9.

[141] K. Wang, J. Wu, L. Ye, H. Zeng. Mechanical properties and toughening mechanisms of polypropylene/barium sulfate composites. Compos. Part A-Appl. Sci. Manuf. 34, 1199–1205 (2003), https:// doi. Org/ 10. 1016/j. compo sitesa. 2003. 07. 004.

[142] M. Bek, A. Aulova, K.P. Cresnar, S. Matkovič, M. Kalin, L.S. Perše. Long-term creep compliance of wood polymer composites: Using untreated wood fibers as a filler in recycled and neat polypropylene matrix. *Polymers* 14, 2539 (2022), https://doi.org/10.3390/polym14132539.

[143] H. Chandekar, S. Waigaonkar, V. Chaudhari. Effect of chemical treatment on creep-recovery behavior of jute-polypropylene composites. *J Mater Des Appl* 235, 329–340 (2020), https://doi.org/10.1177/1464420720963344.

[144] N.E. Marcovich, M.A. Villar. Thermal and mechanical characterization of linear low-density polyethylene/wood flour composites. *J Appl Polym Sci* 90, 2775–2784 (2003), https://doi.org/10.1002/app.12934.

[145] F.W. Preston. The mechanical properties of glass. *J Appl Phys* 13, 623 (1942), https://doi.org/10.1063/1.1714811.

[146] Y. Xu, Q. Wu, L. Young, F. Yao. Creep behavior of bagasse fiber reinforced polymer composites. *Bioresour Technol* 101, 3280–3286 (2010), https://doi.org/10.1016/j.biortech.2009.12.072.

[147] C.J. Perez, V.A. Alvarez, A. Vazquez. Creep behavior of layered silicate/starch-polycaprolactone blends nanocomposites. *Mater Sci Eng A-Struct* 480, 259–265 (2008), https://doi.org/10.1016/j.msea.2007.07.031.

[148] J. Yang, Z. Zhang, A.K. Schlarb, K. Friedrich. On the characterization of tensile creep resistance of polyamide 66 nanocomposites. Part II: Modeling and prediction of long-term performance. *Polymer* 47, 6745–6758 (2006), https://doi.org/10.1016/j.polymer.2006.07.060.

[149] B. Möginger, P. Eyerer. Determination of the weighting function $g(\beta_i, r, v_F)$ for fibre orientation analysis of short fibre-reinforced composites. *Composites* 22, 5 (1991).

[150] R.M. Jones. Mechanics of composite materials. Taylor & Francis Inc: London 1975, pp. 45-57, ISBN 12 978-0070327900.

List of figures

List of tables

Abbreviations

ABS	Acrylonitrile butadiene styrene
AFM	Atomic force microscopy
$BaTiO_3$	Barium titanate
$CaCO_3$	Calciumcarbonate
CF	Carbon fiber
CFRC	Continuous fiber reinforced composites
CMC	Ceramic matrix composites
CNT	Carbon nanotube
DMA	Dynamic mechanical analysis
FEA	Finite element analysis
FEM	Finite element method
FOD	Fiber orientation distribution
GB	Glass bead
GF	Glass fiber
HDPE	High-density polyethylene
HDT	Heat deflection temperature
IET	Impulse excitation technique
LCP	Liquid crystalline polymer
MMC	Metal matrix composites
OT	Oscillatory torsion
PA6	Polyamide 6
PA66	Polyamide 66
PA11	Polyamide 11
PA12	Polyamide 12
PAEK	Polyaryletherketone
PAI	Polyamide-imide
PAR	Polyarylate
PARA	Polyarylamide
PBI	Polybenzimidazole
PBT	Polybutylene terephthalate
PC	Polycarbonate
PE	Polyethylene
PEEK	Polyether ether ketone
PEI	Polyethyleneimine
PESU	Polyethersulfone
PET	Polyethylene terephthalate
PETG	Polyethylene terephthalate glycol
PEX	Cross-linked polyethylene
PI	Polyimide
PLA	Polylactide

PMC	Polymer matrix composites
PMMA	Poly(methyl methacrylate)
POM	Polyoxymethylene
PRC	Particle reinforced composites
PP	Polypropylene
PPA	Polyphthalamide
PPO	Poly(phenylene oxide)
PPS	Polyphenylene sulfide
PPSU	Polyphenylsulfone
PS	Polystyrene
PSU	Polysulfone
PVA	Polyvinyl acetate
PVC	Polyvinyl chloride
PVDC	Polyvinylidene chloride
PVDF	Poly(vinylidene fluoride)
RIM	Reaction injection molding
RRIM	Reinforced reaction injection molding
RVE	Representative volume element
SAN	Styrene-acrylonitrile copolymer
SEM	Scanning electron microscopy
SGFRC	Short glass fiber reinforced composites
SRP	Self-reinforced polymer
TCT	Tensile creep tests
TPE	Thermoplastic elastomer
TPI	Thermoplastic polyimide
TT	Tensile test
UHMWPE	Ultra-high-molecular-weight polyethylene
VSSF	Viscoelastic stress-strain-function
3PB	Three-point bending

Symbols

A	Bailey-Norton coefficient
a	Distance neighboring inclusion
A_F	Fiber cross-section
B'	Fractional free volume
D	Diameter of inclusion
d	Normalized inclusion distance
d_p	Particle diameter
dK_c	Dilatational contribution after micro-cracking
E_0	Initial modulus
E'	Storage modulus
E''	Loss modulus
E^*	Complex modulus
E^*	Particle stiffness
$E(t)$	Creep modulus
E_C	Composite modulus
E_F	Filler modulus
E_f	Flexural modulus
E_l	Longitudinal modulus
E_M	Matrix modulus
f_1, f_2, f_3	Orientation factors
F_0	Initial force
G_0	Initial shear modulus
G′	Storage shear modulus
G′′	Loss shear modulus
G^*	Complex shear modulus
G^*	Shear modulus after micro-cracking
g_J	Shear correction factor
G_J	Effective shear correction factor
G_M	Matrix shear modulus
h	height
$J(t, \sigma_0)$	Creep compliance
J_t	Moment of inertia
k	Geometry factor
k_1, k_2, k_3	Constants depending on the shape and size of the micro-cracking zone

k_{adh}	Filler matrix adhesion
K_C	Fracture toughness of composite
K_E	Einstein coefficient
K_0	Initial fracture toughness
K_M	Fracture toughness of matrix
l	length
m	Mass
M	Torque
n	Fitting exponents
Q	Line energy per unit crack front
r	Aspect ratio
R_2	Correlation coefficient
t	Thickness
$T_{ambient}$	Ambient temperature
T_G	Glass transition temperature
v_F	Filler volume content
w_F	Filler weight content
X_C	Degree of crystallinity

Greek symbols

Γ_t	Tearing energy of the particle
δ	Phase angle
$\tan \delta$	Loss factor
ε_0	Initial strain
ε^+	Transient strain
ε_C	Strain (composite part)
$\varepsilon_{C,F}$	Strain (filler of composite part)
$\varepsilon_{C,M}$	Strain (matrix of composite part)
ε_{EV}	Strain (elementary volume)
ε_M	Strain (matrix part)
ε_R	Relaxation strain
η	Viscosity
θ	Angular displacement, contact angle, misalignment angle, inclination angle
θ_T	Dilatational strain
μ	Poisson´s ratio
μ^*	Poisson´s ratio after microcracking
ξ	Deformation twist in oscillatory torsion
ξ	Geometry factor (Halpin-Tsai)
σ_0	Initial stress
σ_b	Strain at break
$\sigma_F(z)$	Fiber axial stress
σ^{lv}	liquid surface tension
σ^{sl}	solid/liquid interfacial tension
σ^{sv}	solid surface free energy
σ_y	Yield stress
$\sigma_{y,C}$	Yield strength composite
$\sigma_{y,M}$	Yield strength matrix
T	Relaxation time
$\tau_i(z)$	Shear stress at the interface
ϕ	Plane angle
Φ	Correction factor of crack bowing
χ	Stress transfer parameter
ω	Angular frequency

Publications, Posters and Presentations

Publications in a context of this doctoral work:

- Julian Rech, Esther Ramakers-van Dorp, Patrick Michels, Bernhard Möginger, Berenika Hausnerová, **Introduction of an adhesion factor to *cube in cube* models and its effect on calculated moduli of particulate composites**. *Sci Rep* **12**, 16225 (2022). https://doi.org/10.1038/s41598-022-20629-2.
- Julian Rech, Esther Ramakers-van Dorp, Bernhard Möginger, Berenika Hausnerová, **Modeling of Creep Behavior of Particulate Composites with Focus on Interfacial Adhesion Effect**. *Int J Mol Sci* **2022**, *23*, 14120. https://doi.org/10.3390/ijms232214120.
- Julian Rech, Christian Dresbach, Esther Ramakers-van Dorp, Bernhard Möginger, Berenika Hausnerová, **Towards Reliable Mechanical Characterization of Composites for Structural Applications**. Submitted to *Journal of Engineering Mechanics*, June 2025.
- Julian Rech, Bernhard Möginger, Hans-Christian Ludwig, Berenika Hausnerová, **Prediction of Creep Behavior in Short Fiber Reinforced Polymer Matrix Composites using an Elementary Volume Approach**. Submitted to *Mechanics of Time-Dependent Materials*, April 2025.

Conference Publications:

- **Viscoelastic modeling of stress-strain-behavior of two-phase model materials,** *Nordic Rheology Conference,* Gothenburg, Sweden 2019, poster presentation.
- **Elementary Volume Concept – a new modeling approach to calculate the elastic moduli of spherical composites systems introducing the interfacial adhesion**, *Times of Polymer and Composites*, Ischia, Italy 2021, oral presentation.
- **Quantitative determination of adhesion factors by modeling Young´s moduli of glass bead reinforced thermoplastics**, *27th Polish-Slovak Scientific Conference on: Machine Modelling and Simulations*, Rydzyna, Poland 2022, oral presentation.
- **Comparison of Young´s moduli determined by impulse excitation technique (IET), dynamic mechanical analysis (DMA) and tensile test (TT),** *20th ICEM International Conference on Experimental Mechanics*, Porto, Portugal 2023, oral presentation.

Curriculum Vitae

Date and place of birth July 23rd, 1991 in Neuwied, Germany

Permanent address University of Applied Sciences Bonn-Rhein-Sieg

Von-Liebig-Str. 20

D-53359 Rheinbach, Germany

Tel.: (+49) 2241 865 766

E-Mail: julian.rech@h-brs.de

Education

since 08/2020 **Ph.D. studies at Tomas Bata University in Zlín,**

University Institute, Nanotechnology and Advanced Materials

10/2015 – 11/2017 **M.Sc. Applied Polymer Sciences, FH Aachen – University of Applied Sciences,**

Department of Chemistry and Biotechnology

08/2012 – 09/2015 **B.Sc. Chemistry and material sciences, University of Applied Sciences Bonn-Rhein-Sieg,**

Department of Natural Sciences

Work experience

since 01/2018 **Scientific assistant at University of Applied Sciences Bonn-Rhein-Sieg, Rheinbach,**

Faculty of Applied Sciences

since 01/2018 **Project manager for industrial services in the field of thermal, microscopical and mechanical analysis,**

Faculty of Applied Sciences

since 08/2024 **Permanent research assistant as technical laboratory manager at University of Applied Sciences, Rheinbach,**

Faculty of Applied Sciences, Research Group Materials Science

Appendix A

Modulus determination of an EV with a spherical inclusion

A two phase composites consisting of a matrix M and a spherical disperse phase F is modeled by a cube containing a single particle in its center, the elementary volume (EV). This allows for generating large bodies of such composites by 3D arrangement of the EV and affirms complete space filling. Furthermore, the EV can be considered as a representative of such a composite with respect to macroscopic properties and behavior if separated in an appropriate manner, Fig. A1.

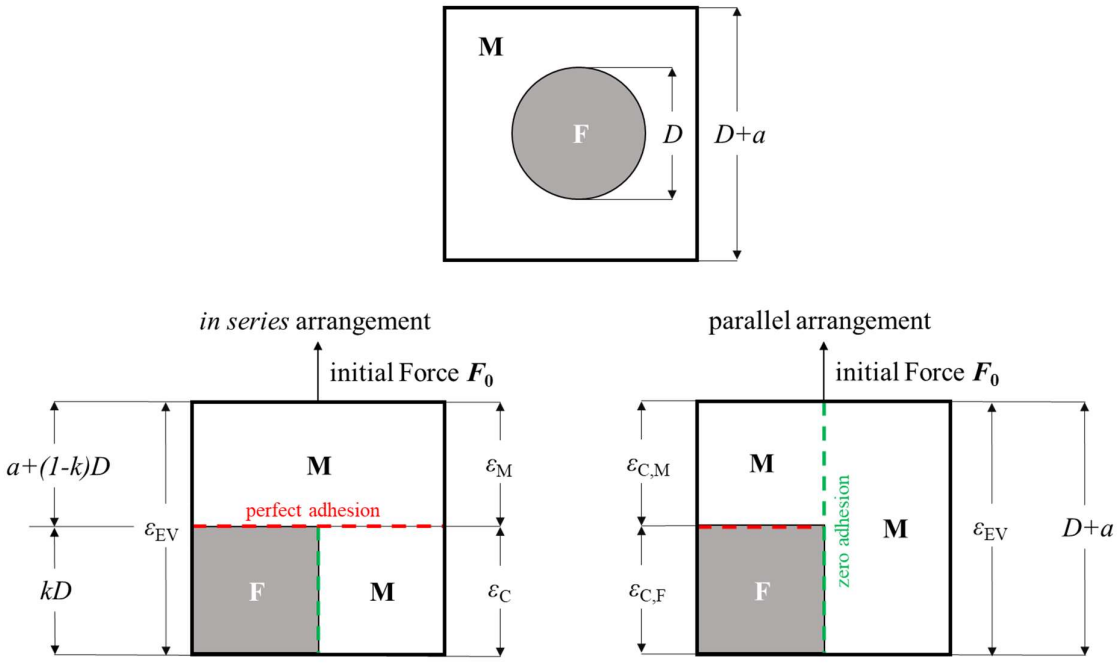

Fig. A1 Cubic elementary volume containing a spherical inclusion (top), and its „cube in cube" representation with in series and parallel arrangement.

The main differences between *in series* and *parallel* arrangement are the acting of the interfacial adhesion and the number of occurring strains:

- In the *in series* arrangement, perfect adhesion is assumed over the whole cross-section of the EV given by $(D + a)^2$ between matrix part and composites part perpendicular to the load direction, zero adhesion may occur between disperse phase and matrix of the composites part along the load direction, and the two strains ε_M and ε_F occur within the EV.
  $\Rightarrow$ upper bound
- In the *parallel* arrangement, perfect adhesion is assumed only over the cross-section of the composites part $(k\ D)^2$ between disperse phase and matrix perpendicular to the load direction, zero adhesion is required between composites part and matrix part along the load direction, and the

three strains $\varepsilon_{\mathrm{EV}}$, ε_{M} and ε_{F} occur within the EV.

$\Rightarrow$ lower bound

Case 1: *in series* arrangement

One requires three stress strain relations to derive the stiffness relation of the EV.

Stress strain relation of the EV (represents the macroscopic quantities)

$$\sigma = \sigma_{\mathrm{EV}} = E_{\mathrm{EV}} \frac{\Delta(D+a)}{D+a} = E_{\mathrm{EV}}\, \varepsilon_{\mathrm{EV}} \quad \Rightarrow \qquad \varepsilon_{\mathrm{EV}} = \frac{\sigma}{E_{\mathrm{EV}}} \tag{A1}$$

with external stress σ, stress acting on EV σ_{EV}, distance a between particles, modulus of EV E_{EV} and strain of EV $\varepsilon_{\mathrm{EV}}$. The second step is to define the stress-strain-relation of the matrix part with respect to the microscopic strain ε_{M} of the matrix part

$$\sigma = \sigma_{\mathrm{M}} = E_{\mathrm{M}} \frac{\Delta a}{a} = E_{\mathrm{M}}\, \varepsilon_{\mathrm{M}} \qquad \Rightarrow \qquad \varepsilon_{\mathrm{M}} = \frac{\sigma}{E_{\mathrm{M}}} \tag{A2}$$

with stress acting on matrix part σ_{M}, matrix modulus E_{M}, and matrix strain ε_{M}, and the stress-strain-relation of the composites part

$$\sigma = \sigma_{\mathrm{C}} = \sigma_{\mathrm{C,M}} + \sigma_{\mathrm{C,F}} \qquad \varepsilon_{\mathrm{C}} = \frac{\sigma}{E_{\mathrm{C}}} \tag{A3}$$

with stress acting composites part σ_C, stress acting on matrix of composites part $\sigma_{C,M}$, stress acting on filler of composites part $\sigma_{\mathrm{C,F}}$, strain of composites part ε_{C}, and the composites modulus E_{C}. The stress acting on the matrix of the composites part is given by

$$\sigma_{\mathrm{C,M}} = \left(1 - \frac{(k\,D)^2}{(D+a)^2}\right) E_{\mathrm{M}}\, \varepsilon_{\mathrm{C}} \tag{A4}$$

with the stress acting on the filler of the composites part

$$\sigma_{\mathrm{C,M}} = \frac{(k\,D)^2}{(D+a)^2}\, E_{\mathrm{F}}\, \varepsilon_{\mathrm{C}} \tag{A5}$$

with filler modulus E_{F}. The efficiency factor k takes into account that less than the maximum cross-section – for spheres it is $A_{\max} = \frac{\pi}{4} D^2$ – efficiently contributes to stress transfer. In order to determine the effective cross-section, the particle is converted to a cube having the same volume. The efficiency factor k of spheres is determined by the condition:

$V_{\mathrm{sphere}} = \frac{\pi}{6} D^3 = k^3 D^3 = V_{\mathrm{cube}}$ what leads to $k = \sqrt[3]{\frac{\pi}{6}} \cong 0.8058$

If the aspect ratio is not close to „1“ one has to distinguish the extremes „along the long axis“ and „perpendicular to the long axis“ e.g. with a square column consideration. Introduction of (A4) and (A5) in (A3) yields

$$\sigma = \left(\left(1 - \frac{(k\,D)^2}{(D+a)^2} \right) E_\mathrm{M}\, \varepsilon_\mathrm{C} + \frac{(k\,D)^2}{(D+a)^2}\, E_\mathrm{F} \right) \varepsilon_\mathrm{C} \tag{A6}$$

If the interfacial adhesion is not perfect, the amount of stress is reduced that can be transferred to the inclusion. This basically means that either modulus E_F or cross-section A_F are apparently reduced. This can be taken into account with the introduction of an adhesion factor k_adh in (A6). This can be done in two ways:

1. Reduction of the effective stiffness of the inclusion $\quad E_\mathrm{F} \;\rightarrow\; k_\mathrm{adh,E}\, E_\mathrm{F}$
2. Reduction of effective cross-section of the inclusion $\quad A_\mathrm{F} \;\rightarrow\; k_\mathrm{adh,A}\, A_\mathrm{F}$

However, the second way suggests that the adhesion factor does not act on the cross-section A_F but on the effective diameter $k\,D$ of the inclusion. Therefore, the adhesion factor is introduced quadratically as it is to reduce the edge length of the filler cube. In that respect the physical meaning of the adhesion factor is that it scales the edge length of the filler cube, and thus the available contact area of stress transfer between filler and matrix to account for reduced adhesion due to the surface energies of filler and matrix, respectively.

1. Reduction of the effective stiffness of the inclusion $\quad E_\mathrm{F} \;\rightarrow\; k_\mathrm{adh}^2\, E_\mathrm{F}$
2. Reduction of effective cross-section of the inclusion $\quad A_\mathrm{F} \;\rightarrow\; k_\mathrm{adh}^2\, A_\mathrm{F}$

This leads to

$$\sigma \underbrace{=}_{d=\frac{a}{D}} \left(\left(1 - \frac{k^2}{(1+d)^2} \right) E_\mathrm{M} \;+\; k_\mathrm{adh}^2\, \frac{k^2}{(1+d)^2}\, E_\mathrm{F} \right) \varepsilon_\mathrm{C} \tag{A7}$$

For perfect interfacial adhesion the adhesion factor k_adh has to be „1“. Solving (A7) for ε_C yields the strain of the composites part.

$$\varepsilon_\mathrm{C} = \frac{\sigma}{E_M \left(1 + \frac{k^2}{(1+d)^2}\, \frac{k_{adh}^2\, E_F - E_M}{E_M} \right)} \tag{A8}$$

The “macroscopic” strain of the EV ε_EV has to depend on the microscopic strains of matrix part ε_M and composites part ε_C. It also has to be affected by the dimensions of the EV in relation to the inclusion. Thus, one starts with the definition of the strain of the EV with spherical inclusion and its transformation in the *cube in cube* representation

$$\varepsilon_\mathrm{EV} = \underbrace{\frac{\Delta(D+a)}{D+a}}_{\text{sphere in EV}} = \underbrace{\frac{\Delta(kD + (D-kD) + a)}{kD + (D-kD) + a}}_{\text{cube in EV}} = \frac{\Delta(kD) + \Delta(D-kD+a)}{kD + (D-kD) + a} \tag{A9}$$

After separation of the stress induced length change into the length changes of inclusion/cube and matrix one gets

$$\varepsilon_{\mathrm{EV}} = \frac{\Delta(kD)}{kD + (D-k\ \ ) + a} + \frac{\Delta(D-kD+a)}{kD + (D-kD) + a} = \frac{\frac{\Delta(kD)}{kD}}{\frac{kD + (D-kD) + a}{kD}} + \frac{\frac{\Delta(D-kD+a)}{(D-kD) + a}}{\frac{kD + (D-kD) + a}{(D-kD) + a}} \quad \text{(A10)}$$

Multiplying the first fraction with *kD* and the second fraction with *D-kD+a* allows for the introduction of the microscopic strains. After cancelation of *D* one gets

$$\varepsilon_{\mathrm{EV}} = \frac{\frac{\Delta k}{k}}{\frac{k + (1-k) + d}{k}} + \frac{\frac{\Delta(1-k+d)}{(1-k) + d}}{\frac{k + (1-k) + d}{(1-k) + d}} = \frac{\varepsilon_{\mathrm{C}}}{\frac{k + (1-k) + d}{k}} + \frac{\varepsilon_{\mathrm{M}}}{\frac{k + (1-k) + d}{(1-k) + d}} \quad \text{(A11)}$$

Rearranging leads

$$\varepsilon_{\mathrm{EV}}(\varepsilon_{\mathrm{M}}, \varepsilon_{\mathrm{C}}) = \frac{1-k+d}{1-d}\varepsilon_{\mathrm{M}} + \frac{k}{1-d}\,\varepsilon_{\mathrm{C}} = \left(1 - \frac{k}{1-d}\right)\varepsilon_{\mathrm{M}} + \frac{k}{1-d}\,\varepsilon_{\mathrm{C}} \quad \text{(A12)}$$

Introduction of (A1), (A2) and (A8) in (A12) yields

$$\frac{1}{E_{\mathrm{EV}}} = \frac{k}{(1+d)} \frac{1}{E_{\mathrm{M}}\left(1 + \frac{(k)^2}{(1+d)^2}\frac{\boldsymbol{k_{adh}^2}\,E_{\mathrm{F}} - E_{\mathrm{M}}}{E_{\mathrm{M}}}\right)} + \left(1 - \frac{k}{(1+d)}\right)\frac{1}{E_{\mathrm{M}}} \quad \text{(A13)}$$

and solving for E_{EV} yields

$$\frac{1}{E_{\mathrm{EV}}} = \frac{\frac{k}{(1+d)}}{E_{\mathrm{M}}\left(1 + \frac{(k)^2}{(1+d)^2}\frac{\boldsymbol{k_{adh}^2}\,E_{\mathrm{F}} - E_{\mathrm{M}}}{E_{\mathrm{M}}}\right)} + \frac{\left(1 - \frac{k}{(1+d)}\right)}{E_M}$$

$$\frac{1}{E_{\mathrm{EV}}} = \frac{\frac{k}{(1+d)}}{E_{\mathrm{M}}\left(1 + \frac{(k)^2}{(1+d)^2}\frac{\boldsymbol{k_{adh}^2}\,E_{\mathrm{F}} - E_{\mathrm{M}}}{E_{\mathrm{M}}}\right)} + \frac{\left(1 - \frac{k}{(1+d)}\right)}{E_{\mathrm{M}}} \frac{\left(1 + \frac{(k)^2}{(1+d)^2}\frac{\boldsymbol{k_{adh}^2}\,E_{\mathrm{F}} - E_{\mathrm{M}}}{E_{\mathrm{M}}}\right)}{\left(1 + \frac{(k)^2}{(1+d)^2}\frac{\boldsymbol{k_{adh}^2}\,E_{\mathrm{F}} - E_{\mathrm{M}}}{E_{\mathrm{M}}}\right)}$$

$$\frac{1}{E_{\mathrm{EV}}} = \frac{\frac{k}{(1+d)} + \left(1 - \frac{k}{(1+d)}\right)\left(1 + \frac{(k)^2}{(1+d)^2}\frac{\boldsymbol{k_{adh}^2}\,E_{\mathrm{F}} - E_{\mathrm{M}}}{E_{\mathrm{M}}}\right)}{E_{\mathrm{M}}\left(1 + \frac{(k)^2}{(1+d)^2}\frac{\boldsymbol{k_{adh}^2}\,E_{\mathrm{F}} - E_{\mathrm{M}}}{E_{\mathrm{M}}}\right)}$$

$$\frac{1}{E_{\mathrm{EV}}} = \frac{1 + \frac{(k)^2}{(1+d)^2}\frac{\boldsymbol{k_{adh}^2}\,E_{\mathrm{F}} - E_{\mathrm{M}}}{E_{\mathrm{M}}} - \frac{(k)^3}{(1+d)^3}\frac{\boldsymbol{k_{adh}^2}\,E_{\mathrm{F}} - E_{\mathrm{M}}}{E_{\mathrm{M}}}}{E_{\mathrm{M}}\left(1 + \frac{(k)^2}{(1+d)^2}\frac{\boldsymbol{k_{adh}^2}\,E_{\mathrm{F}} - E_{\mathrm{M}}}{E_{\mathrm{M}}}\right)} \quad \text{(A14)}$$

Inversion yields the modulus of EV in *in series* arrangement (and the upper bound of composites with spherical disperse phase)

$$\boxed{E_{\mathrm{EV}} = E_{\mathrm{M}}\left(1 + \frac{\frac{(k)^3}{(1+d)^3}\frac{\boldsymbol{k_{adh}^2}\,E_{\mathrm{F}} - E_{\mathrm{M}}}{E_{\mathrm{M}}}}{1 + \frac{(k)^2}{(1+d)^2}\frac{\boldsymbol{k_{adh}^2}\,E_{\mathrm{F}} - E_{\mathrm{M}}}{E_{\mathrm{M}}} - \frac{(k)^3}{(1+d)^3}\frac{\boldsymbol{k_{adh}^2}\,E_{\mathrm{F}} - E_{\mathrm{M}}}{E_{\mathrm{M}}}}\right)} \quad \text{(A15)}$$

The efficiency factor *k* is related to the filler volume content v_{F}.

$$v_{\mathrm{F}} = \frac{(k\,)^3}{(1+d)^3}; \qquad {v_{\mathrm{F}}}^{2/3} = \frac{(k)^2}{(1+d)^2}; \qquad v_{\mathrm{F}}^{1/3} = \frac{k}{(1+d)} \quad \text{(A16)}$$

and (11) turns to $$E_{\mathrm{EV}} = E_{\mathrm{M}}\left(1 + \frac{v_{\mathrm{F}}\,\frac{\boldsymbol{k}_{\mathbf{adh}}^{2}\,E_{\mathrm{F}}-E_{\mathrm{M}}}{E_{\mathrm{M}}}}{1 + {v_{\mathrm{F}}}^{2/3}\,\frac{\boldsymbol{k}_{\mathbf{adh}}^{2}\,E_{\mathrm{F}}-E_{\mathrm{M}}}{E_{\mathrm{M}}} - v_{\mathrm{F}}\,\frac{\boldsymbol{k}_{\mathbf{adh}}^{2}\,E_{\mathrm{F}}-E_{\mathrm{M}}}{E_{\mathrm{M}}}}\right) \quad \text{(A17)}$$

For perfect interfacial adhesion with k_{adh}=1, equation (A13) is identical to Paul's relation determined by a *cube in cube* treatment.

Case 2: *parallel* arrangement

Stress strain relation of the EV (represents the macroscopic quantities)

$$\sigma = \sigma_{\mathrm{EV}} = E_{\mathrm{EV}}\,\frac{\Delta(D+a)}{D+a} = E_{\mathrm{EV}}\,\varepsilon_{\mathrm{EV}} \quad \Rightarrow \qquad \varepsilon_{\mathrm{EV}} = \frac{\sigma}{E_{\mathrm{EV}}} \qquad \text{(A18)}$$

The macroscopic stress σ acts both on matrix part with σ_{M} and composite part with σ_{C}

$$\sigma = \sigma_{\mathrm{M}}\,\frac{A_{\mathrm{M}}}{A_0} + \sigma_{\mathrm{C}}\,\frac{A_{\mathrm{C}}}{A_0} = \sigma_{\mathrm{M}}\left(1 - \frac{k^2}{(1+d)^2}\right) + \sigma_{\mathrm{C}}\,\frac{k^2}{(1+d)^2} \qquad \text{(A19)}$$

The strain of the matrix part ε_{M} is identical to the strain of the EV $\varepsilon_{\mathrm{EV}}$. Thus, the stress strain relation of the matrix part is given by

$$\sigma_{\mathrm{M}} = E_{\mathrm{M}}\,\varepsilon_{\mathrm{EV}} \qquad \varepsilon_{\mathrm{EV}} = \frac{\sigma_{\mathrm{M}}}{E_{\mathrm{M}}} \qquad \text{(A20)}$$

Stress strain relations of the composites part where the three stresses are identical are given by

$$\sigma_{\mathrm{C}} = E_{\mathrm{C}}\,\varepsilon_{\mathrm{EV}} \quad \Leftrightarrow \quad \sigma_{\mathrm{C,M}} = E_{\mathrm{M}}\,\varepsilon_{\mathrm{M}} \quad \Leftrightarrow \quad \sigma_{\mathrm{C,F}} = \boldsymbol{k}_{\mathbf{adh}}^{\mathbf{2}}\,E_{\mathrm{F}}\,\varepsilon_{\mathrm{F}} \qquad \text{(A21)}$$

with the corresponding strains

$$\varepsilon_{\mathrm{EV}} = \frac{\sigma_{\mathrm{C}}}{E_{\mathrm{C}}} \quad (19) \qquad \varepsilon_{\mathrm{M}} = \frac{\sigma_{\mathrm{C,M}}}{E_{\mathrm{M}}} \quad \text{(A22)} \qquad \varepsilon_{\mathrm{F}} = \frac{\sigma_{\mathrm{C,F}}}{\boldsymbol{k}_{\mathbf{adh}}^{\mathbf{2}}\,E_{\mathrm{F}}} \qquad \text{(A23)}$$

They are connected to each other by

$$\varepsilon_{EV} = \frac{k}{(1+d)}\,\varepsilon_F + \left(1 - \frac{k}{(1+d)}\right)\,\varepsilon_M \qquad \text{(A24)}$$

Insertion of (A19), (A20) and (A21) in (A22) yields

$$\frac{1}{E_C} = \frac{k}{(1+d)}\,\frac{1}{\boldsymbol{k}_{\boldsymbol{adh}}^{\mathbf{2}}\,E_F} + \left(1 - \frac{k}{(1+d)}\right)\,\frac{1}{E_M} \qquad \text{(A25)}$$

Solving for the modulus of the composites part E_C yields

$$E_C = \frac{E_M\;\boldsymbol{k}_{\boldsymbol{adh}}^{\mathbf{2}}\,E_F}{\left(1-\frac{k}{1+d}\right)\boldsymbol{k}_{\boldsymbol{adh}}^{\mathbf{2}}\,E_F + \frac{k}{1+d}\,E_M} \qquad \text{(A26)}$$

Introduction of (A15), (A17) and (A18) with (A24) in (A16) yields

$$E_{\mathrm{EV}}\,\varepsilon_{\mathrm{EV}} = E_{\mathrm{M}}\left(1-\frac{k^2}{(1+d)^2}\right)\varepsilon_{\mathrm{EV}} + \frac{E_{\mathrm{M}}\,\boldsymbol{k}_{\mathbf{adh}}^{\mathbf{2}}\,E_{\mathrm{F}}}{\left(1-\frac{k}{1+d}\right)\boldsymbol{k}_{\mathbf{adh}}^{\mathbf{2}}\,E_{\mathrm{F}}+\frac{k}{1+d}E_{\mathrm{M}}}\,\frac{k^2}{(1+d)^2}\,\varepsilon_{\mathrm{EV}} \tag{A27a}$$

$$E_{\mathrm{EV}} = E_{\mathrm{M}}\left\{\left(1-\frac{k^2}{(1+d)^2}\right) + \frac{\boldsymbol{k}_{\mathbf{adh}}^{\mathbf{2}}\,E_{\mathrm{F}}}{\left(1-\frac{k}{1+d}\right)\boldsymbol{k}_{\mathbf{adh}}^{\mathbf{2}}\,E_{\mathrm{F}}+\frac{k}{1+d}E_{\mathrm{M}}}\,\frac{k^2}{(1+d)^2}\right\} \tag{A27b}$$

Rearranging yields

$$E_{\mathrm{EV}} = E_{\mathrm{M}}\left\{1-\frac{k^2}{(1+d)^2} + \frac{k^2}{(1+d)^2}\,\frac{\boldsymbol{k}_{\mathbf{adh}}^{\mathbf{2}}\,E_{\mathrm{F}}}{\left(1-\frac{k}{1+d}\right)\boldsymbol{k}_{\mathbf{adh}}^{\mathbf{2}}\,E_{\mathrm{F}}+\frac{k}{1+d}E_{\mathrm{M}}}\right\}$$

$$E_{\mathrm{EV}} = E_{M}\left\{1-\frac{k^2}{(1+d)^2} + \frac{k^2}{(1+d)^2}\,\frac{\boldsymbol{k}_{\mathbf{adh}}^{\mathbf{2}}\,E_{\mathrm{F}}}{\boldsymbol{k}_{\boldsymbol{adh}}^{\mathbf{2}}\,E_{\mathrm{F}}-\frac{k}{1+d}\left(\boldsymbol{k}_{\mathbf{adh}}^{\mathbf{2}}\,E_{\mathrm{F}}-E_{\mathrm{M}}\right)}\right\}$$

$$E_{\mathrm{EV}} = E_{\mathrm{M}}\left\{1+\frac{k^2}{(1+d)^2}\left(\frac{\boldsymbol{k}_{\mathbf{adh}}^{\mathbf{2}}\,E_{\mathrm{F}}}{\boldsymbol{k}_{\mathbf{adh}}^{\mathbf{2}}\,E_{\mathrm{F}}-\frac{k}{1+d}\left(\boldsymbol{k}_{\mathbf{adh}}^{\mathbf{2}}\,E_{\mathrm{F}}-E_{\mathrm{M}}\right)}-\;1\right)\right\}$$

$$E_{\mathrm{EV}} = E_{\mathrm{M}}\left\{1+\frac{k^2}{(1+d)^2}\left(\frac{\boldsymbol{k}_{\mathbf{adh}}^{\mathbf{2}}\,E_{F}-\boldsymbol{k}_{\mathbf{adh}}^{\mathbf{2}}\,E_{\mathrm{F}}+\frac{k}{1+d}\left(\boldsymbol{k}_{\mathbf{adh}}^{\mathbf{2}}\,E_{\mathrm{F}}-E_{\mathrm{M}}\right)}{\boldsymbol{k}_{\mathbf{adh}}^{\mathbf{2}}\,E_{\mathrm{F}}-\frac{k}{1+d}\left(\boldsymbol{k}_{\mathbf{adh}}^{\mathbf{2}}\,E_{\mathrm{F}}-E_{\mathrm{M}}\right)}\right)\right\}$$

$$E_{\mathrm{EV}} = E_{\mathrm{M}}\left(1+\frac{\frac{k^3}{(1+d)^3}\left(\boldsymbol{k}_{\mathbf{adh}}^{\mathbf{2}}\,E_{\mathrm{F}}-E_{M}\right)}{\boldsymbol{k}_{\mathbf{adh}}^{\mathbf{2}}\,E_{\mathrm{F}}-\frac{k}{1+d}\left(\boldsymbol{k}_{\mathbf{adh}}^{\mathbf{2}}\,E_{\mathrm{F}}-E_{\mathrm{M}}\right)}\right) \tag{A28}$$

Thus, the modulus of EV in *parallel* arrangement (and the lower bound of composites with spherical disperse phase) is given by

$$\boxed{E_{\mathrm{EV}} = E_{\mathrm{M}}\left(1+\frac{\frac{k^3}{(1+d)^3}\,\frac{\boldsymbol{k}_{\mathbf{adh}}^{\mathbf{2}}\,E_{\mathrm{F}}-E_{\mathrm{M}}}{E_{\mathrm{M}}}}{\frac{\boldsymbol{k}_{\mathbf{adh}}^{\mathbf{2}}\,E_{\mathrm{F}}}{E_{\mathrm{M}}}-\frac{k}{1+d}\,\frac{\boldsymbol{k}_{\mathbf{adh}}^{\mathbf{2}}\,E_{\mathrm{F}}-E_{\mathrm{M}}}{E_{\mathrm{M}}}}\right)} \tag{A29}$$

Introduction of v_{F} using (12) provides

$$E_{\mathrm{EV}} = E_{\mathrm{M}}\left(1+\frac{v_F\,\frac{\boldsymbol{k}_{\mathbf{adh}}^{\mathbf{2}}\,E_{\mathrm{F}}-E_{\mathrm{M}}}{E_{\mathrm{M}}}}{\frac{\boldsymbol{k}_{\mathbf{adh}}^{\mathbf{2}}\,E_{\mathrm{F}}}{E_{\mathrm{M}}}-v_{\mathrm{F}}^{1/3}\,\frac{\boldsymbol{k}_{\mathbf{adh}}^{\mathbf{2}}\,E_{\mathrm{F}}-E_{\mathrm{M}}}{E_{\mathrm{M}}}}\right) \tag{A30}$$

Appendix B

Creep compliances of SFRC considering the fiber orientation

The orientation factors f_3 in thickness direction are close to zero for PMC which indicates that the plates are close to lamina, and the fiber orientation can be taken into account for the plane stress state. The stress strain relation of the transversely isotropic EV is given in the main axes system by

$$\begin{pmatrix}\varepsilon_1\\ \varepsilon_2\\ \varepsilon_3\end{pmatrix} = \begin{pmatrix}\varepsilon_1\\ \varepsilon_2\\ \gamma_{12}\end{pmatrix} = \begin{pmatrix}J_{11} & J_{12} & 0\\ J_{12} & J_{22} & 0\\ 0 & 0 & J_{66}\end{pmatrix}\begin{pmatrix}\sigma_1\\ \sigma_2\\ \tau_{12}\end{pmatrix} \tag{B1}$$

$$\text{with } J_{11} = \frac{1}{E_{11}}\,, J_{12} = -\frac{\mu_{12}}{E_{11}} = -\frac{\mu_{21}}{E_{22}}, J_{22} = \frac{1}{E_{22}}\,, \text{ and } J_{66} = \frac{1}{G_{12}} \tag{B2}$$

Usually the coordinate system of a part differs from the main axes system of the EV requiring a transformation leading to

$$\begin{pmatrix}\varepsilon_x\\ \varepsilon_y\\ \varepsilon_z\end{pmatrix} = \begin{pmatrix}\varepsilon_x\\ \varepsilon_y\\ \gamma_{xy}\end{pmatrix} = \begin{pmatrix}\bar{J}_{11} & \bar{J}_{12} & \bar{J}_{16}\\ \bar{J}_{12} & \bar{J}_{22} & \bar{J}_{26}\\ \bar{J}_{16} & \bar{J}_{26} & \bar{J}_{66}\end{pmatrix}\begin{pmatrix}\sigma_x\\ \sigma_y\\ \tau_{xy}\end{pmatrix}. \tag{B3}$$

Now the components of the $\bar{J}$-matrix depend on the components of the J -matrix and the angle θ of misalignment of fiber orientation to the direction of the external load:

$$\bar{J}_{11} = J_{11}\,cos^4\,\theta + (2J_{12} + J_{66})\,sin^2\,\theta\,cos^2\,\theta + J_{22}\,sin^4\,\theta \tag{B4a}$$

$$\bar{J}_{12} = J_{12}(sin^4\,\theta + cos^4\,\theta) + (J_{11} + J_{22} - J_{66})\,sin^2\,\theta\,cos^2\,\theta \tag{B4b}$$

$$\bar{J}_{22} = J_{11}\,sin^4\,\theta + (2J_{12} + J_{66})\,sin^2\,\theta\,cos^2\,\theta + J_{22}\,cos^4\,\theta \tag{B4c}$$

$$\bar{J}_{16} = (2J_{11} - 2J_{12} - J_{66})\,sin\,\theta\,cos^3\,\theta - (2J_{22} - 2J_{12} - J_{66})\,sin^3\,\theta\,cos\,\theta \tag{B4d}$$

$$\bar{J}_{26} = (2J_{11} - 2J_{12} - J_{66})\,sin^3\,\theta\,cos\,\theta - (2J_{22} - 2J_{12} - J_{66})\,sin\,\theta\,cos^3\,\theta \tag{B4e}$$

$$\bar{J}_{66} = 2(2J_{11} + 2J_{22} - 4J_{12} - J_{66})\,sin^2\,\theta\,cos^2\,\theta + J_{66}(sin^4\,\theta + cos^4\,\theta) \tag{B4f}$$

The J_{ij} are defined in terms of the engineering constants in Eq. (B2). To measure the creep parallel to the flow direction, the stress σ_0= (σ_0, 0, 0) has to be applied in x-direction leading to

$$\bar{J}_{11}(t,\sigma_0) = \frac{1}{E_{11}}\cos^4\theta + \left(-\frac{2\mu_{12}}{E_{11}} + \frac{1}{G_{12}}\right)\sin^2\theta\cos^2\theta + \frac{1}{E_{22}}\sin^4\theta = J_{11}(t,\sigma_o)\cos^4\theta + \left(-2\,\mu_{12}\,J_{11}(t,\sigma_o) + \frac{1}{G_{12}(t,\sigma_0)}\right)\sin^2\theta\cos^2\theta + J_{22}(t,\sigma_o)\sin^4\theta \tag{B5}$$

and to measure the creep perpendicular to the flow direction, the stress $\sigma_0 = (\sigma_0, 0, 0)$ has to be applied in y-direction leading to

$$\bar{J}_{22}(t,\sigma_0) = \frac{1}{E_{11}}\sin^4\theta + \left(-\frac{2\mu_{12}}{E_{11}} + \frac{1}{G_{12}}\right)\sin^2\theta\cos^2\theta + \frac{1}{E_{22}}\cos^4\theta = J_{11}(t,\sigma_o)\sin^4\theta + \left(-2\,\mu_{12}\,J_{11}(t,\sigma_o) + \frac{1}{G_{12}(t,\sigma_0)}\right)\sin^2\theta\cos^2\theta + J_{22}(t,\sigma_o)\cos^4\theta \quad \text{(B6)}$$

The equations (B5) and (B6) contain the shear modulus G_{12} that wasn't measured experimentally and therefore has to be approximated. If one assumes that the PBT matrix and the glass fibers are isotropic materials, the corresponding shear moduli can be expressed by their Young's moduli and Poisson's ratios.

$$G_{\mathrm{M}} = \frac{E_{\mathrm{M}}}{2\,(1+\mu_{\mathrm{M}})} \qquad \text{or} \qquad G_{\mathrm{F}} = \frac{E_{\mathrm{F}}}{2\,(1+\mu_{\mathrm{F}})} \quad \text{(B7)}$$

The EVC can be derived for shear properties leading to

$$G_{12} = G_{\mathrm{M}}(1+d)\left[\frac{1+kr\left((1+d)(r+d)\right)^{-1}\beta_{\mathrm{G}}}{k+(1+d-k)\left(1+kr\left((1+d)(r+d)\right)^{-1}\beta_{\mathrm{G}}\right)}\right] \quad \text{with} \quad \beta_{\mathrm{G}} = \frac{G_{\mathrm{F}}-G_{\mathrm{M}}}{G_{\mathrm{M}}} \quad \text{(B8)}$$

and introducing equation (B7) to (B8) and rearranging leads to

$$\frac{1}{G_{12}(t,\sigma_0)} = J_{22}(t,\sigma_0)\;\underbrace{2(1+\mu_{\mathrm{M}})\left[\frac{1+\frac{(1+d-k)\frac{(\mu_{\mathrm{M}}-\mu_{\mathrm{F}})}{(1+\mu_{\mathrm{F}})}E_{\mathrm{R}}+(1+d-k)\frac{(\mu_{\mathrm{M}}-\mu_{\mathrm{F}})}{(1+\mu_{\mathrm{F}})}A_{\mathrm{F}}^{\perp}E_{\mathrm{R}}}{k+(1+d-k)(E_R-1)+(1+d-k)\,A_{\mathrm{F}}^{\perp}\,(E_{\mathrm{R}}-1)}}{1+\frac{\frac{(\mu_{\mathrm{M}}-\mu_{\mathrm{F}})}{(1+\mu_{\mathrm{F}})}A_{\mathrm{F}}^{\perp}E_{\mathrm{R}}}{1+A_{\mathrm{F}}^{\perp}\,(E_{\mathrm{R}}-1)}}\right]}_{\text{shear correction factor } g_{\mathrm{J}}} \quad \text{(B9)}$$

The shear correction factor g_{J} depends on both the materials properties relative modulus E_{R} and Poisson's ratios μ of fiber and matrix and the geometry of the EV given by aspect ratio r and normalized fiber distance d. Their effects on the relative modulus E_{R} are shown in Fig. B1 for a Poisson's ratio $\mu_{\mathrm{F}} = 0.25$. If the relative moduli exceed 10 – injection molded short glass fiber reinforced composites have relative moduli of typically 15 to 40 – the shear correction factor g_{J} decreases from 2.95 to 2.85 for both PBT GF20 and PBT GF30. If the Poisson's ratio increases from 0 to 0.5, the shear correction factor g_{J} decreases from 2.93 to 2.82, Fig. B2.

For relative moduli exceeding 30, the shear correction factor g_{J} approaches asymptotically the value 2.8. Due to relaxation processes, the matrix moduli decrease during creep experiment but this does not significantly affect the shear corrections factor g_{J}. The relevant consequence is that the time and stress dependency of $J_{66} = \frac{1}{G_{12}}$ corresponds directly to the time and stress dependency of J_{22}:

$$J_{66} = J_{22}\,g_{\mathrm{J}} \quad \text{(B10)}$$

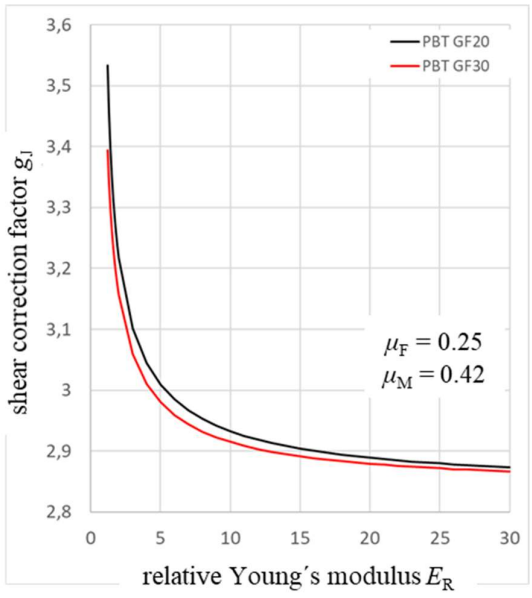

Fig. B1 Dependence of relative modulus E_R of fiber and matrix on shear correction factor g_J

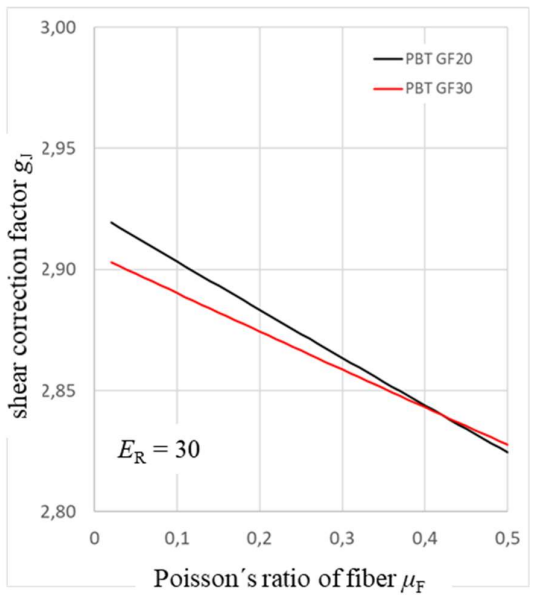

Fig. B2 Dependence of Poisson's ratio of fibers on shear correction factor g_J

Julian Niklas Rech

Reinforcing mechanisms of polymer matrix composites: evaluation and modeling of matrix/dispersed phase interrelationship

Zpevňující mechanismy kompozitů s polymerní matricí: hodnocení a modelování vztahů mezi matricí a disperzní fází

Doctoral Thesis